Numerical Investigation of the Flow Between Two Stationary Parallel Discs.

Jomir Uddin Soroardy

A Thesis

In

The Department

Of

Mechanical and Industrial Engineering

Presented in Partial Fulfillment of Requirements for the degree of

Master of Applied Science at

Concordia University

Montreal, Quebec, Canada.

November 2006

Your file Votre référence
ISBN: 978-0-494-28945-7
Our file Notre référence
ISBN: 978-0-494-28945-7

ABSTRACT

Numerical Investigation of the Flow Between Two Stationary Parallel Discs.

Jomir Uddin Soroardy

Steady, incompressible turbulent sink flows that develop between two stationery discs with and without swirl were investigated numerically using the software FLUENT 6.1 with the Reynolds Stress Model (RSM) employed to approximate turbulence. The main purpose of the work is to validate the method and then elaborate on some key features of these types of flows.

Both problems studied here were characterized by severe streamline bending. Exploratory tests using the k-ε methodology reconfirmed that it is not suitable for flows of these type. Instead, the Reynolds Stress Model (RSM) with five equations for 2D geometry and 7 equations for 3D to accurately resolved the physics of the problems well. Furthermore, the continuative rather the pressure boundary condition yielded stable solutions. Care however had to be applied in selecting the length of the outlet manifold. The basic idea was to avoid the *vena contracta* after the ninety-degree bend by increasing the length of the exit pipe.

The obtained numerical results are shown to be in accord with past experiments throughout the entire domain. The technique is able to resolve, at a satisfactory level, the flow development even at known problematic areas such as for

example near the sink exit. Acceleration was found to be the primary controlling factor for both purely radial and swirling inflow where monotonic changes of pressure gradient are a common manifestation.

For uni-radial sink flow, inertia increase either due to inlet velocity augmentation or decrease of the local area produces flatter velocity profiles thus suggesting that inertia reigns over the viscous forces. In the case of swirling inflow, the overpowering centrifugal force field forced almost all of the fluid to be drained through the Ekman's boundary layers developed on each of the disk surface. It now becomes clear that the growth of flow near the disk or spikes in the radial velocity is due to the combined action of boundary layer development and local reduction of the flow area. The numerical algorithm was also able, for the first time, to successfully capture the toroidal recirculation zone that is known to inhabit the central portion of the flow. The latter is also responsible for the development of a reversed flow, which causes the saddle-like behavior of the radial velocity near the mid-plane. The tangential velocity peaks near the disks known from previous experiments and numerical formulations appeared also in the current solutions.

Therefore, the present study has validated a tool that can now be used to provide answers to some outstanding questions. It can be employed to provide an insight into the stabilizing effects of acceleration which encourages the flow to remain laminar even at very high inlet Reynolds numbers, or to laminarize in case that the entering flow is turbulent. It could also provide the limits of validity of the previous simple models.

ACKNOWLEDGEMENTS

Greatest gratitude goes to my supervisor Professor Dr. G.H. Vatistas for his strong support throughout the course of this research work by transferring me his valuable idea, and for his discussions and suggestions.

Special appreciations are due to Mohammad Fayed for his discussion to obtain more clear understanding of the physics of this complex flow and for his encouragement to work in team. Sincere thanks also to Ait abderrahmane hamid for his valuable advice.

I would like to thank Dr. Ali Jawarneh for his initial help in learning the software used in this work.

I am expressing my indebtness to my parents who always stand behind me, my Uncle M.S. Khalid Bin Huda and brother Main Uddin Soroardy for their financial and moral support to achieve success.

This work is dedicated to my parents Mohammad Hossain soroardy and
Khaleda Akhtar.

Contents

Nomenclature

h	Half the gap size (mm or in).
H	Gap size (mm or in).
k	Turbulent Kinetic Energy (m2/s2).
p	Pressure (Pa).
r, θ, z	Polar Coordinates
R_0	Radius of discs (mm or in).
R_i	Radius of sink exit (mm or in).
Re	Reynolds Number with respect to gap size
Re_r	Reynolds number with respect to disc radius
S	Swirl ratio
t	Time (sec).
u	Dimensionless Radial velocity
u_0	Inlet radial velocity (m/s or ft/s).
$\vec{v}$	Velocity with direction
v	Dimensionless Swirl velocity
v_0	Inlet swirl velocity (m/s, ft/s).
v_r	Radial velocity (m/s, ft/s).
v_θ	Swirl or tangential Velocity (m/s, ft/s).
v_z	Axial Velocity (m/s or ft/s).

v_i	Mean velocity of turbulent flow in i direction (m/s).
v_j	Mean velocity of turbulent flow in j direction (m/s).
v_k	Mean velocity of turbulent flow in k direction (m/s).
v'_i	Fluctuating velocity of turbulent flow in i direction (m/s).
v'_j	Fluctuating velocity of turbulent flow in j direction (m/s).
v'_k	Fluctuating velocity of turbulent flow in k direction(m/s).
w	Dimensionless Axial velocity
x_i, x_j, x_k	Distances in Cartesian coordinates i,j,k
ρ	Density of fluid (air) (Kg/m3)
μ	Dynamic Viscosity of fluid (air)(N-S/m2).
ν	Kinematic Viscosity of fluid (air) (m2/s).
∇	Gradient
σ	Aspect Ratio
η	Dimensionless radial coordinate
ζ	Dimensionless axial coordinate
Π	Dimensionless pressure
fn	Function
ε	Turbulent Dissipation rate (m2/s3).
μ_t	Turbulence Viscosity (N-S/m2).

List of Figures

List of Tables

CHAPTER 1

Introduction

The long interest of researchers in disc-type flow domains is due to the industrial relevance of the problem. This situation often appears in several turbo-machinery components, in the radial diffuser, the vortex gyroscope, heat exchangers etc. The problem can be examined using the setup shown schematically in figure 1.1

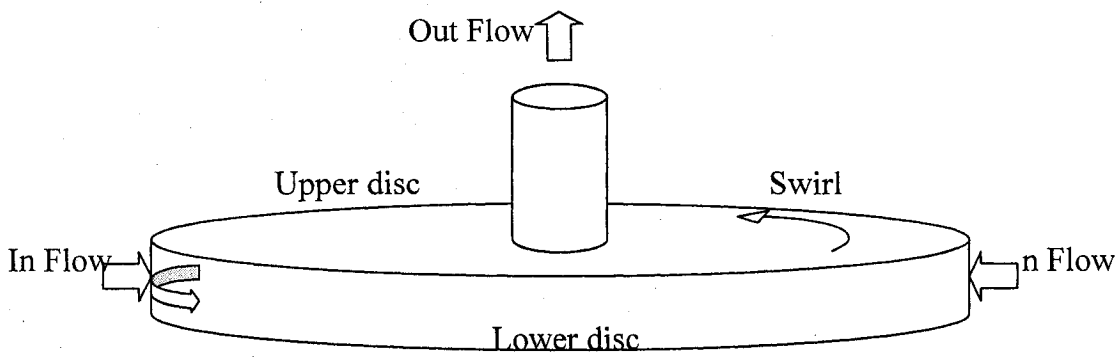

Figure 1.1: Disc type domain for purely radial or swirling flow.

Fundamentally, several types of flows could be generated within this configuration; the sink flow and the source flow with or without swirl. In the case of a sink flow (or inward flow) the setup allows the fluid to enter through the periphery and drained out by a centrally located exit on one disc or on both of them. On the other hand, source flow or outward flow can be created by turning around the direction of the last type of flow keeping in mind that reversing the direction of flow may not always reverse the flow characteristics. Both inflow and outflow exhibit the releminarization phenomenon [Sovran, 1967], which plays an important role in fluid

dynamics. Here focus will be given on the purely radial inflow with and without swirl.

Past experimental, theoretical as well as numerical efforts approached the problem form different angles with the aim to examine some specific flow characteristics.

1.1 Purely sink flow:

This type of flow deals with the converging kind where no tangential velocity is being introduced. Purely radial inflow includes the important properties of a monotonic decreasing pressure as a consequence of a continuously increasing acceleration in the direction of the flow. Due to the stabilizing effect of acceleration, the flow behaves as a laminar one even though it is was turbulent when entered the domain [Murphy, et al., 1983]. Industrial applications of this type include the double disc valves, air bearings, pneumatic micrometers, flow rate and viscosity meters.

1.2 Swirling inflow

Imparting to the entering fluid, a tangential velocity component, in addition to the radial, creates swirling disk inflow. The superimposed swirl generates a strong centrifugal force field inside the domain which alters completely the character of the flow. Typical industrial applications of flow fields of this kind are the gaseous core nuclear rocket engine [Savino & Keshok, 1965] and the vortex combustors [Jawarneh, et al., 2004]. More over, the notable use of the swirling type flow found in

cyclone separators and incinerators, the vortex gyroscope, the vortex pump, the swirl atomizer, multiple disc turbo machinery cascades, make it attractive to fluid dynamicists. The complexities related to mainly the dominance of the centrifugal force and the complexity of the boundary conditions introduces severe obstacles that have prevented a general analytical solution in the past. Furthermore, excessive time (and thus prohibitive cost) requirement have also hindered even a proper experimental characterization of the problem. It is for these reasons that we have decided to numerically solve for the turbulent flow in such domain using the commercially available CFD software FLUENT 6.1. Many industries are now routinely involving the less expensive CFD methods to simulate complicated fluid flows. Besides, because of the massive development in computer memory, this technique provides fast, economical, and highly accurate [Ferziger & Peric, 1999] results. Nevertheless, the numerical solution is always approximate in comparison the exact analytical. Errors in the description are concerned with the imposition of assumptions, the selection of the appropriate boundary conditions, solver setup to approximate the differential equations, discritization and iterations strategies. Steady, axi-symmetric, incompressible assumptions are taken to reduce the complexity of flow simulation. The Reynolds Stress Model (RSM) is selected to simulate turbulence.

CHAPTER 2

Technical Literature Review

In the last decades, several analytical, numerical, and experimental investigations have improved our understanding of the phenomenon. Priority will be given here to only previous contributions that are directly relevant to the present work.

Savino and Keshok [1965] conducted a series of experiments in a 0.107 aspect ratio (height to diameter ratio) cylindrical chamber with the aim to map the radial, tangential velocity, and pressure distributions. The causes that had as an effect the development of their respective profiles were examined. Air was injected tangentially through the periphery and exhausted by a centrally located outlet. A probe was used to sense both of the magnitude and the direction of velocity at different radial locations. The non-dimensional radial velocity profiles were found to exhibit a distinct similarity near the upper and lower boundaries (upper and lower plates). It was discovered that under the influence of a strong centrifugal field the fluid finds the exit moving close to the upper and lower dicks where due to the presence of Ekman's boundary layers where the centrifugal force is at its minimum. Consequently, the fluid is seen to find the exit through the upper and lower boundary layers thus choosing the path of the least action. The measurements also show the radial velocity to be small

way from the walls (in the mid-channel region). Away from the exit port and near the mid- channel the tangential velocity was found to follow closely a free-vortex profile. The latter finding made the analytical determination of the pressure possible. The determined factor responsible for such behavior is therefore the swirl ($S = \frac{v_\theta}{v_r} = 15$ in their case), imparted to the fluid at the inlet. This high inlet swirl strength is the cause of such a distinct flow manifestation.

Wormley [1969] developed a momentum integral analysis for a steady, incompressible swirling inflow in a short vortex valve considering the interaction between the invicid vortex core and viscous end wall boundary layers. The inlet and exit regions of the chamber were excluded. In search of simplifying assumptions for the analytical solution, a series of water flow visualizations were also performed employing air bubbles and milk powder to visualize the flow. In the experiment, the steady stream of bubbles entered the chamber and immediately rose to the upper wall, and then traveled to the exit following closely the upper disk surface. At very high swirling ratio the milky "donut" lingered for a long time near the mid-plane of the chamber indicating the existence of a lesser radial flow region, with the bulk of the fluid moving mainly through the end-wall boundary layers. As the swirl strength was reduced, the radial flow penetrated further into the mid-channel plane. At very weak swirl, there was no milk observed inside the valve confirming that a radial flow was developing along the entire axial span of the chamber. In his analytical derivations, he considered two regions; the developing flow zone and developed one. Every region

was further subdivided into two sub-zones; the boundary layer and core flow. In mid-channel both the radial and tangential velocities were assumed to be sole function of the radius, while near the end walls they were function of the axial distance as well. The obtained analytical expression for the pressure distribution agreed well with experimental findings. A parameter named Boundary Layer Coefficient (BLC), a function of the valve diameter, peripheral flow, total flow, and the wall frictional factor, was derived for short vortex valves.

Based on Wormley's technique [1969], Kowk et al [1972] numerically solved a set of differential equations for the flow within the annular region of a short vortex chamber. Attention was also given to extend his method and to examine the variation of the apparent viscosity throughout the flow field. Assuming the apparent viscosity (that consisted by the eddy viscosity + operating viscosity) to be a function of the tangential velocity in the core, the governing equations were simplified and integrated. Their calculations showed the non-dimensional boundary layer thickness of the entering fluid to first increase, reaching a maximum, and then reduce as the flow approached the sink. The tangential velocity profile agreed well with experiment within the main chamber. Near the exit where the streamlines bend to find the exit, the agreement was unsatisfactory. Furthermore, the simulations results showed that the radial velocity is not resolved adequately in both the boundary layers and inside the core flow regions. An empirical equation for apparent viscosity was also derived.

In a subsequent analytical study, Kwok and Lee [1978] applied the integral equation method for compressible inflow (without vortex) between two discs and considered the incompressible flow as a special case. Considering the flow process as an isothermal one, the derived nonlinear equation was solved numerically via a fourth order Runge-Kutta.

In the same decade, experimental work for purely radial and weak vortex in an angular rate sensor (aspect ratio $\leq$ 0.0170455) was reported by De santis and Rakwasky [1971]. The velocity data were obtained via hot-wire anemometry. In both swirling and non swirling flow, the experimental velocity profiles at smaller radii were not symmetric, which is contrary to what was expected when two outlets are used. In their study priority was given to the determination of the flow characteristics inside the boundary layer i.e. in the viscous dominated flow sector of the field. For the non- swirling sink, their experimental results established that the flow is mainly invicid inside the main chamber (for the range of inlet Reynolds no 300 to 1600) and the boundary layers developed near the discs constitutes only 10% of the flow field. The influence of boundary layers was examined by comparing the experimental values against the theory based on a modified version of the integral momentum boundary approach. As the flow accelerated toward the sink center, and under the influence of a favorable pressure gradient, the radial velocity followed the 1/r law. The boundary layers thinned out producing steeper velocity profiles along the flow direction. The theoretical displacement thickness corresponded reasonably to the experiment, while a small discrepancy was evident for the momentum thickness. The

measured inviscid centerline radial velocity values were in good agreement with the theory. The shear stress increased sharply with decreasing radius. A case of a very low aspect ratio (0.002727) chamber was tested and the flow was found to be fully-developed after a short distance down-stream from inlet, where the boundary layers merged. The entrance length was estimated analytically. In the case of swirling sink, experiments were conducted in a 0.01591 aspect ratio chamber with spin introduced to the fluid by rotating both discs. The swirl ratios were on the weak side of the swirl ratio spectrum (S = 0.03 and 0.06). Due to the probe rotation, the measured tangential velocities ware in doubt. In order to remedy the difficulty they added the quantity ωr to the measured values but found the experimental centerline tangential velocity to be larger than the inviscid velocity. Due to the presence of a porous coupler, the obtained boundary layer thickness was non zero at periphery. For purely radial inflow, displacement thickness was maximum at one-third the radial distance from the inlet and the maximum momentum thickness occurring at the 70% location of the non-dimensional radii. The radial wall shear stress increased sharply toward the center with the azimuthal component exhibiting very rapid growth. The experimental shear stress was always to lag behind the theoretical. For every Reynolds number in the interval [300, 1500], the efficiency, given in terms of the vortex strength, was seen to decrease linearly (from 1 to 0) with the radius.

Murphy et al [1978] studied both analytically and numerically the sink flow without swirl between two discs. Three flow regimes were considered; the entrance region where the flow is under the influence of strong viscous effects; the area near

the exit where strong inertial effects are present, and the region in the middle of the other two where both viscous and inertial effect are of equal importance. Assuming a uniform velocity profile at the inlet, they obtained a fully developed parabolic velocity profiles just after the inlet, with a boundary layer thickness half the gap size. As the flow advanced downstream, the acceleration dominated the flow causing flattening of the radial velocity distribution profiles. The flow resembled the familiar external boundary layer with a large central core flunked on both sides. The static pressure varied logarithmically at large and at very small radii as predicted by the potential Bernoulli equation, but not in the intermediate zone where both viscosity and acceleration are important. Murphy et al [1983] also studied the laterally converging laminar and turbulent flow between two parallel surfaces. Studies on the laminarizing or laminarascent phenomena were also included although their main interest remained on the near-wall region where the boundary layer assumptions for internal flow remained valid. For the laminar flow with local Reynolds number ranging from 210 to 21000, a test section having the circular shape was employed in the experiment and their results agreed well with the laminar approach. Smoke visualizations of the path lines from three directions provided evidence of no rapid mixing or diffusion that marked the dominance of acceleration rather than effect of turbulence in that flow region. In order to study turbulent and transitional flow, experiments conducted in a test section having the shape of a circular section. The local Reynolds number varied from 1600 up to 68000. Experimental results of the stream wise pressure were measured. In the range of high entering Reynolds number flow and minimal convergence, the fluid motion is quasi-developed, fully turbulent.

However, in the range of low flow rate and maximum lateral convergence, the experimental pressure drop differs modestly with the laminar and turbulent predictions.

An alternate momentum integral approach by Lee and Lin [1985] featured a second order differential equation that was solved numerically using Runge-Kutta method. Static pressure results for a purely radial inflow found to be in agreement with previous experimental evidence, though the velocity profiles did not.

Using a similar domain, Vatistas [1988] simplified the governing equations and was able to derive analytical closed form solution for the purely radial sink flow. Assuming the average changes of radial momentum and neglecting the axial velocity component (for small gap), the pressure drop was found to be consisting from the superposition of the viscous and the inertia inertial contributions. In the viscous affected region, radial velocity was the function of 1/r and z (axial distance) but in the case where inertia term dominated, radial velocity was dependent on 1/r only. The derived value for the maximum radial velocity was 3/2 times of local radial average velocity. The global friction coefficient was expressed in terms of a reduced Reynolds number. These analytical static pressure results were compared with previous experiments and were in very good agreement. Vatistas [1990] then focused on the linearization of the momentum equation of Lee and Lin and was able to derive a closed form solution. For low Reynolds numbers, the radial velocity distribution was almost the same as in earlier work with the Poisseuille parabolic profile emerging at

very low Reynolds numbers. Difference with the experiment was found to be within 12.5%. For high Reynolds number the velocity profiles became flat where the existence of boundary layers appeared as a consequence of the non-slip condition at the disk wall. Moreover, both creeping and invicid flow were shown to be the asymptotes to the general case.

In order to provide more accurate representations of the pressure and the radial velocity, Vatistas et al. [1995] solved the nonlinear equations numerically for purely radial inflow. Simplified derivations for velocity and pressure were functions of solely one dimensional parameter called λ which is the combination of Reynolds number and radial distance. For small λ values the obtained $\Delta\Pi$ was comparable to previous theories. Whereas, for large value of λ, the results varied substantially with the other theories except with the closed form solution given by Vatistas [1988]. The non-dimensional velocity profiles were also in fair agreement with the closed form solution at higher λ. However, for smaller λ the deviation was large.

Singh [1993] investigated the inward flow between two stationary parallel discs both experimentally and numerically. For low Reynolds numbers the k-ε model was employed to resolve the Reynolds stress. Increasing the local inlet Reynolds number and decreasing the gap diameter ratio, the pressure drop was found to increase. The accompanied experimental measurements *via* a Laser Doppler Anemometer showed that the velocity profiles are symmetric about mid plane near

the inlet. As expected, in the neighborhood of the exit, where the streamlines bend for the fluid to negotiate the exit, the velocity becomes asymmetric with its maximum value occurring near the disc containing outlet. The turbulent intensity was found maximum near the wall remaining more or less constant on the core region. Due to the stabilizing effects of acceleration on the production of turbulent kinetic energy, increasing the Reynolds number resulted into a decrease of the velocity fluctuations. It was amply evident from their results that the turbulent kinetic energy decayed faster at smaller gap ratios. The latter observation suggests that a decrease in gap size has a stabilizing effect on the flow.

A power series solution, where all material elements were either monotonically accelerating or decelerating, was presented by Zitouni and Vatistas [1997]. The series were evaluated numerically. As mentioned previously, all the controlling parameters were expressed in terms of λ (function of other dimensionless radius and reduced Reynolds number). For λ closed to zero, both sink and source flow showed the familiar Poiseuille profiles. However, for large λ values, the two flows were entirely different to mid-channel. Near the wall, the velocity reduced to zero through a thin boundary layer. Its thickness was found to decrease with λ. Ghaly and Vatistas [1997] provided a simpler and faster numerical solution (to power series) for purely inflow and outflow. Assuming unidirectional flow, the flow excluded the entrance and exit regions. As λ increased, inward velocity flattened the governing equations were reduced to a third- order ordinary differential equation (ODE) that was written as a system of three non-linear first orders ODE s. The resulting system was

then solved as an initial value problem (IVP) using the shooting method. Pressure distributions as well as radial velocities were in fair agreement with previous experiments and also with power series solution. In a later parametric study concerning the sink flow with swirl, Ghaly and Vatistas [2001] demonstrated the effects of swirl and Reynolds number on the flow field and pressure field in a low aspect ratio vortex chamber. Assuming that the shear stress in radial direction is much than that in axial direction, the radial and tangential momentum equations were simplified. The implicit Euler's backward method was then employed to integrate the equations in the radial direction and the shooting-method for solving in the axial direction. The produced numerical results showed that increasing the swirl number caused the maximum radial velocity to shift from the gap centre line to the near wall as the centrifugal force increased. Keeping the Reynolds number constant, the radial velocity decreased with the swirl strength. Purely radial flow emerged for creeping flow Reynolds numbers.

Not long ago, Frankel & Taira [2005] performed error analysis with respect to the numerical solution of the set of equations presented in [1995] and [1997]. Ghaly and Vatistas [2001] provided results that are comparable to those obtained using the considerably more involved theoretical approaches of Frankel and Taira [2005] and Zitouni and Vatistas [1997].

Tsifouradaris [2003] performed analytical investigation for both inflow and outflow with or without swirl between two discs with very low aspect ratios. In the

analysis, the radial velocity was expressed as a function of radial location and the reduced Reynolds number while the pressure depended on the Re, the radial distance and the swirl number. In order to support the analysis, experiments at low and moderate Re numbers for several gap ratios were also conducted. The entry and exit regions were excluded. For the case of purely radial flow, viscous as well as inertia affects played an important role near inlet (after the entrance). As flow advanced, the profiles became flatter at mid gap. Increasing the inlet Reynolds number, inertia grew larger thus encouraging the radial velocity to develop at a faster rate. The effect of Reynolds number on pressure was found to be minimal. For swirling inflow, the radial velocity remained unaffected by swirl. Analytical results for the tangential velocity showed similar characteristics with radial. Based on above work, Vatistas et al [2005] extended further the analytical expression for the tangential velocity when both discs are rotating.

CHAPTER 3

Mathematical Description and Dimensional Analysis

Dimensional analysis widens and deepens every experimental, analytical, and numerical study. It provides a generalized presentation of results through a set of dimensionless parameters. The method also offers a compact description of the same phenomenon on a framework requiring fewer variables[1]. Since it reduces the effort in characterizing the same problem, dimensional analysis is economical. The great majority of the parameters correspond to a ratio between two forces. Consequently these are indicators, which show the relative importance of one force *visa vie* the other. In some flow conditions some forces could be orders of magnitude larger than others. Frequently, through an order of magnitude argument one can examine the same problem considering only the dominant forces and neglecting all those of insignificantly smaller contribution. Such an approach yields a simpler set of equations, which describe mathematically the problem that often leads either to an analytical solution or reduces considerably the computational effort.

In this chapter, the mathematical model of the flow between two stationary discs with swirl will be given with the associated equations arranged in dimensionless form.

---

[1] Equal to the number of basic dimensions involved.

The Mathematical Model

Every representation of reality must respect all the conservation and entropy laws. In our case since an isothermal flow is assumed, the conservation of mass and momentum will be paramount.

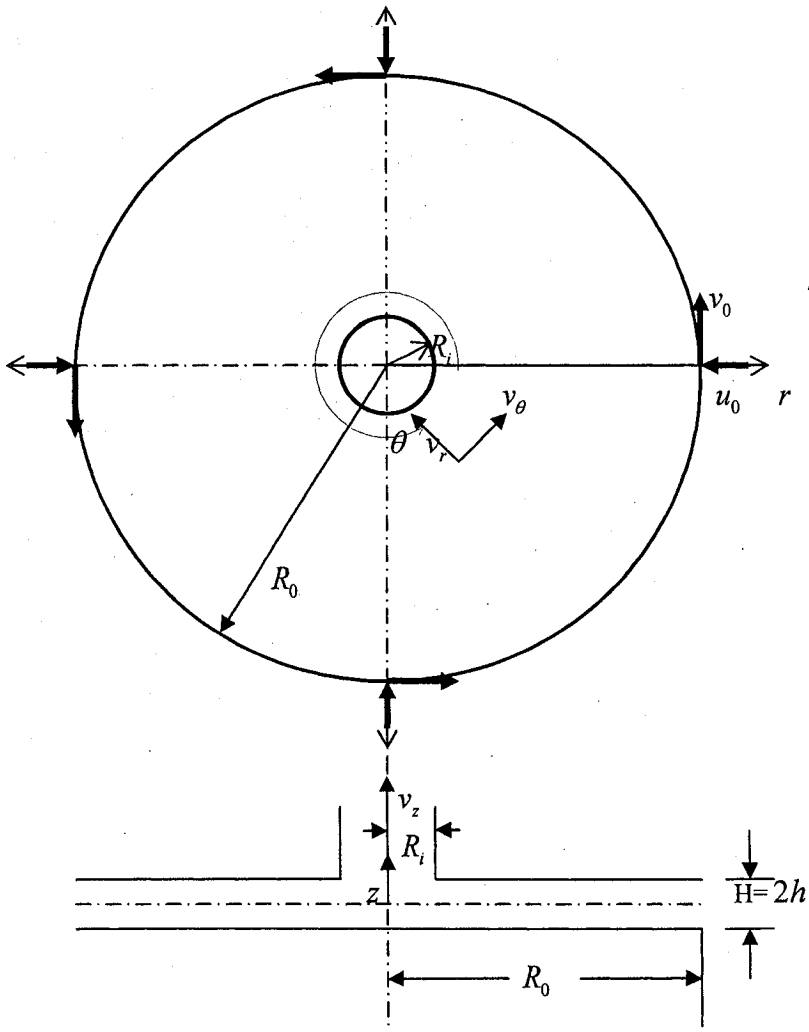

Figure 3.1: Top and side views of the setting for the flow between two discs.

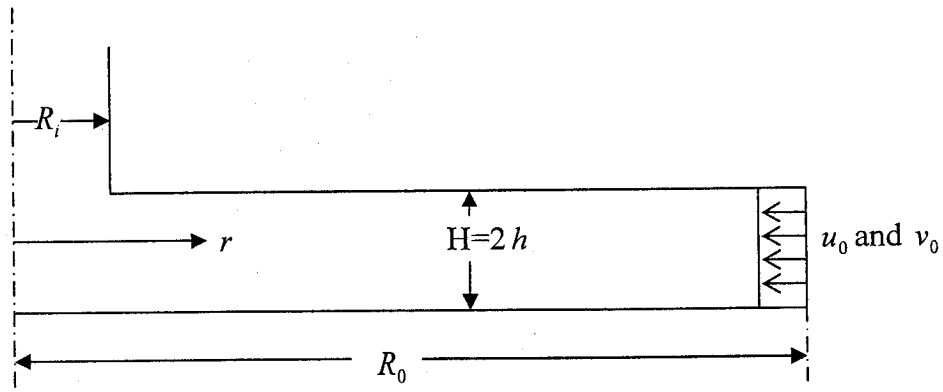

Figure 3.2 Flow problem in 2D for symmetric half.

In the present study the flow is assumed to be steady, incompressible and axi-symmetric. Under these assumptions the conservation equations and boundary conditions are,

Continuity

$$\frac{\partial v_r}{\partial r}+\frac{v_r}{r}+\frac{\partial v_z}{\partial z}=0 \tag{1}$$

r momentum

$$v_r\frac{\partial v_r}{\partial r}+v_z\frac{\partial v_r}{\partial z}-\frac{v_\theta^2}{r}=-\frac{1}{\rho}\frac{\partial p}{\partial r}+\nu[\frac{\partial^2 v_r}{\partial r^2}+\frac{1}{r}\frac{\partial v_r}{\partial r}+\frac{\partial^2 v_r}{\partial z^2}-\frac{v_r}{r^2}] \tag{2}$$

θ momentum

$$v_r\frac{\partial v_\theta}{\partial r}+v_z\frac{\partial v_\theta}{\partial z}+\frac{v_r v_\theta}{r}=\nu[\frac{\partial^2 v_\theta}{\partial r^2}+\frac{1}{r}\frac{\partial v_\theta}{\partial r}+\frac{\partial^2 v_\theta}{\partial z^2}-\frac{v_\theta}{r^2}] \tag{3}$$

z momentum

$$v_r \frac{\partial v_z}{\partial r} + v_z \frac{\partial v_z}{\partial z} = -\frac{1}{\rho}\frac{\partial p}{\partial z} + \nu\left[\frac{\partial^2 v_z}{\partial r^2} + \frac{1}{r}\frac{\partial v_z}{\partial r} + \frac{\partial^2 v_z}{\partial z^2}\right] \tag{4}$$

Boundary conditions:

a) at $r = R_0$, $v_r = u_0$, $v_z = 0$ and $v_\theta = v_0$

b) at $z = 0$, $v_r = v_z = v_\theta = 0$

c) at $z = 2h$, $r \geq R_i$, $v_r = v_z = v_\theta = 0$

d) at $z = 2h$, $r \leq R_i$, $v_r = v_r(r)$, $v_z = v_z(r)$, $v_\theta = v_\theta(r)$.

Putting the boundary conditions, the dimensionless form of above equations are:

continuity

$$\frac{1}{\eta}\frac{\partial(u\eta)}{\partial \eta} + \frac{1}{\sigma}\frac{\partial w}{\partial \varsigma} = 0 \tag{5}$$

r momentum

$$u\frac{\partial u}{\partial \eta} + \frac{1}{\sigma} w\frac{\partial u}{\partial \varsigma} - \frac{v^2}{\eta} S^2 = -\frac{\partial \Pi}{\partial \eta} + \frac{1}{\mathrm{Re}_r}\left[\frac{\partial^2 u}{\partial \eta^2} + \frac{1}{\eta}\frac{\partial u}{\partial \eta} + \frac{1}{\sigma^2}\frac{\partial^2 u}{\partial \varsigma^2} - \frac{u}{\eta^2}\right] \tag{6}$$

θ momentum

$$u\frac{\partial v}{\partial \eta} + \frac{1}{\sigma} w\frac{\partial v}{\partial \varsigma} + \frac{uv}{\eta} = \frac{1}{\mathrm{Re}_r}\left[\frac{\partial^2 v}{\partial \eta^2} + \frac{1}{\eta}\frac{\partial v}{\partial \eta} + \frac{1}{\sigma^2}\frac{\partial^2 v}{\partial \varsigma^2} - \frac{v}{\eta^2}\right] \tag{7}$$

z momentum

$$u\frac{\partial w}{\partial \eta}+\frac{R_0}{h}w\frac{\partial w}{\partial \zeta}=-\frac{1}{\sigma}\frac{\partial \Pi}{\partial \zeta}+\frac{1}{\mathrm{Re}_r}[\frac{\partial^2 w}{\partial \eta^2}+\frac{1}{\eta}\frac{\partial w}{\partial \eta}+\frac{1}{\sigma^2}\frac{\partial^2 w}{\partial \zeta^2}] \tag{8}$$

Boundary conditions:

e) at $\eta = 1$, $u = u_0$, $w = 0$ and $v = v_0$

f) at $\zeta = 0$, $u = v = w = 0$

g) at $\zeta = 1$, $\eta \geq \frac{R_i}{R_0}$, $u = v = w = 0$

h) at $\zeta = 1$, $\eta \leq \frac{R_i}{R_0}$, $u = u(\eta)$, $w = u(\eta)$ and $v = v(\eta)$.

Where:

$$u=\frac{v_r}{u_0}, \qquad v=\frac{v_\theta}{v_0}, \qquad w=\frac{v_z}{u_0}, \qquad \eta=\frac{r}{R_0}$$

$$\zeta=\frac{z}{H}, \qquad \sigma=\frac{h}{R_0}, \qquad \mathrm{Re}=\frac{u_0 h}{\nu}$$

$$S=\frac{v_0}{u_0}, \qquad \Pi=\frac{P}{\rho u_0^2}, \qquad \mathrm{Re}_r=\frac{\mathrm{Re}}{\sigma}=\frac{u_0 R_0}{\nu}$$

CHAPTER 4

Numerical Modeling

In this chapter, the numerical study is presented. The selection of the numerical model, the grid, the selection and imposition of the boundary conditions along with the solution procedure used to simulate the flow problem will be discussed.

Steady, turbulent, incompressible, axi-symmetric converging flow with and without swirl has been modeled numerically using the FLUENT 6.1 solver. As there are no circumferential gradients in the flow, modeling was accomplished using 2D segregated solver. For purely sink flow, Singh [1993] used the low Reynolds number k-ε model in his numerical solution. Expecting severe case of streamline bending to occur, the Reynolds Stress Model is employed instead. Test performed for the swirling flow case, k-ε model failed to simulate the flow characteristics to the expected fidelity.

For the case of swirling inflow, conservation of angular momentum plays a vital role in the creation of a Rankine-like [1858] combined vortex where the tangential velocity increases sharply as the radius decreases and then reducing to zero at the sink center. Centrifugal forces developed by the circumferential motion in the free vortex region are in equilibrium with the radial pressure gradient. For a non-ideal vortex, the form of these radial pressure gradient changes, driving radial and axial flows in response to a highly non-uniform pressure. High degree of coupling between

the swirl and the pressure field makes the modeling of swirling flows complex. The Reynolds Stress Model (RSM) is suitable to resolve the latter impediment. FLUENT 6.1 is able to take account of these variations in the static pressure and the corresponding changes in the axial and radial velocities as well as tangential components.

4.1 Selecting the turbulence model:

Selection of turbulence model depends on the physics of fluid flow and no single model can be considered as acceptable for all types of problems [Fluent, 2003]. For example, two equations $k-\varepsilon$ model can be applied where there is no or very little streamline bending taking place such as for the purely radial inflow or very weak swirling inflow away from the outlet . But in the case of strong swirling flow, where streamlines curve severely, RSM five equations for 2D geometry and 7 equations for 3D can predict the flow characteristics accurately. The choice of the model primarily depends on the expected vortex strength measured by the swirl ratio,

$$S = \frac{v_\theta}{v_r}.$$

Flows with no swirl (S=0) or weak to moderate swirl ($S \leq 0.5$) $k-\varepsilon$ model can be employed. Nevertheless, both the RNG $k-\varepsilon$ model and the realizable $k-\varepsilon$ model can provide better results than the standard $k-\varepsilon$ model. However, if $S \geq 0.5$, the effect of strong turbulence anisotropy due to strong swirl can be modeled adequately via the second-moment closure introduced in the RSM. Besides the swirl number, the level of accuracy required, the available computational resources, and the amount of time

available for the simulation are also important factors in the selection of the approximate turbulence model (more details can be found in the Fluent 6.1, Manual).

Importance will be given now to the determination of which part of the turbulent Navier-Stocks equations (of Ensemble Averaging approach) is important for the present modeling using the RSM.

4.1.1 Reynolds (Ensemble) Averaging

Reynolds –Averaging approach requires much less computational capacity rather than the more involved Large Eddy Simulation (LES). The transport equations for the mean flow with all the scales of turbulence are represented by the RANS (Reynolds- Averaged Navier- Stocks) equations. Filtering is introduced to remove eddies smaller than the mesh size. In this approach, Navier-Stocks equations are decomposed into the mean and fluctuating components;

$$v_i = \overline{v}_i + v'_i \tag{9}$$

Where, $\overline{v}_i$ is the mean and v'_i is the fluctuating velocity component.

The pressure and other scalar quantities can be written:

$$\phi = \overline{\phi} + \phi' \tag{10}$$

Here ϕ denotes a scalar such as the pressure or say energy.

Substitution of the above forms into continuity and momentum equations and taking a time (or ensemble) average gives the RNAS equations in Cartesian coordinate,

$$\frac{\partial \rho}{\partial t} + \frac{\partial (\rho v_i)}{\partial x_i} = 0 \tag{11}$$

$$\frac{\partial (\rho v_i)}{\partial t} + \frac{\partial (\rho v_i v_j)}{\partial x_j} = -\frac{\partial p}{\partial x_i} + \frac{\partial}{\partial x_j}\{\mu[\frac{\partial v_i}{\partial x_j} + \frac{\partial v_j}{\partial x_i} - \frac{2}{3}\delta_{ij}\frac{\partial v_l}{\partial x_l}]\} + \frac{\partial (-\rho \overline{v'_i v'_j})}{\partial x_j} \tag{12}$$

Where, δ_{ij} is the Kronecker delta. Here $\frac{\partial}{\partial t}$ is zero, ρ is constant (steady, incompressible flow).

The additional terms that now appear in the momentum equations are the Reynolds stresses that represent the effect of turbulence. For closure, the Reynolds stresses $\rho \overline{v'_i v'_j}$, must be modeled. In order to solve the problem, the term $\rho \overline{v'_i v'_j}$ must be expressed in terms of the known variable can be achieved using Boussinesq's hypothesis [1975] which also includes the different k-ε models and Reynolds stresses transport models (RSM and Algebraic Stress Model where FLUENT 6.1 deals with only RSM).

The Boussinesq hypothesis [1975] relates the Reynolds stresses to the mean velocity gradients,

$$\rho\overline{v'_i v'_j} = \mu_t\left(\frac{\partial v_i}{\partial x_j} + \frac{\partial v_j}{\partial x_i}\right) - \frac{2}{3}\left(\rho k + \mu_t \frac{\partial v_i}{\partial x_i}\right)\delta_{ij} \qquad (13)$$

Where $\mu_t \left(= \rho C_\mu \frac{k^2}{\varepsilon}\right)$ is the eddy viscosity, $k \left(= \frac{\overline{v'_i v'_i}}{2}\right)$ turbulent kinetic energy and ε is dissipation rate and $C_\mu = 0.09$ is constant.

To close the momentum equation (12), one needs the values of the Reynolds Stresses in equation (13).Then the value of k and ε are required as an input. Assuming the flow is fully turbulent and the effects of molecular viscosity are negligible, the standard k-ε model (semi-empirical model) became more popular to model various practical engineering flow calculations due to its robustness, economy, and reasonable accuracy for a wide range of uses [Fluent, 2003]. Due to its limitation in simulating the flow with stream line bending, two other models were modified from standard k-ε model to solve this problem. One of them is Realizable k-ε model proposed by Shih et al. [1995] where another one is the Re-Normalization Group RNG) theory that proposed by Yakhot and Orszag [1986] and by Choudhury [1993].

Although the above mentioned two models have been considered for the swirling flow phenomenon (up to medium strength), for very strong swirl (S $\geq$5), none of above models is able to produce results comparable with experiment. The Reynolds Stress Model (RSM), the most elaborate one, is applicable to predict such flows.

4.1.2 Reynolds Stress Model:

Rather than the eddy-viscosity hypothesis, RSM solves five additional transport equations for the Reynolds stresses in 2D flows and seven additional transport equations in 3D together with an equation for the dissipation rate to closes the RANS equations.

The transport equations for Reynolds stresses, $\rho\overline{v'_i v'_j}$ in tensorial form are:

$$\underbrace{\frac{\partial}{\partial t}\{\rho\overline{v'_i v'_j}\}}_{\text{i}} + \underbrace{\frac{\partial}{\partial x_k}\{\rho v_k \overline{v'_i v'_j}\}}_{\text{ii}} = - \underbrace{\frac{\partial}{\partial x_k}\{\rho\overline{v'_i v'_j v'_k} + \overline{p(\delta_{kj} v'_i + \delta_{ik} v'_j)}\}}_{\text{iii}}$$

$$+ \underbrace{\frac{\partial}{\partial x_k}\{\mu\frac{\partial}{\partial x_k}(\overline{v'_i v'_j})\}}_{\text{iv}} - \underbrace{\rho\{(\overline{v'_i v'_k})\frac{\partial v_j}{\partial x_k} + (\overline{v'_j v'_k})\frac{\partial v_i}{\partial x_k}\}}_{\text{v}} - \underbrace{\rho\beta\{g_i\overline{v'_j\theta} + g_j\overline{v'_i\theta}\}}_{\text{vi}}$$

$$+ \underbrace{\overline{p\{\frac{\partial v'_i}{\partial x_j} + \frac{\partial v'_j}{\partial x_i}\}}}_{\text{vii}} - \underbrace{2\mu\overline{\frac{\partial v'_i}{\partial x_k}\frac{\partial v'_j}{\partial x_k}}}_{\text{viii}} - \underbrace{2\rho\Omega_k\{\overline{v'_j v'_m}\varepsilon_{ikm} + \overline{v'_i v'_m}\varepsilon_{jkm}\}}_{\text{ix}}$$

$$+ \underbrace{S}_{\text{x}} \qquad (14)$$

Where, i = Local time derivative (zero for present steady flow), ii= Convection C_{ij}, iii = Turbulent diffusion, $D_{T,ij}$, iv = Molicular Diffusion $D_{L,ij}$, v = Stress production P_{ij}, vi = Buoyancy production G_{ij} (Neglected in this case), vii = Pressure strain ϕ_{ij}, viii = Dissipation tensor ε_{ij}, ix = production by system rotation F_{ij} (zero, present study), x = Source term S (zero).

$C_{ij}, D_{L,ij}$ and P_{ij} are not required to model [Fluent, 2003]. So one has to calculate $\phi_{ij}, D_{T,ij}, \varepsilon_{ij}$ terms to close these exact equations.

Daly and Harlow [1970] proposed following formula to generalize the diffusion gradient $D_{T,ij}$;

$$D_{T,ij} = c_s \frac{\partial}{\partial x_k}\{\rho \frac{k\overline{v'_k v'_l}}{\varepsilon} \frac{\partial(\overline{v'_i v'_j})}{\partial x_l}\} \tag{15}$$

Concerning the numerical instabilities, it is simplified in FLUENT 6.1 according to Lien and Leschziner [1994] with the relation;

$$D_{T,ij} = \frac{\partial}{\partial x_k}\{\frac{\mu_t}{\sigma_k} \frac{\partial(\overline{v'_i v'_j})}{\partial x_k}\} \tag{16}$$

Where, turbulent viscosity $\mu_t = \rho C_\mu \frac{k^2}{\varepsilon}$ similar to the standard k-ε model and σ_k= 0.82. The pressure-strain term ϕ_{ij} is modeled using different theories one of which is called Linear Pressure-Strain Model proposed by Gibson and Launder [1978], Fu et al. [1987], and Launder [1989] with Low-Re Modifications for near-wall flows using the enhanced wall treatment. Another model that is called Quadratic Pressure-Strain Model proposed by Speziale, Sarkar, and Gatski [1991] (See Fluent Manual, 2003 for details). However, Linear Pressure-Strain Model was used to model ϕ_{ij}. In modeling a specific term, the turbulent kinetic energy can be calculated by $k = \frac{\overline{v'_i v'_i}}{2}$.

Therefore, to solve transport equation for the turbulent kinetic energy k, in order to obtain boundary conditions for the Reynolds stresses, Fluent uses the following conservation equation,

$$\frac{\partial(\rho k)}{\partial t}+\frac{\partial(\rho k v_i)}{\partial x_i}=\frac{\partial}{\partial x_j}[(\mu+\frac{\mu_t}{\sigma_k})\frac{\partial k}{\partial x_j}]+\frac{1}{2}(P_{ii}+G_{ii})-\rho\varepsilon(1+2M^2{}_t)+S_k \qquad (17)$$

Equation (17) is solved globally throughout the flow domain and is identical with k-ε model when σ_k=0.82. The dissipation tensor ε_{ij} is calculated from $\varepsilon_{ij}=\frac{2}{3}\delta_{ij}(\rho\varepsilon+Y_M)$ where, $Y_M=2\rho\varepsilon M_t^2$. M_t is turbulent Mach number, which can be defined as; $M_t=\sqrt{\frac{k}{a^2}}$ here $a=\sqrt{\gamma RT}$ sound speed.

Similar to the standard k-ε model, the dissipation rate ε is approximated using the following relation,

$$\frac{\partial(\rho\varepsilon)}{\partial t}+\frac{\partial(\rho\varepsilon v_i)}{\partial x_i}=\frac{\partial}{\partial x_j}[(\mu+\frac{\mu_t}{\sigma_\varepsilon})\frac{\partial\varepsilon}{\partial x_j}]+C_{\varepsilon 1}\frac{\varepsilon}{2k}(P_{ii}+C_{\varepsilon 3}G_{ii})-C_{\varepsilon 2}\rho\frac{\varepsilon^2}{k}+S_\varepsilon \qquad (18)$$

where σ_ε=1.0, $C_{\varepsilon 1}$=1.44, $C_{\varepsilon 2}$=1.92. The constant $C_{\varepsilon 3}$ is a function of the local flow direction relative to the gravitational vector.

4.1.3 Computational Time:

Computational time per iteration is important for the choice of the turbulence model. For example, the standard **k-ε** model requires the least amount of memory rather than any other models. Because the RSM solves a larger number of equations for the Reynolds stresses, requires 50-60% more CPU time per iteration compared to the k-ε model [Fluent, 2003]. For modeling the flow in the present domain, RSM is found to be feasible with optimum mesh size.

4.2 NUMERICAL SIMULATION: Numerical simulation is the crucial part for the numerical modeling which can be divided into three stages; Pre-processing, selecting the solver that will solve the turbulent Navier-Stokes equations, and post-processing.

4.2.1 Pre-processor:

Pre-processing includes the clear definition of the physical phenomenon that needs to be solved, selecting and creating the suitable flow geometry of the domain, optimum mesh generation for this domain, the setting-up of the appropriate boundary condition based on geometry and physics of flow. The physical phenomena studied here is the turbulent in-flow between two stationary discs without and with swirl. As the flow is converging, pressure is decreasing with the increasing radial and swirl velocity components with the swirl enhancing turbulence. When the influence of swirl or the rotational terms is large, high degree of coupling between the momentum

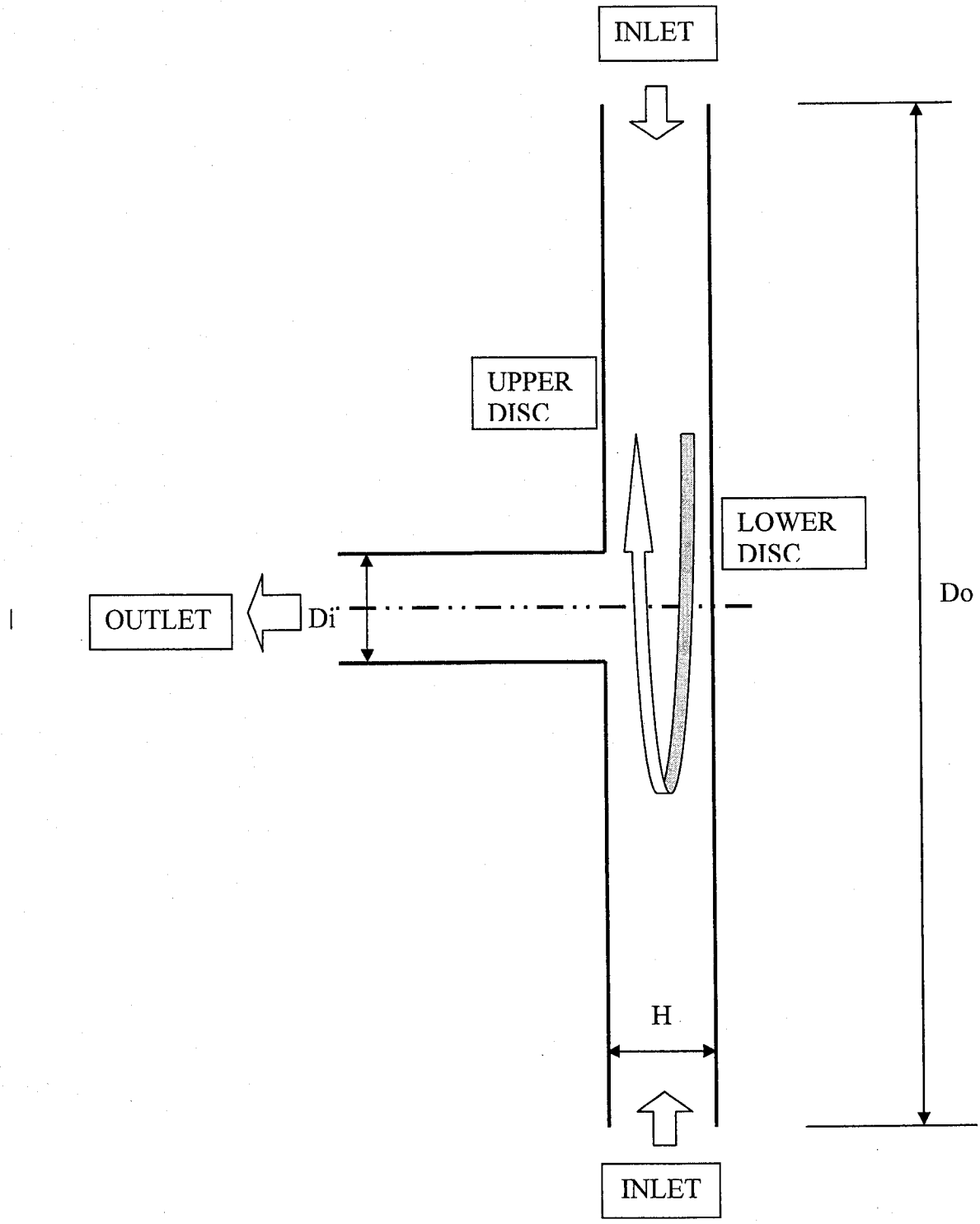

Figure 4.1: 2D geometry for the numerical modeling

equation introduces difficulties in the domain and thus to the solution of the flow. These impediments are related to the large radial pressure gradient which drives the flow in the axial and radial directions and to the ensuing complex forces in the flow. Instabilities in the solution process may result from this coupling and sometimes making very difficult to obtain a converged solution [Fluent, 2003].

i) The Computational domain

Axi-symmetry implies that there are no circumferential gradients in the flow and therefore a two-dimensional geometry (figure 4.1) can be adopted in order to define the physical phenomenon. Here Do (=2 R_0) is the disc diameter, Di (=2 R_i) is the diameter of the outlet located at the centre of the upper disc. H (=2 h) is the gap between the two discs. These dimensions are varying for purely radial inflow and swirling inflow as different cases were examined to compare with existing experiments.

ii) The Grid Size Study

For an axi-symmetric problem, it is strongly recommended to set the grid in such a way that if the axis of rotation is x axis, then the grid must be located on or above the y=0 line. Sufficient resolution in grid should also be taken care when solving flows that include swirl or rotation because, swirling flow will often involve steep gradients in the tangential velocity requiring fine grids for accurate resolution [Fluent, 2003].

From the Figure 4.1, it is clear that the geometry of flow is symmetrical. So meshing the half portion of this configuration will be capable to calculate full domain. Grid study was evaluated by selecting optimum grid types and size as wall as considering their effect on solution.

a) Selecting the appropriate Grid Type:

The choice of mesh type usually depends on the engineering application. Set-up time, Computational expense and Numerical diffusion are important to select an appropriate grid type.

a.1) Set-up time:

In general, for complex geometries, it is preferable to employ unstructured grids with triangular or quadrilateral cells in order to save meshing time, but a simple geometry can be graded with both structured and unstructured approaches.

a.2) Computational Expense:

In the case of complex or very large geometries, a triangular mesh gives less numbers of cells than an equivalent quadrilateral mesh. Because, the structured quadrilateral mesh enforces cells to place at the regions where they are not required. However, quadrilateral meshes offer many advantages over triangular meshes in grading simple and moderately-complex shapes. For example, quadrilateral elements are more inexpensive in some situations as they permit much larger aspect ratio than triangular types. Besides, large aspect ratio in a triangular cell can affect the skewness

of the cell, which may lead the solution to inaccuracies and obstruct convergence [Fluent, 2003]. Therefore, for relatively simple geometries quadrilateral mesh is recommended.

a.3) Numerical diffusion:

Numerical diffusion (false diffusion) is one of the dominant sources of error in numerical calculations because it affects the flow calculation in the same manner as if increasing the real diffusion coefficient. Second-order discretization scheme is helpful to reduce the effects of numerical diffusion in the solution. Moreover, the amount of numerical diffusion is inversely related to the resolution of the mesh. Hence, one way of avoiding the effect of numerical diffusion is using a fine mesh. Above all, it can be minimized when the flow is aligned with the mesh [Fluent, 2003]. This is the most relevant factor in the choice of grid. When grading is done with triangular mesh instead of quadrilateral category, it can not be possible to make the grid parallel to the flow.

Objective of study is the mean turbulent flow rather than boundary layer solution. So, uniform distribution of mesh (equal interval size with successive ratio every where the domain) is able to predict the solution correctly. However, grading with finer mesh at boundary layer was also examined and obtained results were similar to the previous approach. Geometry was drawn and meshed by GAMBIT 2.2 that offers quadrilateral (map, sub-map, pave) and triangular (pave only) face meshing schemes. Basically, quadrilateral mapping (structured mesh) deals with the

shape which can easily be divided or sub-divided in the form of quadrates [Fluent, 2003].

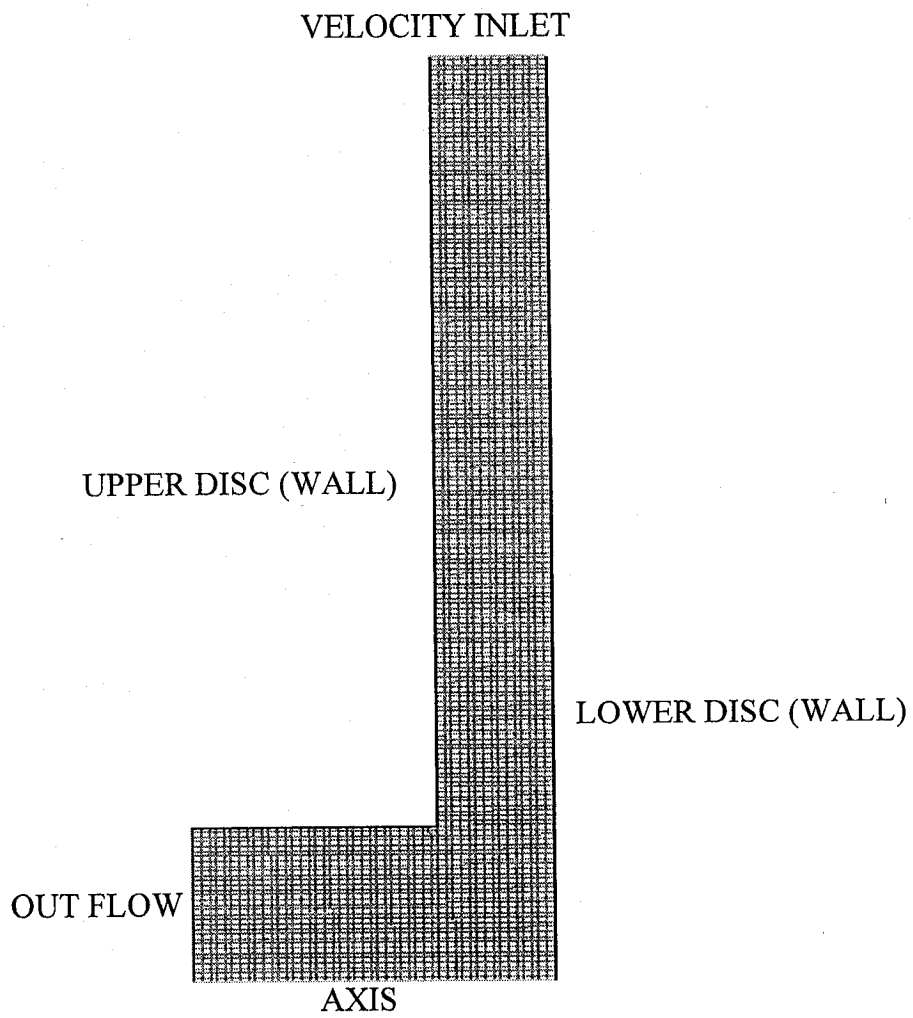

Figure 4.2: Quadrilateral uniform face mesh on the domain for purely sink-flow according to the setup of Singh [1993].

If the contour is not one quadrate but the combination of two or more quadrates (as figure 4.2) then sub-mapping (of quadrilateral) are more useful than triangular one. Because of the flow complexity, both the quadratic and triangular types were checked for present investigation and same results were achieved. Therefore, present problem is independent on mesh types.

Finally, triangular mesh of same interval size to the quadrilateral one produces much more numbers of elements (hence, more computational ability required). Therefore, quadrilateral meshing scheme was chosen to study this problem.

b) Effect of grid on solution:

Grid Size (interval size of face) (mm)	Number of Cells	Number of Faces	Number of Nodes
1	2324	4832	2509
0.8	3889	8016	4128
0.6	6844	14004	7161
0.4	15462	31398	15937
0.3	27545	55723	28179
0.2	61849	124647	62799
0.15	109841	220947	111107
0.14	126596	254548	127953
0.13	146044	293548	147505
0.12	171944	345470	173527

Table 4.1: Details of different mesh size and number of cells, faces and nodes for purely sink flow.

1) Purely sink flow:

In order to determine the grid dependence on the purely radial inflow, the geometry of experimental settings for Singh [1993] was chosen where, the radius of discs, R_0 = 152.4 mm, radius of sink outlet, R_i = 25.4 mm, Gap, H = 12 mm., with flow rate 19.71E-0.03 m3/s. Figure 4.2 shows the grid scheme for this setting. Different grid sizes that were examined to get optimum mesh are described in table 4.1.

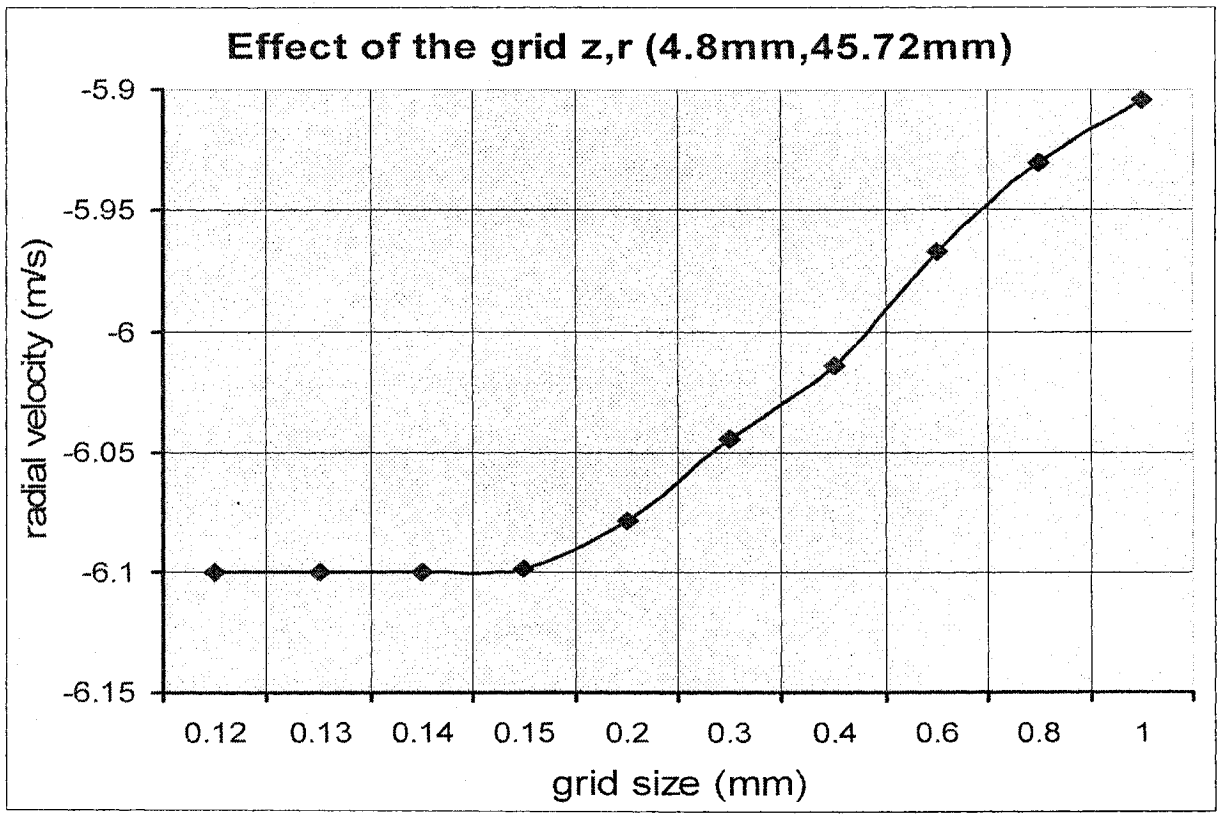

Figure 4.3(a): Radial velocity (m/s) Vs. grid size (mm) of the solution for purely sink flow [Singh, 1993] at the point (4.8mm, 45.72mm).

The effects of mesh sizes on the radial velocity at two different points are shown by graphical representation (figure: 4.3). From the Figure 4.3; it's very clear that after the mesh size 0.3 mm, the change in the solution is negligible as the difference is not exceeding 0.576 %. Table 4.1; shows the finer mesh size is, the more number of cells, number of nodes as wall as number of faces which concern the computational time and memory. So, optimum mesh size can be selected between 0.2 mm and 0.3 mm for this flow problem.

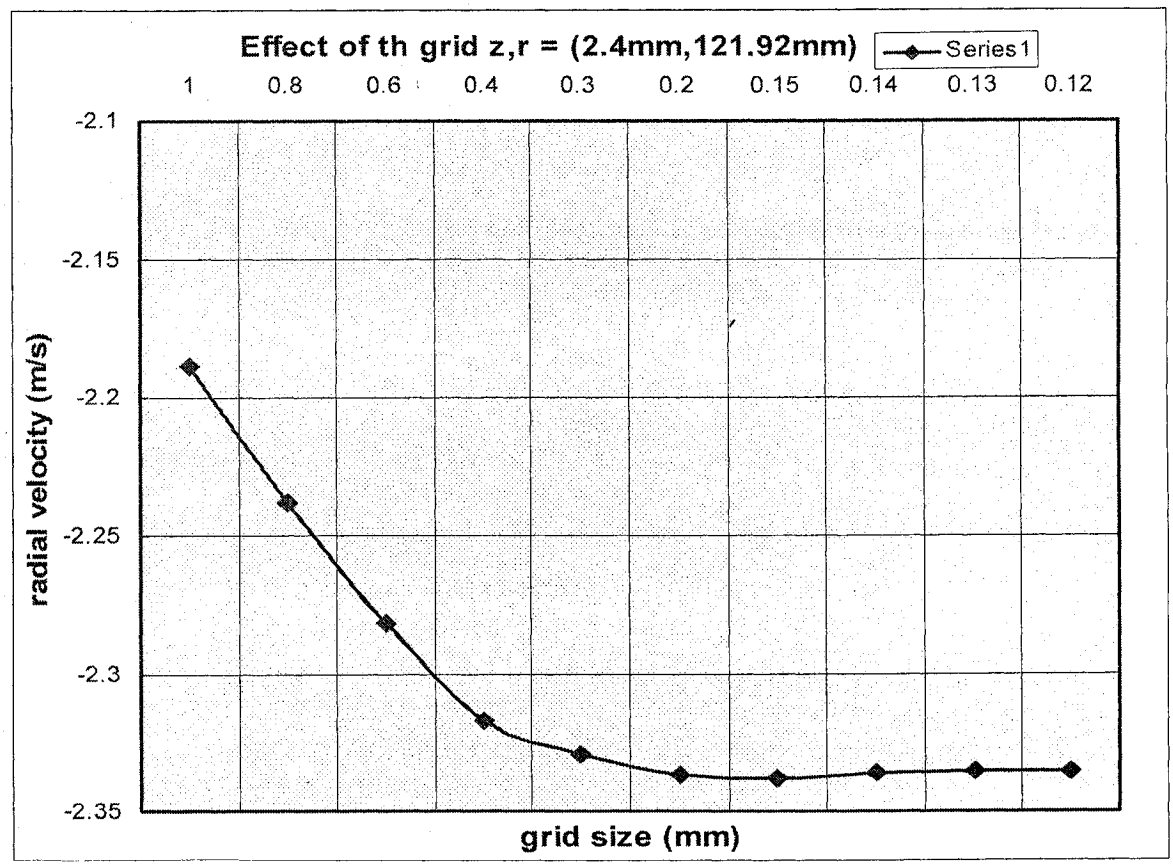

Figure 4.3(b): Radial velocity (m/s) Vs. grid size (mm) of the solution for purely sink flow [Singh, 1993] at the point (2.4mm, 121.92mm).

2) Swirling inflow:

For swirling inflow, the experimental setting of Savino and Keshock [1965] was drawn and graded (figure 4.4) which is pretty similar to the setup of purely radial flow with different dimensions.

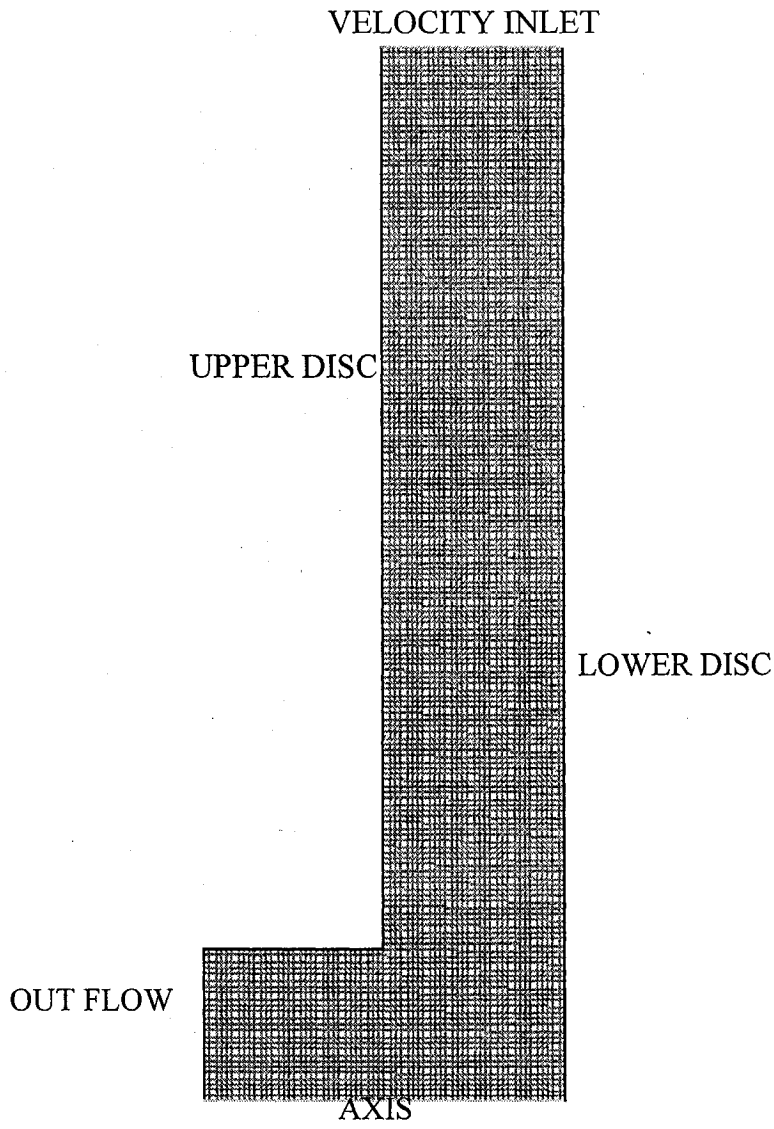

Figure 4.4: Quadrilateral uniform face mesh on the domain for swirling inflow according to the setup of Savino and Keshock [1965].

In this case, the radius of discs, R_0 = 148.844 mm (5.86 in), radius of sink outlet, R_i = 25.4 mm (1 in), Gap H = 31.75 mm (1.25 in). The given mass flow rate is 0.209 pound mass per second with inlet radial swirl ratio $S \cong 15$.

In the original experimental test section, the inlet velocity was given as average velocity. As no velocity profile was given, assuming uniform inlet velocity would lead to an improper boundary condition that could affect the solution.

Consequently, an inlet velocity profile is needed as an appropriate boundary condition. This requirement can be satisfied in two ways; namely writing the profile as a user defined function or extending the diameter of discs and putting a uniform velocity distribution at the inlet section.

Grid Size (interval size of face) (mm)	Number of Cells	Number of Faces	Number of Nodes
1	6368	12974	6607
0.8	10000	20298	10299
0.6	17596	35588	17993
0.5	25600	51677	26078
0.48	27456	55407	27952
0.46	29946	60409	30464
0.45	31453	63435	31983
0.44	32688	65916	33229
0.43	34336	69225	34890
0.42	36100	72767	36668
0.41	37561	75702	38142

Table 4.2: Details of different mesh size and number of cells, faces and nodes for swirling inflow.

In the present numerical study, disks radius was increased to 1 inch more than experimental test section for above purpose. Therefore, the total disc radius became 174.244 mm (6.86 in).

Figure 4.4 shows all the settings for computation that are same as purely sink flow except extending radial portion. Here, velocity inlet was defined at inlet, wall at upper and lower discs, out flow condition at outlet and axis at the centre line. The choice of 1 in. extension of given radius was confirmed after making some investigations on that. For example, using 1.5 inch and 2 inches instead of 1 inch gave same profile at concerned radius (5.86 inches of test section). However, 1 in increment was chosen to save computational time.

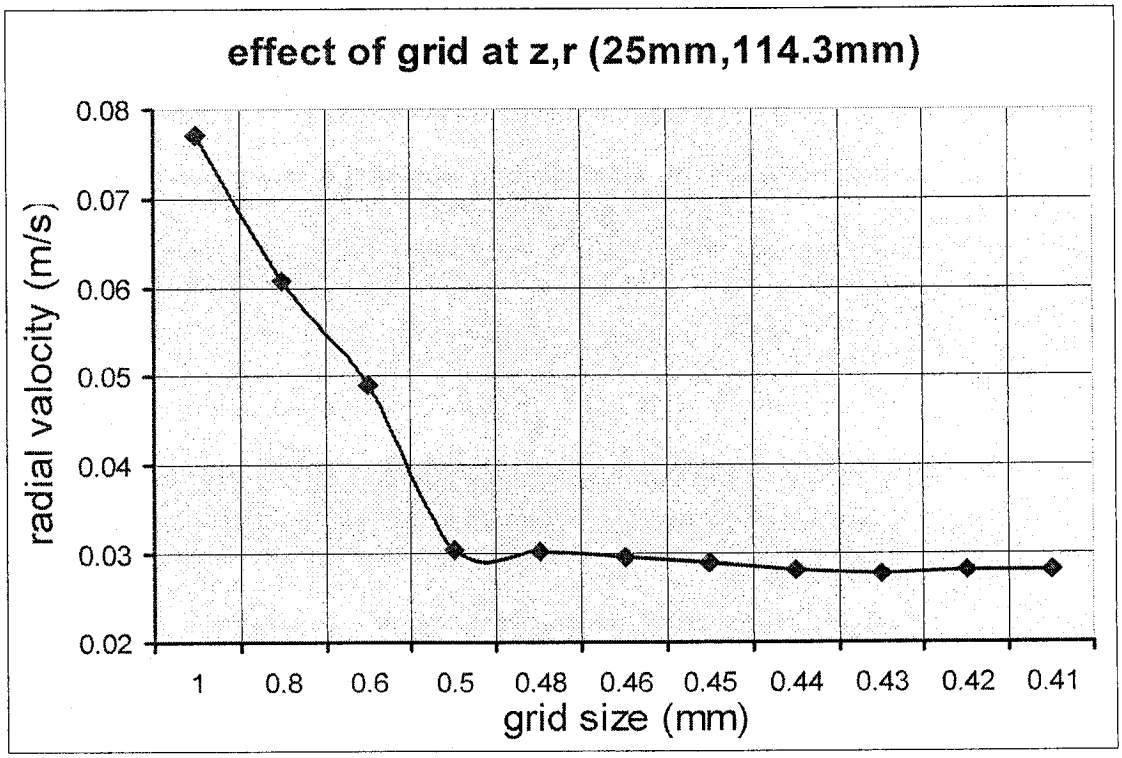

Figure 4.5(a): Radial velocity (m/s) Vs. grid size (mm) for swirling inflow [Savino and Keshock, 1965] at the point (25mm, 114.3mm).

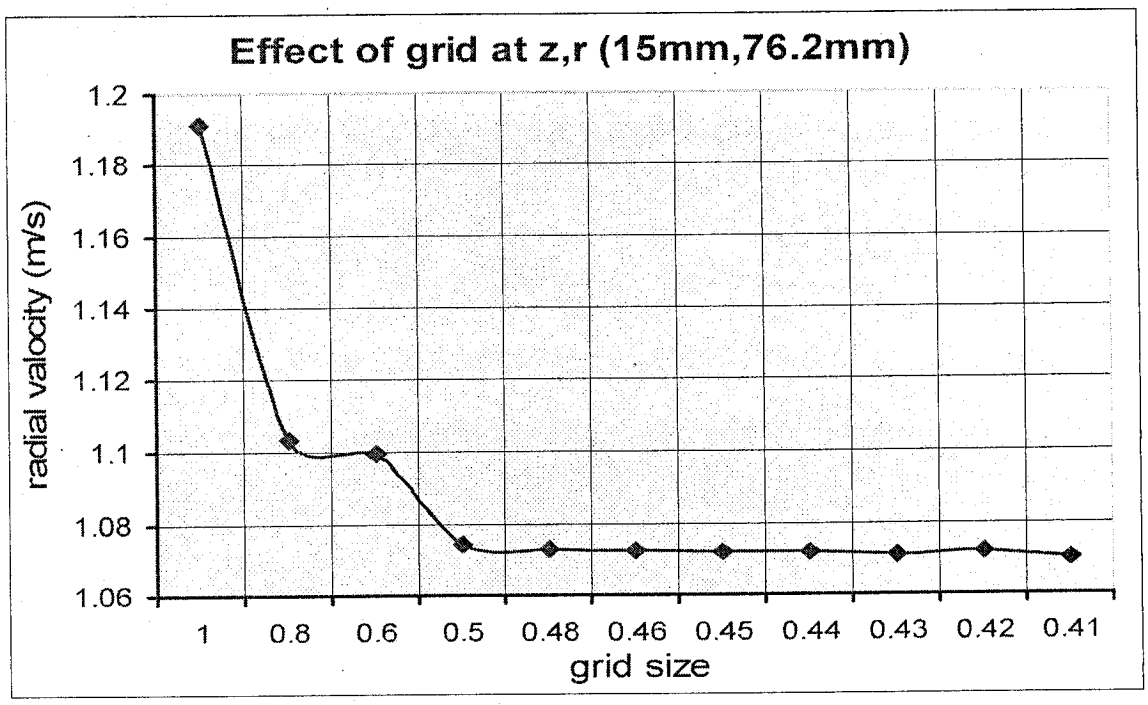

Figure 4.5(b): Radial velocity (m/s) Vs. grid size (mm) for swirling inflow [Savino and Keshock ,1965] at the point (15mm, 76.2 mm).

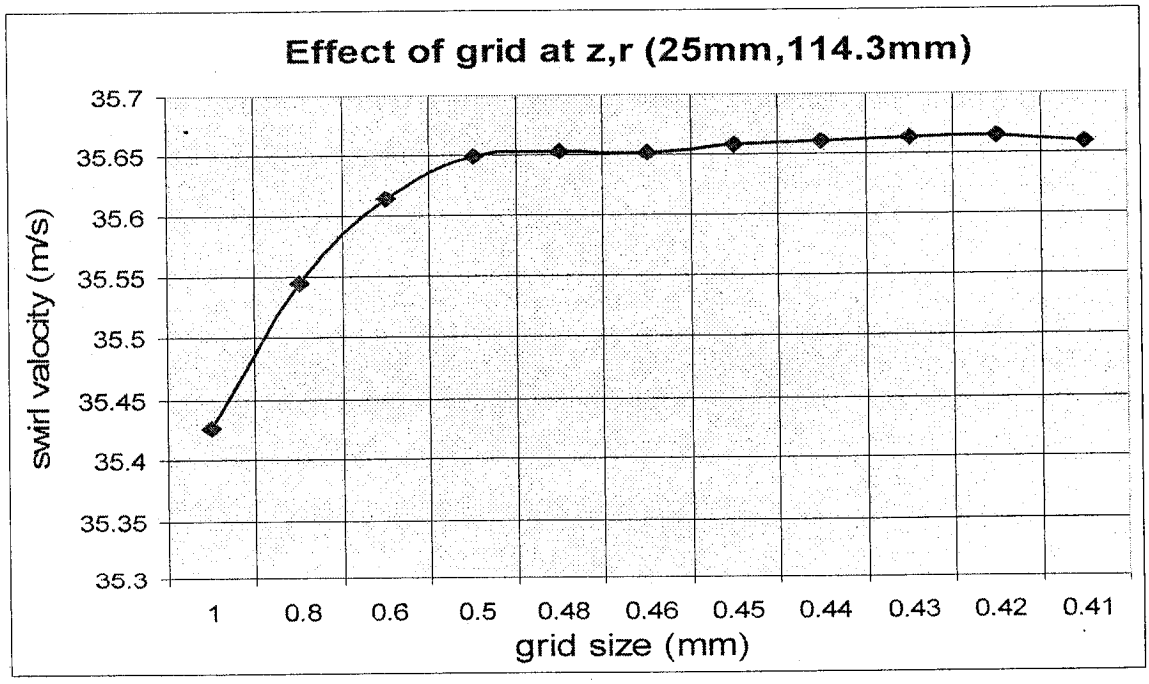

Figure 4.6(a): Swirl velocity (m/s) Vs. grid size (mm) for swirling inflow [Savino and Keshock ,1965] at the point (25mm, 114.3 mm).

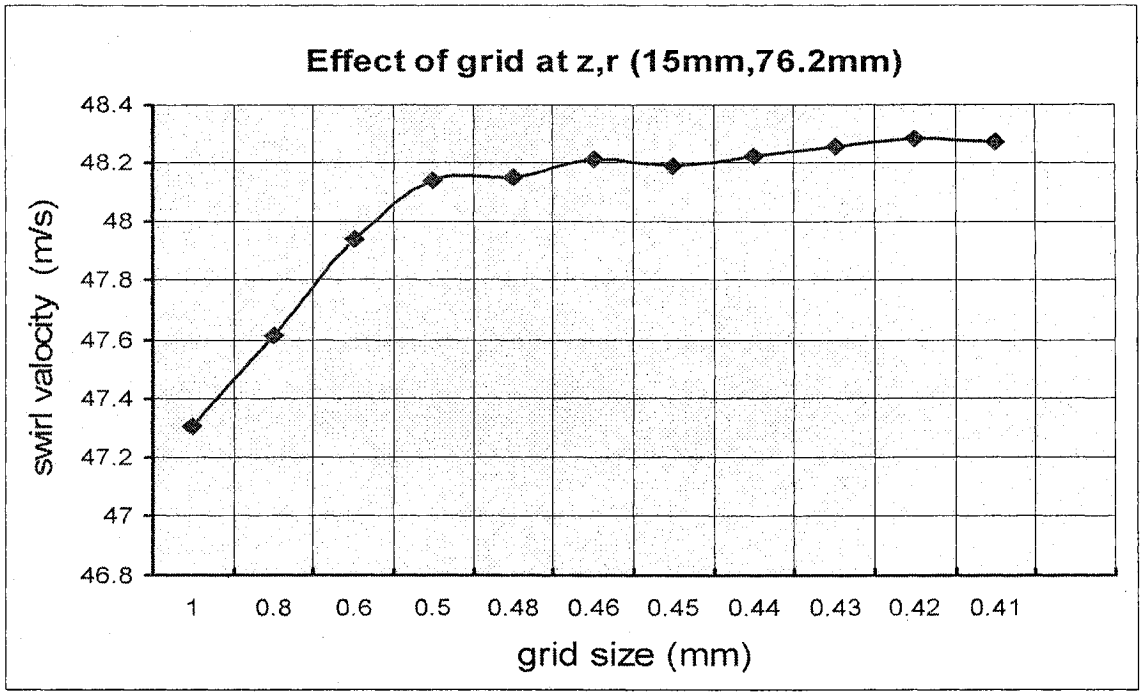

Figure 4.6(b): Radial velocity (m/s) Vs. grid size (mm) for swirling inflow [Savino and

Keshock, 1965] at the point (15mm, 76.2 mm).

Figure 4.4; displays the grid on domain and different sizes of grid that was selected to study are listed in table 4.2. Effects of grid size on radial and swirling velocity at two different points are represented in fig 4.5 and fig 4.6.

Figure 4.5 and figure 4.6 indicates that grid smaller than 0.48 sizes has minimal effect on changing the solution criteria. Again, from the point of view of computational memory and time, face mesh with the size between 0.48 and 0.45 can be selected as optimum one to get approximate numerical solution of the problem.

4.2.2 Solver:

After grading and setting boundary conditions in GAMBIT 2.2, the file exported as mesh file which was opened in FLUENT 6.1 as case file. Then file was run using steady, incompressible axisymmetric, 2D segregated solver for purely sink flow and axisymmetric swirl solver for swirling in-flow. Different settings and parameters choose to solve the turbulent Navier-Stokes equations are as follows.

i) Grid checking:

The first action taken place after reading the case file in FLUENT 6.1 is to check the grid using 'grid check' command to detect any grid trouble before get started with the problem setup. Skewness-based smoothing of mesh can be possible to perform where it sets the minimum cell skewness value to 0.4 for 2D geometry. 'Smooth' command tries to move interior nodes if required to improve the skewness of cells greater than minimum value. 'Swap' command exchanges the faces of cells for any disorder. All of these actions accomplished with some number of iterations and helpful to see whether it is possible to get solution using this grid set up or not. For example, if any negative areas or volumes in the grid are detected by checking command indicates the incapability of achieving the solution [Fluent, 2003]. However, because of the simplicity that we have in our domain this step has minimal effect in our cases of study.

ii) Scaling grid and defining units:

Grid was created in mm for both cases but units were defined differently as experiments. Following table describes the details.

Flow	Length	density	viscosity	velocity	pressure	Temp.	Mass flow rate
Purely sink	mm	Kg/m3	Kg/m-s	m/s	Pascal	K	Kg/s
Swirling inflow	mm	lbm/ft3	Kg/m-s	ft/s	Pascal	F	lbm/s

Table 4.3: Different units used in solution.

iii) Defining turbulent model:

For both of the swirling and non-swirling flow, Reynolds-Stress Model needs to define the model constants. Constants were selected as given in the solver by default. Such as, $C_{\mu} = 0.09, C_{1\varepsilon} = 1.44$, $C_{2\varepsilon} = 1.92$, turbulent Prandtl number for kinetic energy $\sigma_k = 1.0$, turbulent Prandtl number for dissipation rate σ_{ε}=1.3. In the Reynolds-Stress option in solver, wall boundary condition from k equation with standard wall function was chosen for the near wall treatment. Because, standard wall functions are able to give reasonably accurate predictions for the majority of high-Reynolds-number, wall-bounded flows. Later is applicable if there is no blowing or

suction as well as no severe pressure gradients takes places or when the flow situations do not depart far away from the ideal conditions [Fluent, 2003].

iv) Defining material:

The material flow inside the domain was air and the properties of material at inlet were set as given in experiments as the following table.

Flow type	Material	Density	Viscosity	Pressure	Temperature
Purely radial flow	Air	1.225 kg/m3	1.7894e-05 kg/m-s	101325 Pascal	300 degree K
Swirling flow	Air	0.106326 lbm/ft3	2.29e-05 kg/m-s	101325 Pascal	299.82degree K

Table 4.4: Material and properties at inlet.

v) Defining Boundary conditions:

Velocities were specified at domain inlet by three components such as axial, radial, and Swirl (in the case of swirling in-flow) velocity. In every case, the axial velocity was zero at the inlet, the flow was normal to the gap.

Radial velocity was calculated from the volumetric flow rate by the following equation.

$$v_r = -\frac{Q}{4\pi R^2_o G} \qquad (19)$$

Where, v_r = Radial Velocity with (-) sign indicates the direction of flow toward the centre. Q = Volume flow rate,

R_o = Disc radius,

$G = \frac{H}{D}$ = aspect ratio, H = Gap size, D = Disc diameter.

Tangential velocity (in case of swirling flow) was calculated from the swirl ratio where,

$$\text{Swirl ratio, } S = \frac{v_\theta}{v_r} = \text{tangential/ radial velocity} \qquad (20)$$

vi) Turbulence specification method:

In general, higher level of turbulence is produced within shear layer which is relatively insensitive to the in-flow boundary value for the numerical calculation. However, it is important to ensure the boundary value not to be so unphysical that can contaminate the solution or obstruct the solution convergence. Turbulent intensity and Hydraulic Diameter specification method is strongly recommended to model internal turbulent flows [Fluent, 2003].

a) Turbulence intensity:

The turbulence intensity can be defined as the ratio of the root-mean-square of the velocity fluctuations, v_{rms}, to the average velocity v_{av};

$$I = \frac{v_{rms}}{v_{av}} \qquad (21)$$

Physically, turbulence is instability generated by shear and its intensity is increased by the increase of shear. So, the turbulence level can be scaled by $v_{rms} \rightarrow \frac{\partial v_{av}}{\partial y}$. But this scaling is not dimensionally consistent. To solve this problem, shear strength can be replaced by shear velocity or frictional velocity based on the wall shear stress;

$$v^* = \sqrt{\frac{\tau_{wall}}{\rho}} \tag{22}$$

Where $v^* \approx$ is the shear velocity or the frictional velocity $\approx v_{rms}$. ρ is the density of fluid, τ_{wall} is wall shear stress.

One of the most challenging problems is to calculate shear stress which is a function of Reynolds number based on the distance along which the boundary layer developed. There is no previous theoretical study available to get this distance for the present flow domain. Therefore, it is very difficult to theoretically predict the shear velocity as well as turbulence intensity (I) for the current configuration. In case of a fully-developed duct flow, I can be estimated from the empirical formula [Fluent, 2003];

$$I = \frac{v_{rms}}{v_{av}} = 0.16(\mathrm{Re}_{HD})^{-1/8}$$

Where, Re_{HD} is the Reynolds number based on hydraulic diameter with I=4% for Re_{HD}=50000. However, the present flow is not similar to the duct flow. Hence, turbulence intensity was estimated using the experimental data of Singh [1993] for purely radial flow where it was varied from 12 to 20 percent. In the experiment [Singh, 1993], I was decreasing with increasing the Reynolds number and decreasing

the gap ratio inside the domain. During the present solution process, no effect was observed due to the inlet I variations.

b). Hydraulic diameter:

Hydraulic diameter was calculated from the following formula;

$$D_H = \frac{4A}{P} \tag{23}$$

For the flow between two discs;

D_H = hydraulic diameter,

Where H is gap height and D is disc diameter.

A = Cross sectional area $= 2\pi D$.

P = wetted perimeter of the flow domain (for two discs) = $\pi D + \pi D = 2\pi D$.

Putting these relations in the equation (23) the hydraulic diameter for present study is

$$D_H = 2H \tag{24}$$

c) Reynolds-stress specification:

Reynolds-stress was specified by estimating the Reynolds stress components at inlet. Calculation was based on some empirical formula assuming isotropic turbulence at the inlet;

$$\overline{v'_\alpha v'_\alpha} = \frac{2}{3}k \tag{25}$$

Here, k is the turbulent kinetic energy that can be estimated from turbulence intensity, I using the following formula [Fluent, 2003];

$$k = \frac{3}{2}(v_{av} I)^2 \tag{26}$$

And Reynolds-Stress components in the perpendicular direction were neglected at inlet as axial velocity input was zero. Hence;

$$\overline{v_i' v_j'} = 0 \tag{27}$$

vii) Solution control:

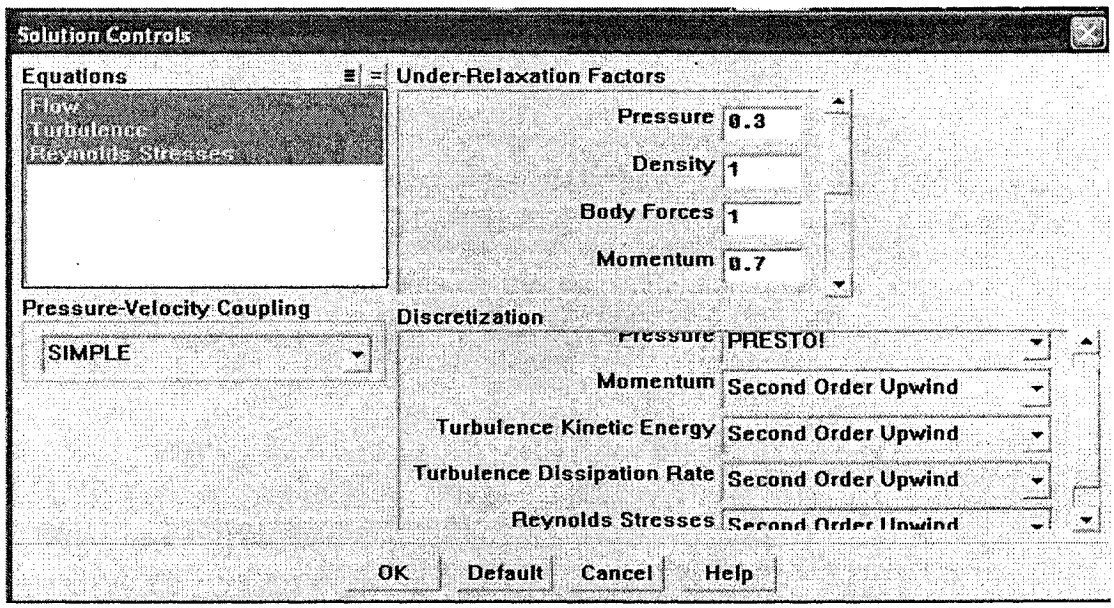

Figure 4.7: Example of settings in window showing solution control panel.

In the solution control panel (figure 4.7) of solver, all the equations like flow, turbulence, Reynolds-stresses and swirl velocity (for swirling case only) were kept running together to get the calculation in the same iteration. SIMPLE (Semi – implicit Method for Pressure –linked Equations) scheme was chosen as the method of pressure- velocity coupling. Because, this algorithm uses a relationship between velocity and pressure corrections which enforce the mass conservation through the solution and pressure field of the domain could be obtained. Due to the pressure interpolation of flow with high swirl ratio or the flow inside strongly curved domains, PRESTO! (Pressure Staggering Option) scheme is recommended [Fluent, 2003].

Second order upwind discretization for momentum equations, swirl velocity, turbulence kinetic energy, turbulence dissipation rate and Reynolds stresses was set to reduce numerical diffusions. Default settings of Under relaxation factors such as 0.3 for pressure, 0.7 for momentum, 1 for density,1 for body force, 0.9 for swirl velocity,0.8 for turbulent kinetic energy,0.8 for turbulent dissipation rate,1 for turbulent viscosity and 0.5 for Reynolds stresses were used to get convergence. At each iteration, solution proceeds according to following flow chart as segregated solver was employed.

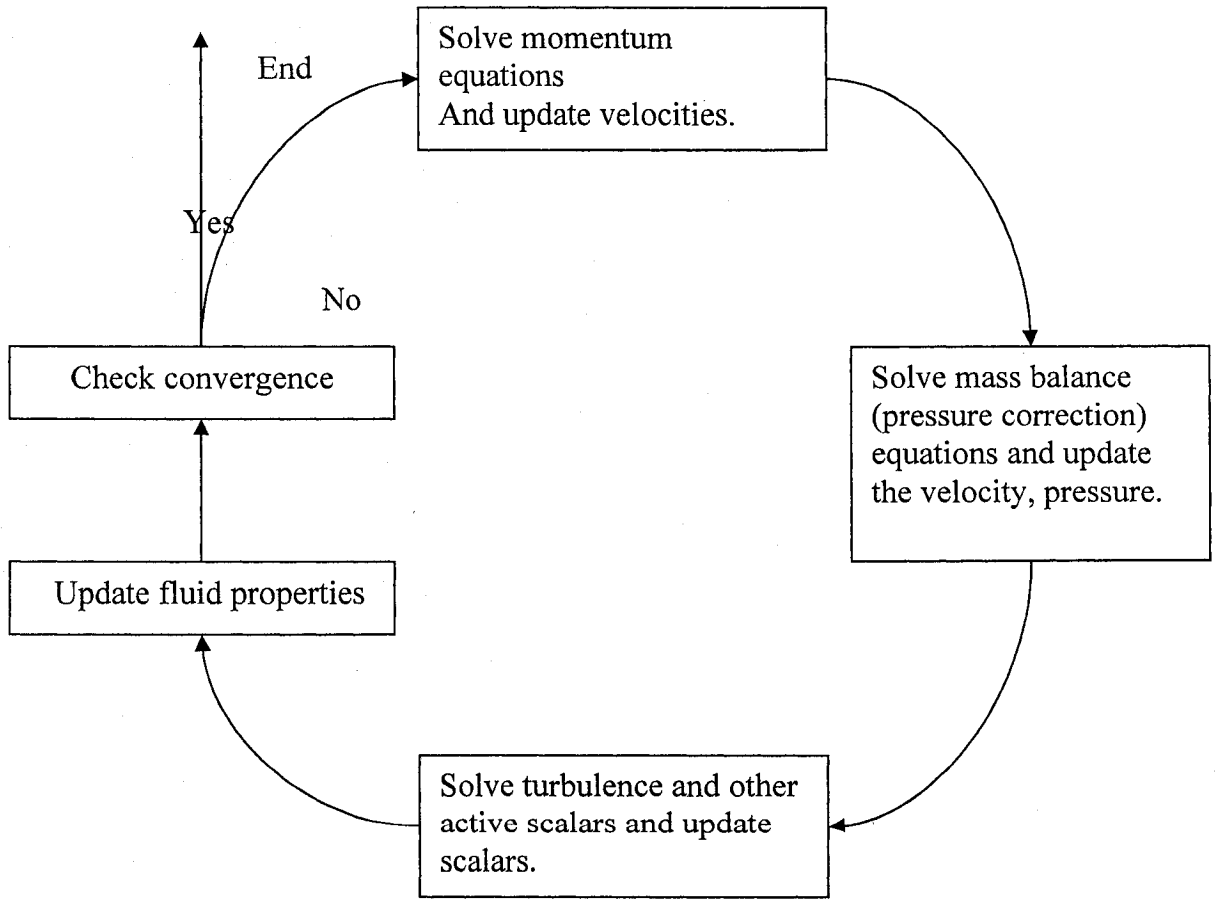

Figure 4.8: Flow chart of numerical calculation at one iteration for segregated solver.

4.2.3 Sample calculations of different parameters for boundary conditions:

i) Purely sink flow:

Calculations using Singh [1993] experimental setup;

Given flow rate Q= 19.71E-03 m3/s, disc radius R_o=152.4mm, disc diameter D=304.8 mm, Gap size H= 12mm, radius of sink outlet R_i= 25.4mm.

So the gap ratio $G = \frac{H}{D}$=12/304.8 = 0.03937.

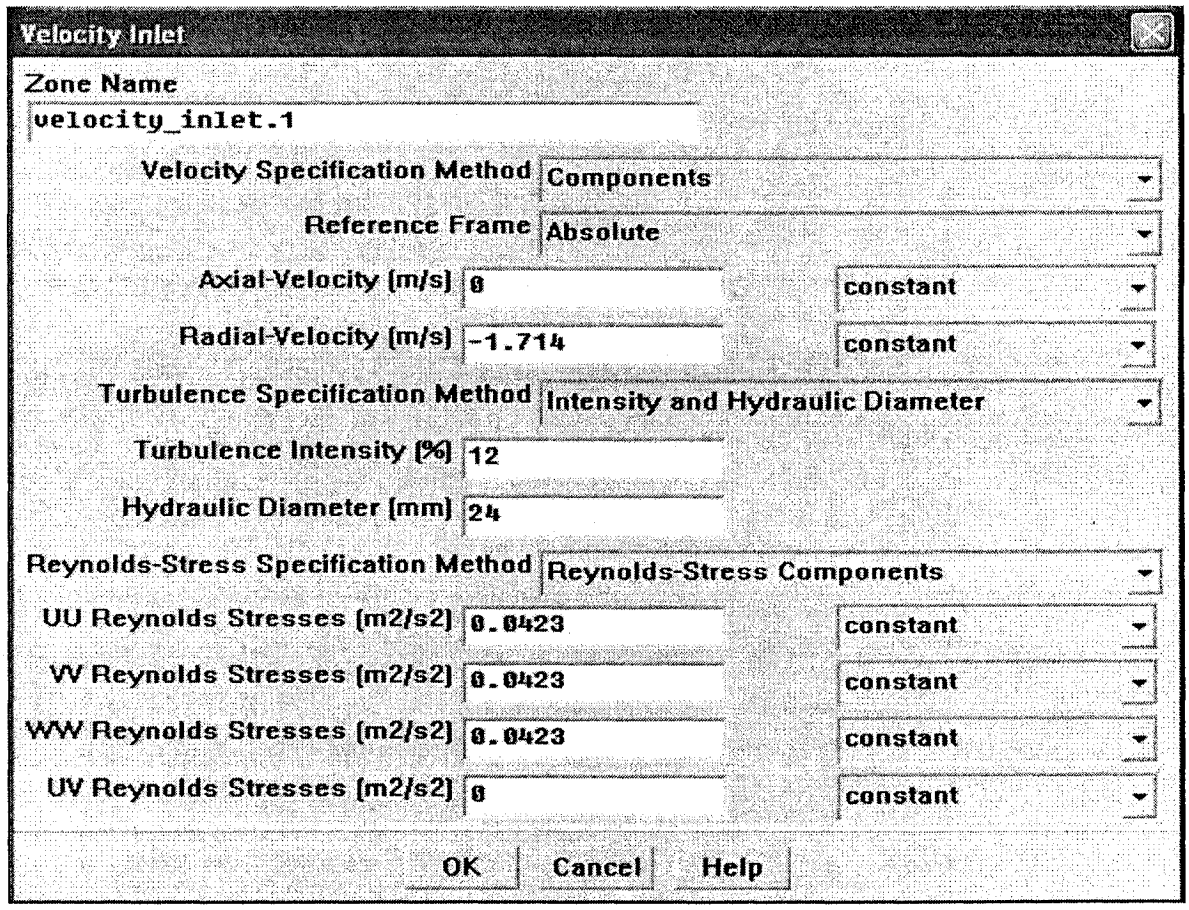

Figure 4.9: Sample input boundary window of Fluent for purely sink flow.

From the equation (19), Inlet radial velocity u_0 = 1.714 m/s with (-)ve direction.

Hydraulic diameter $D_H = 2H$ (equation, 24) = 24mm.

Inlet Reynolds number, $\mathrm{Re} = \frac{\rho u_0 D_H}{\mu} = 2816$

Where ρ = 1.225 kg/m3 and μ =1.7894e-05 kg/m-s.

Inlet turbulence intensity I = 12% (estimated from the experiments).

From equation (26), inlet turbulent kinetic energy k = 0.0635 m2/s2.

Finally, the Reynolds- stress components at inlet, $\overline{v'_\alpha v'_\alpha} = \frac{2}{3}k$ =0.0423.

And $\overline{v'_i v'_j} = 0$.

ii) Swirling inflow:

The experimental set-up of Savino and Keshock [1965] was employed for sample calculations.

Here, given mass flow rate $\dot{m}$ = 0.209 lbm/s, disc radius, R_o = 6.86 in = 174.244mm, outlet radius R_i = 1 in = 25.4 mm, Gap size H = 1.25 in = 31.75mm.

Density of air at inlet ρ =0.106 lbm/ft3 = 1.703236 kg/m3. μ =2.29e-05 kg/m-s.

Given inlet swirl ratio, S = 14.634.

So, aspect ratio, $G = \frac{H}{D}$ = 1.25/ (2*5.86) = 0.106655 ≅ 0.107.

Volume flow rate, $Q = \dot{m} / \rho$ =1.965653 ft3/s.

From the equation (19), radial velocity u_0 = 6.15 ft/s = 1.87452 m/s with (-) ve direction.

From the equation (20), tangential velocity, $v_0 = u_0 * S = 90$ ft/s = 27.432 m/s.

Hydraulic diameter $D_H = 2H$ (equation, 24) = 2.5 in = 63.5 mm.

Inlet Reynolds number, $\mathrm{Re} = \frac{\rho u_0 D_H}{\mu} = 8853$.

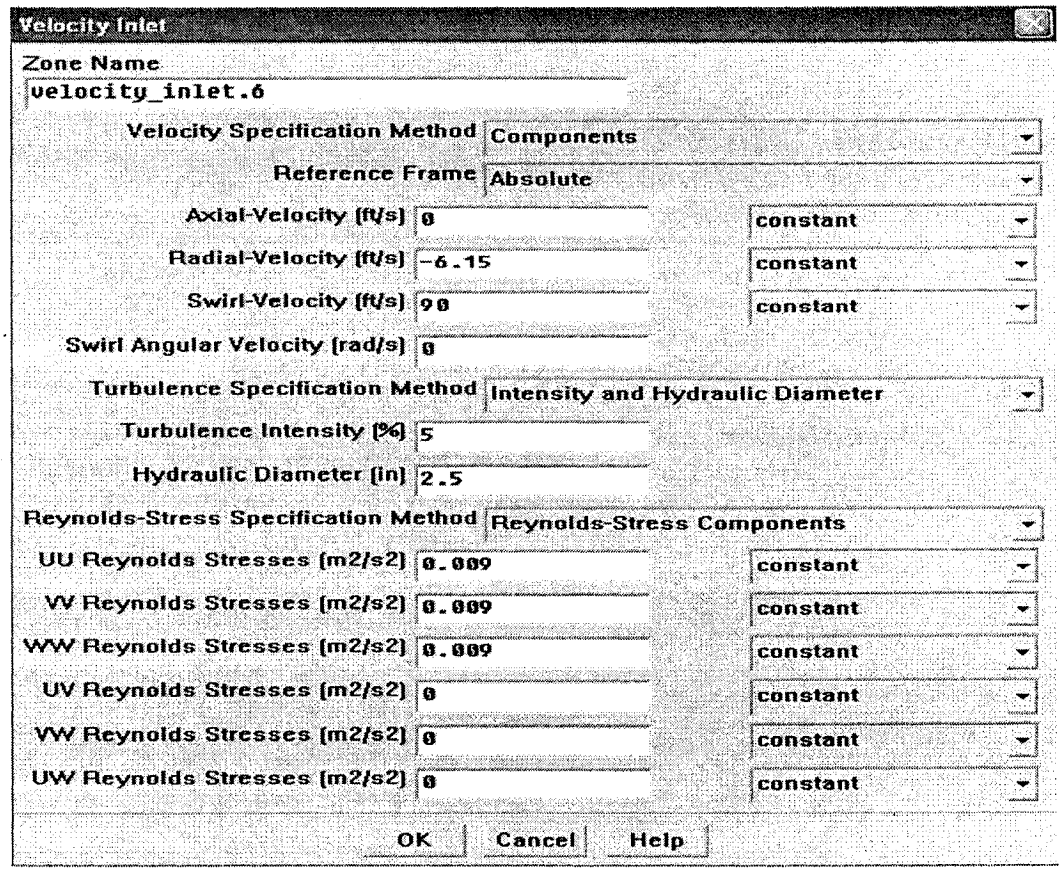

Figure 4.10: Sample input boundary window of Fluent for swirling inflow.

As Turbulence intensity I, increases with increasing Reynolds number at inlet, than we set I = 5 to 30 % but could not realize any change in solution for this variation.

From equation (26), inlet turbulent kinetic energy k = 0.0131768 m2/s2.

So, Reynolds- stress components at inlet, $\overline{v'_\alpha v'_\alpha} = \frac{2}{3}k = 0.009$, and $\overline{v'_i v'_j} = 0$.

4.2.4 Verification of incompressibility:

i) Purely Sink flow:

i) Incase of Q= 19.71E-03 m3/s, Gap = 0.03937 and inlet Reynolds No. = 2816, at the 28.194 mm radial location (0.185 non- dimensional radius from exit),

From the numerical solution;

Area-Weighted Average Radial Velocity = 9.3128608 m/s (in negative direction).

Now, speed of sound in air is 347.219 m/s (as speed of sound = $\sqrt{\gamma RT}$ where, specific heat constant of air γ = 1.4, Gas constant R of air 287.05 N.m./kg K, T= 300K).

So Mach number, Mc = Local average radial velocity / speed of sound = 0.026821.

As the flow does not exceed the Mc = 0.3 at above radial location (near exit) than its clear that flow remains incompressible at that location. Hence, incompressible assumption is valid for these boundary conditions.

b) Incase of Q= 34.42E-03 m3/s, Gap = 0.03937 and inlet Reynolds = 4918, at 28.194 mm radial location (0.185 non- dimensional radius),

Again, from the Numerical solution;

Area-Weighted Average Radial Velocity = 16.26417 m/s (in negative direction).

Again Speed of sound = 347.219 m/s.

So, Mc = 0.04684, which is far beyond Mc = 0.3 (compressible criteria).

Hence, the flow is still incompressible at these boundary conditions.

ii) Swirling inflow:

From the numerical solution, The Area-Weighted Average Radial Velocity at 1 in. radial location (from exit) is 17.699781 ft/s = 58.0701m/s (negative direction).

Speed of sound in air is 347.219 m/s.

So Mach number, Mc = 0.16724 which indicates the flow is incompressible at that location. Hence the assumption and solution of incompressible flow is valid for the swirling in-flow also.

4.2.5 Post-Processing:

Post –processing was employed for creating surfaces at different radius, reporting mass flow rate, plotting the radial and swirling velocity profiles, getting the radial pressure distribution as wall as streamlines to compare with experiments.

4.2.6 Convergence:

Convergence of solution was checked for different residuals which were obtained in graph as follows;

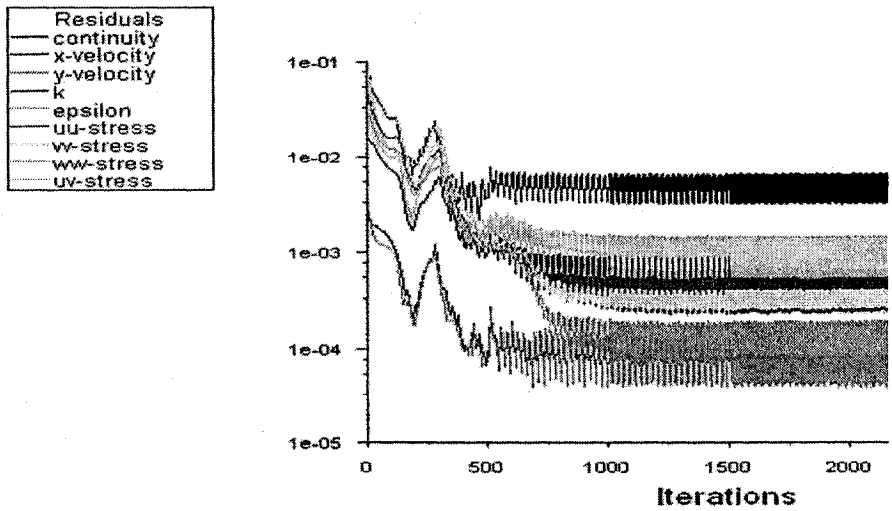

Figure 4.11: One example the residuals

CHAPTER 5

The Validation

Comparison of numerical results with the experiments will be provided in this chapter in two parts; purely radial sink flow and inflow with swirl. As per definition of inflow, the fluid enters the domain through the periphery and drained via by centrally located outlet. The characteristics of the radial pressure distribution, radial velocity at different stations obtained numerically (described in previous chapter) of a steady, incompressible, axi-symmetric, turbulent flow will be compared with previous experimental investigations. Data from Desantis and Rakwasky [1971], Singh [1993] were chosen for purely radial flow and that of Savino and Keshock [1965] for swirling case.

5.1 Purely sink flow:

In the case of a sink flow, the cross sectional area reduces in the streamwise direction and consequently the fluid accelerates. As no tangential velocity is introduced at inlet, the streamlines between inlet and exit regions will be parallel, see figure 5.1. Due to the developing flow near the inlet and at the exit corner turning produce streamline bending evident in the same figure. At the exit manifold the classical recirculation patch due to *vena contracta* is clearly visible.

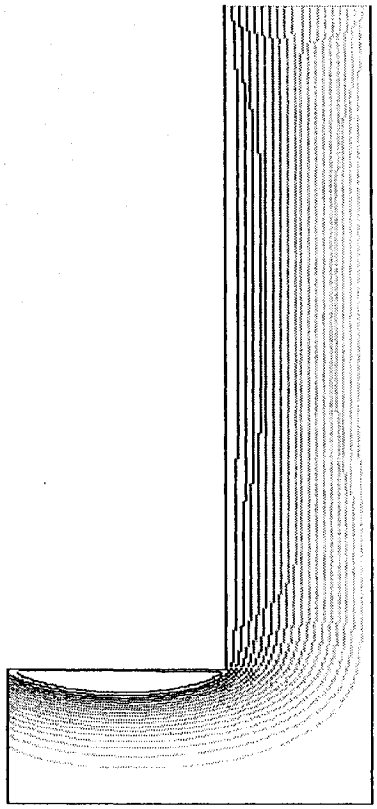

Figure 5.1: Stream function for the numerical modeling of purely radial turbulent sink flow at G=0.0394, Re= 2538.

Due to the existence of the exit recirculation zone, the manifold length of numerical domain should be selected in such a manner as to allow flow development. Any length before this development contains reverse flow. As outflow boundary condition let the flow go out only, it contradicts the algorithm followed by recirculation zone and hence, misleads the pressure calculations. Moreover, the pressure boundary condition will lead to numerical difficulties, which in turn will necessitate additional computing time for convergence. Due to the complexity in estimating the backpressure and turbulence intensity of the reverse flow, the outflow boundary condition was used in lieu of the exit pressure condition. For purely sink

flow studied here, a pressure condition at the inlet provided similar result as those by the inlet velocity condition. However, a uniform velocity at inlet was imposed due to the simplicity. Particular care was provided to the inlet length as turbulent characteristics require sufficient time and distance to adjust to the acceleration. Even if fully developed turbulent profile was defined at inlet, it would not affect the solution to a significant manner since in the case of purely sink flow, the nature of turbulence depend only on acceleration rather than the 'history of flow' at the entrance.

i) Pressure Distribution:

The radial variation of the static pressure depends on the inertial contribution, turbulence losses, and viscous dissipation.

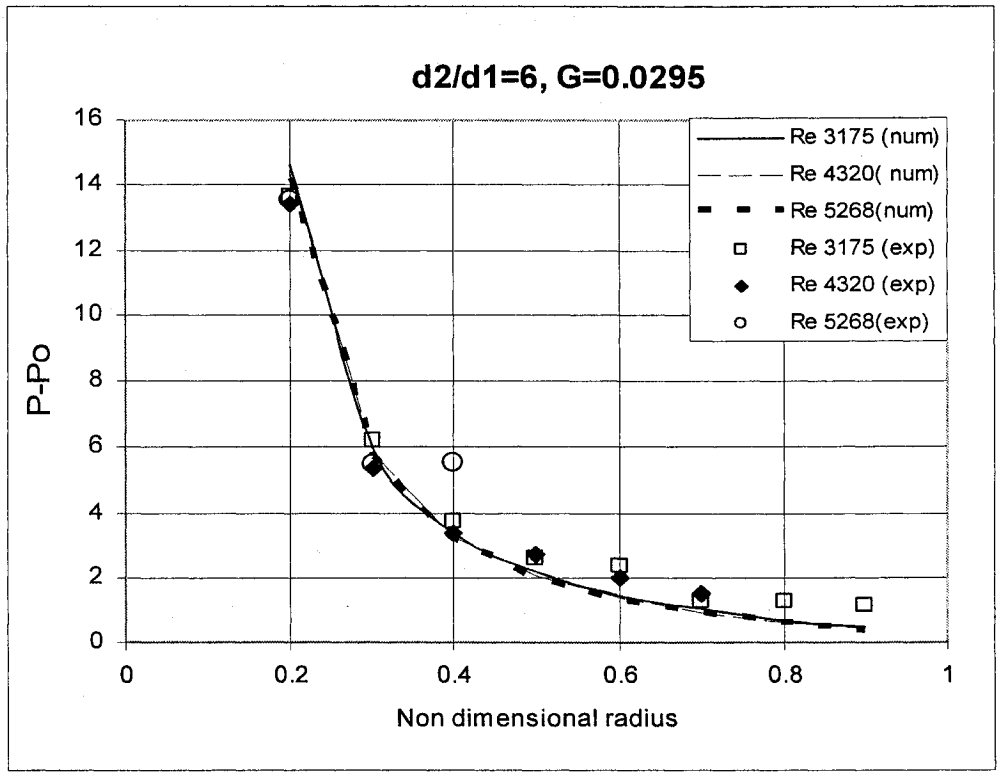

Figure5.2: Numerical and experimental [Singh, 1993] pressure difference of purely sink flow for G=0.0295.

In order to gage the numerically obtained pressure distribution against the experiments of Singh [1993] three different geometries (gap ratios G=0.0295, G= 0.0197, G= 0.00984) along with twelve inlet Reynolds numbers were used

Since for a purely sink flow the flow area is continually reduced along the flow direction, the pressure decreases monotonically [Tsifourdaris, 2003]. Figures 5.2, 5.3, and 5.4 show changes of the pressure, starting immediately after the entrance, which persist until the fluid finds the exit port.

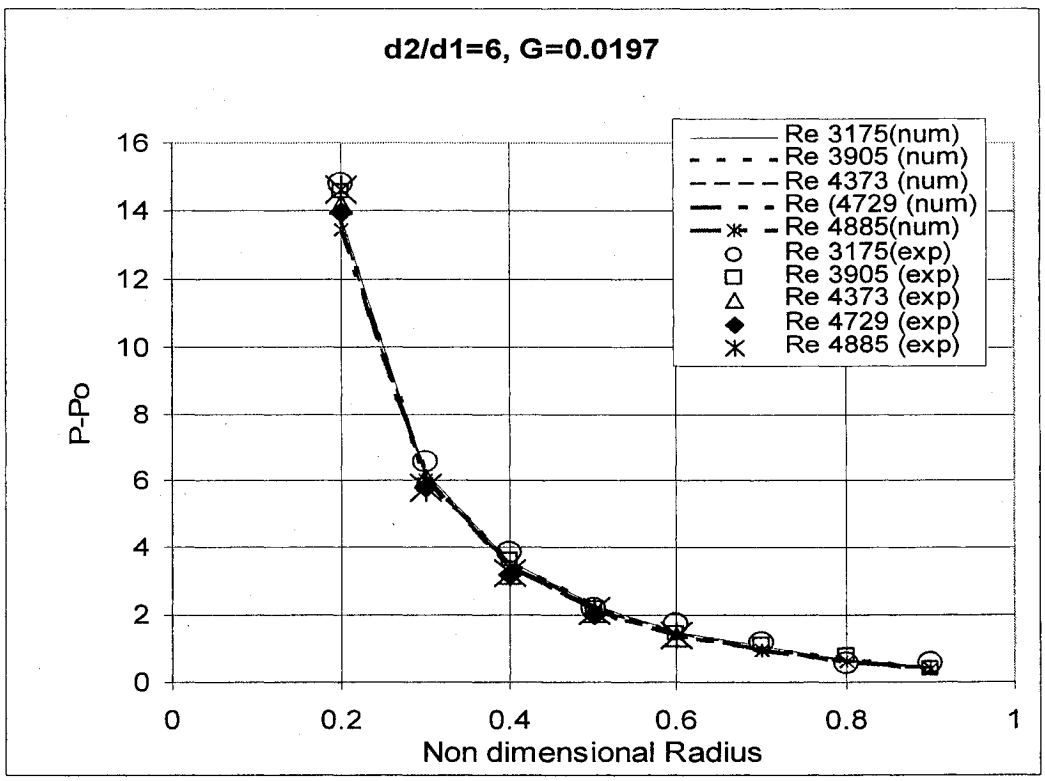

Figure 5.3: Numerical and experimental [Singh, 1993] pressure difference of purely sink flow for G=0.0197.

Figure 5.2 reveals some deviations to exist near the inlet area among the numerical solution and the experimental data. It is also evident, from the same figure, that there is a noticeable deviation between the two for radii greater than 0.6. In other figures (figure 5.3, figure 5.4), however, no such a digression is observed. The latter leads us to believe that the discrepancy among the two in figure 5.2 it may be due to experimental error.

Near the exit region, both of inertia and viscous contributions play vital roles for the noticeably sharp changes of the pressure. Decreasing the gap ratio has minimal effect on the pressure difference but for a given gap size, increasing the inlet Reynolds number leads to a decrease of the pressure drop.

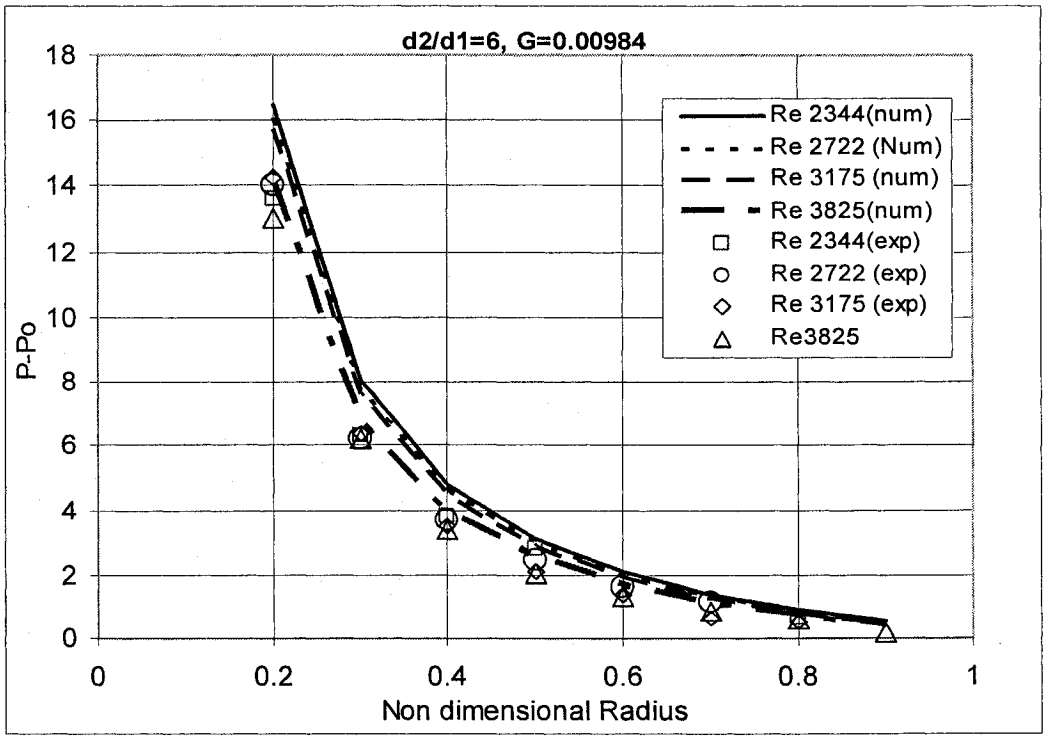

Figure 5.4: Numerical and experimental [Singh, 1993] pressure difference of purely sink flow for G=0.00984.

The percentage error amongst the numerical and experimental [Singh, 1993] pressure distributions is shown in Table 5.1. It is amply evident that the numerical technique is capable of predicting the pressure fairly.

			non dimensional radius							
Gap ratios	Re		0.2	0.3	0.4	0.5	0.6	0.7	0.8	0.9
G=0.0295	3175	% of error	-0.0693	0.0433	0.09511	0.18067	0.3912	0.2	0.446501	0.58897
	4320			-0.082	0.02567	0.23561	0.3228	0.385		
	5268		-0.0496	-0.0448	0.41959					
G=0.0197	3175		0.0642	0.0513	0.06843	-0.0341	0.109	0.105	-0.2632	0.204
	3905		0.0612	-0.0524	0.04122	-0.0075	-0.002	0.098	0.143	-0.114
	4373		0.0501	0.0091	-0.0735	-0.0447	-0.054			
	4729		0.0354	-0.0407	-0.0829	-0.0826		0.08	-0.19481	-0.523
	4885		0.0815	-0.0331	-0.0446	-0.0016	-0.023			
G=0.00984	2344		-0.2069	-0.2762	-0.252	-0.1056			-0.4676	
	2722		-0.1463	-0.2565	-0.2568	-0.1983	-0.206	-0.156		
	3175		-0.1033	-0.1905	-0.2715	-0.3772	-0.352	-0.93	-0.50933	
	3825		-0.0835	-0.0881	-0.1697	-0.2601	-0.273	-0.299	-0.293	-1.26

Table 5.1: Percent of errors between numerical and experimental [Singh, 1993] pressure difference.

ii) The Radial Velocity:

Based on the viscous and/or acceleration effects and in order to achieve solutions previous numerical and analytical studies for unidirectional sink flow [Wormley, 1969 and Tsifourdaris, 2003] were restricted to three different flow regions with setups of very small gap ratios and/or low inlet Reynolds numbers. However, the present study relaxes the previous restrictive conditions and considers the turbulent flow in enclosures of moderate gap ratios. The results obtained (see figure 5.5 to 5.11) show that inertia force is dominant to viscous force across almost the entire flow domain. In order to verify the numerically obtained flow characteristics, Singh's [1993] four experimental cases (shown in figures 5.5, 5.6, 5.7, and 5) were considered. Two gap ratios and a range of inlet Reynolds numbers were used. In addition, the three sets of experimental data provided by Desantis and Rakwasky's [1971] (see figures 5.9, 5.10, and 5.11) were also included.

When the flow enters the domain with a uniform velocity and in order to accommodate the wall non-slip condition, it starts to develop. Figures 5.5 and 5.7 are implying that the numerical calculation is able to capture the flow evolution in the entrance region. For higher Reynolds numbers (figures 5.6 and 5.8), the small differences between the experiment and numerical solution at entrance region are clear. These discrepancies may be attributed to the insufficient time and space allocations (due to the higher inlet velocity) given for turbulence to be adequately adjusted to the acceleration. However, the trend of velocity profiles in both the numerical predictions and the experimental information seem to be reasonably good.

The numerical study of Murphy et al. [1983] suggested that at larger entry radii, after the entrance effects have died down, viscosity dominates the flow. The argument was based on the fact that in this region, the radial velocity profile changes from the imposed inlet uniform distribution to the parabolic shape. In the intermediate section, boundary layer develops and reaches up to half of the disc spacing. Then, cross-sectional area reduction causes the fluid in the potential core to accelerate and makes the boundary layer thinning until it reaches to the locality of exit. At very small radii, acceleration is seen to dominate the flow rather than viscosity that allows the radial velocity begins to revert back to a uniform profile.

The radial velocity inside the boundary layer has been measured by Desantis and Rakwasky [1971]. They provided three experimental data sets, corresponding to three different inlet-Reynolds numbers, show similar trends. The main flow between the two discs is essentially inviscid with a boundary layer developing along the two disk walls. These layers occupy only 10 percent of the total flow area. The radial velocity inside boundary layer was found to be a function of radius, while the boundary layer had developed at about 0.8 of the non-dimensional radial position. Subsequent to this radial position, its thickness decreases as the fluid continues to flow towards the center of the sink. The latter being a direct result of the favorable pressure gradient which tends to accelerate the flow in the stream wise direction.

Tsifourdaris [2003] had theoretically shown that boundary layer development near the entrance to be very quick and the displacement thickness found to increase

up to 80% of the non dimensional radius (see figures 5.5, 5.6, 5.7, 5.8), and then to decrease linearly towards the geometric center.

Finally, comparison between the current numerical and the experimental results of Desantis and Rakwasky [1971] presented in figures 5.10 and 5.11 show a very sound agreement even near inlet zone.

As the flow advances downstream (for example, less than 80% of the non-dimensional radius toward the centre of the sink) viscous effect is reduced rapidly and the radial velocity is increasing monotonically as the flow area reduces. In this region, acceleration affects strongly the nature of the flow, which produces the distinctly present velocity plateau.

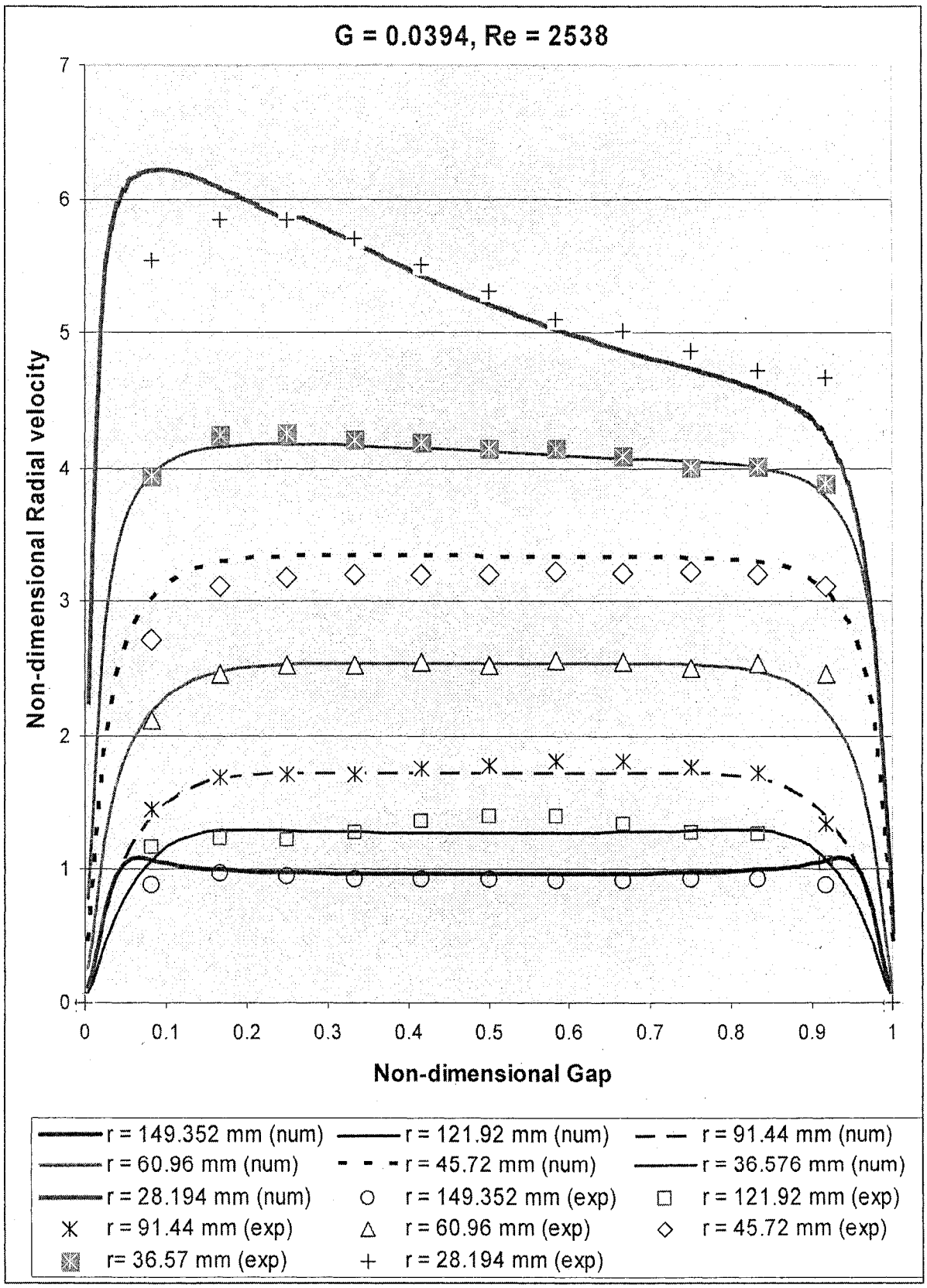

Figure 5.5: Radial velocity Vs. Gap size from numerical results and experimental data of Singh [1993] for G=0.0394, Re= 2538.

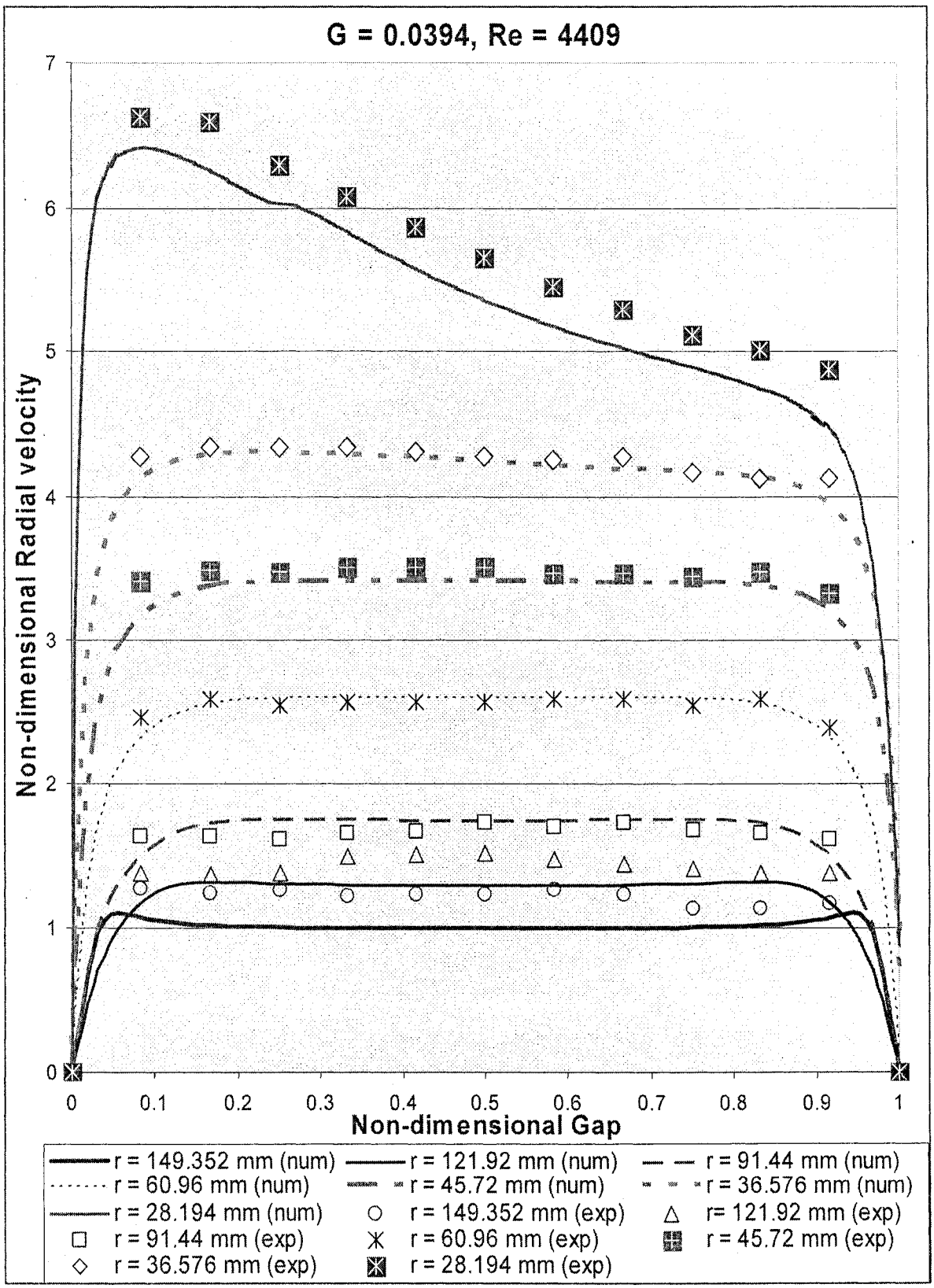

Figure 5.6: Radial velocity Vs. Gap size from numerical results and experimental data of Singh [1993] for G=0.0394, Re= 4409.

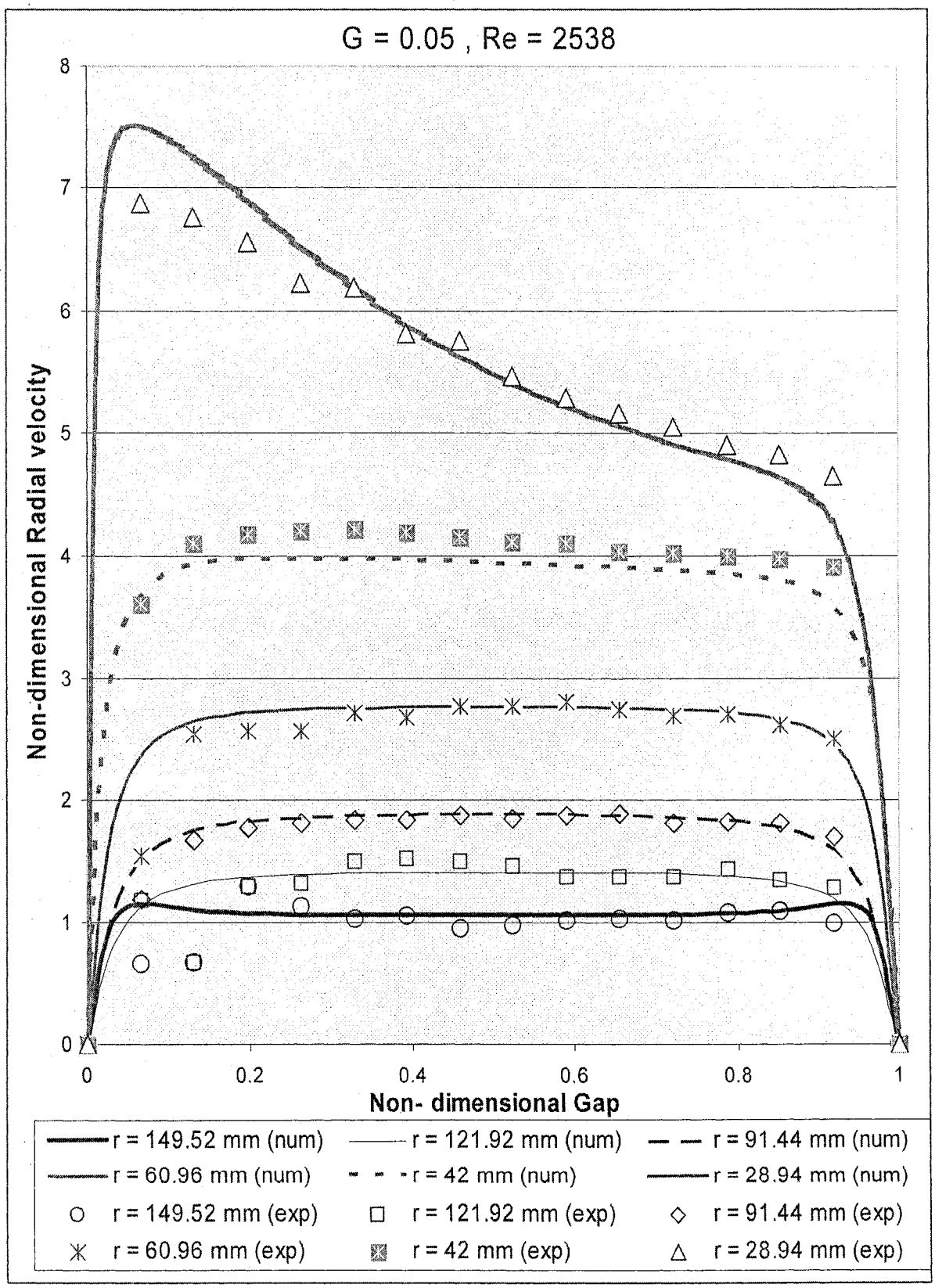

Figure 5.7: Radial velocity Vs. Gap size from numerical results and experimental data of Singh [1993] for G=0.05, Re= 2538.

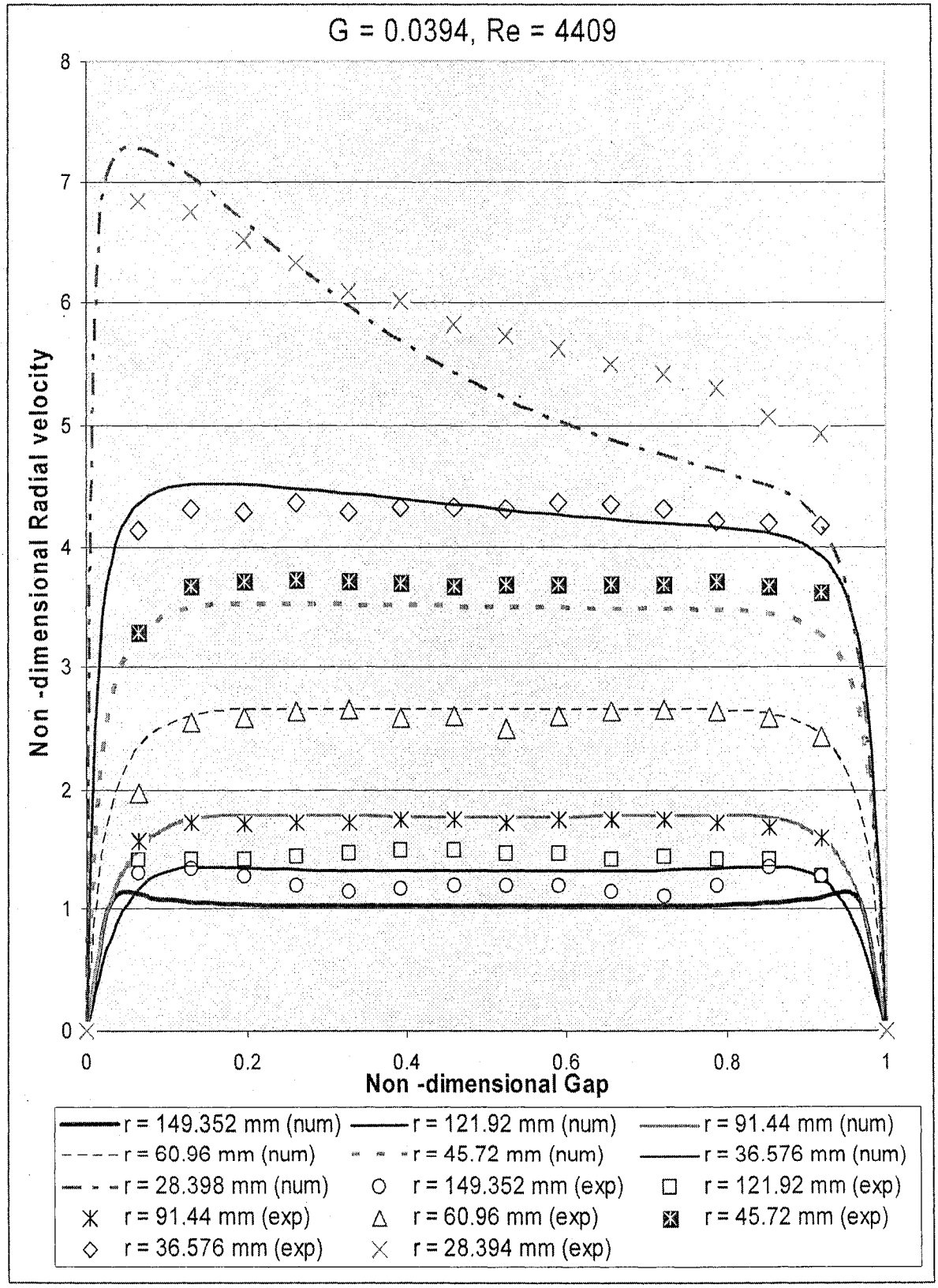

Figure 5.8: Radial velocity Vs. Gap size from numerical results and experimental data of Singh [1993] for G=0.05, Re= 4409.

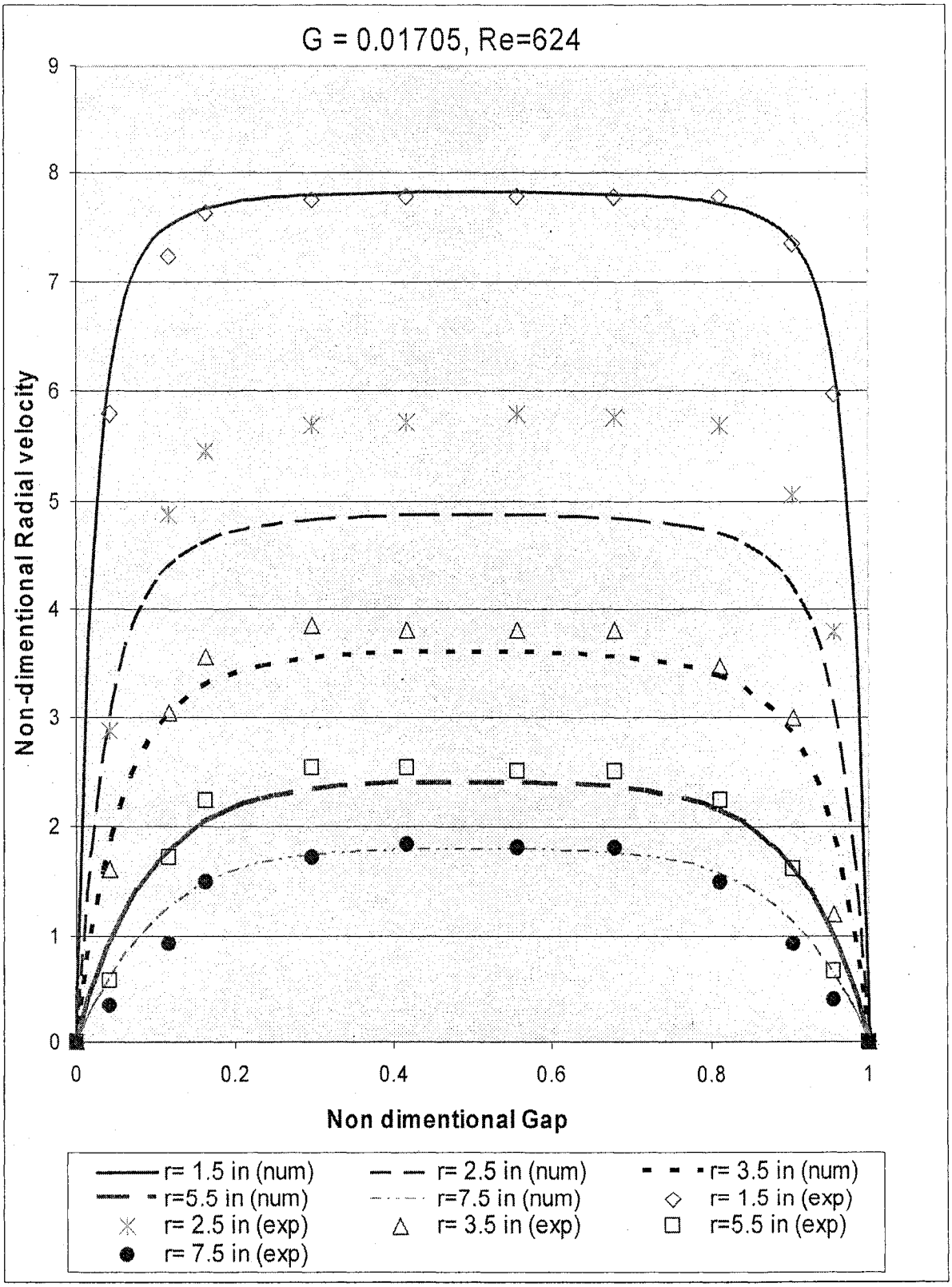

Figure 5.9: Radial velocity Vs. Gap size from numerical results and experimental data of Desantis and Rakwasky, [1971] for 38 CFM flow rate.

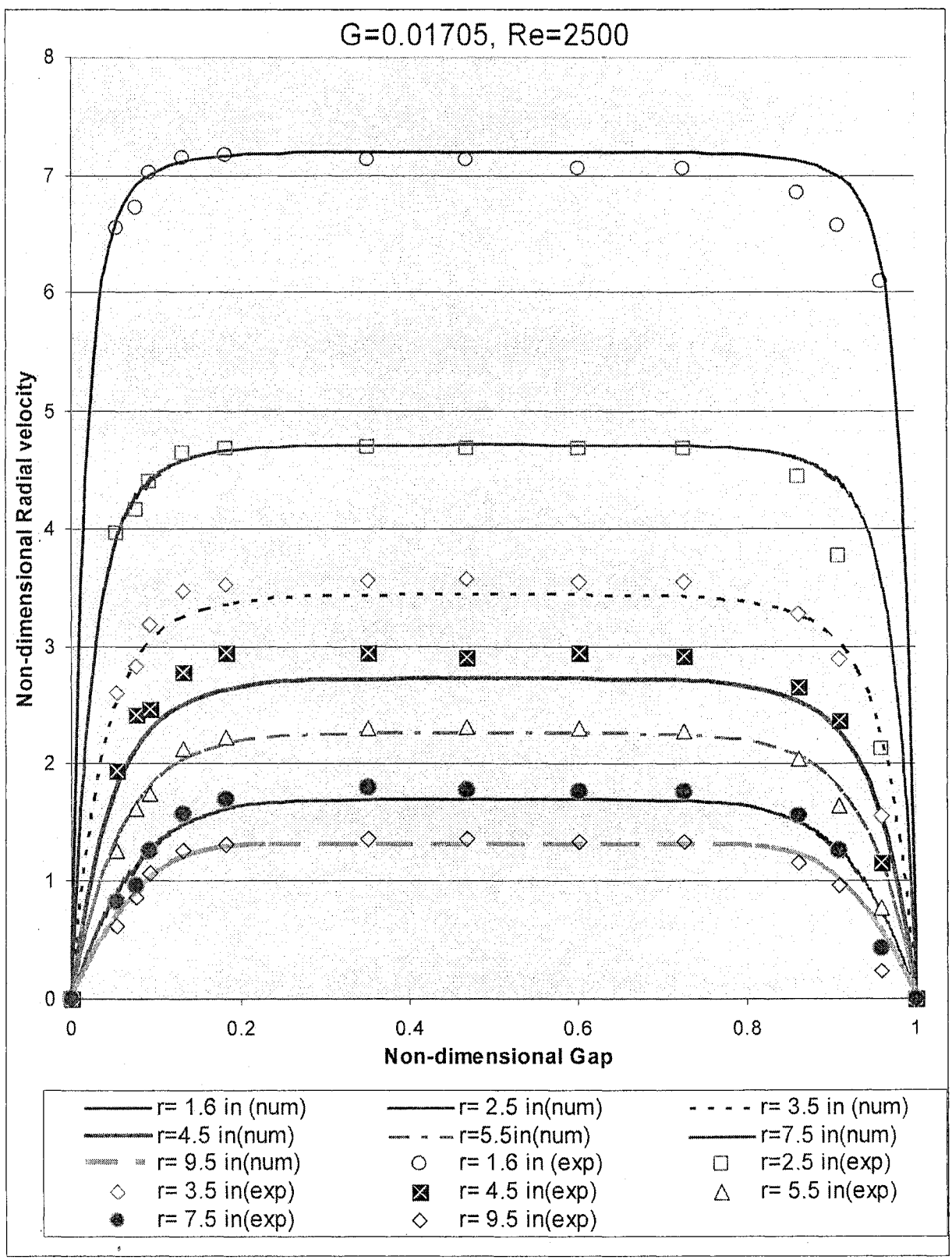

Figure 5.10: Radial velocity Vs. Gap size from numerical results and experimental data of Desantis and Rakwasky, [1971] for 88 CFM flow rate.

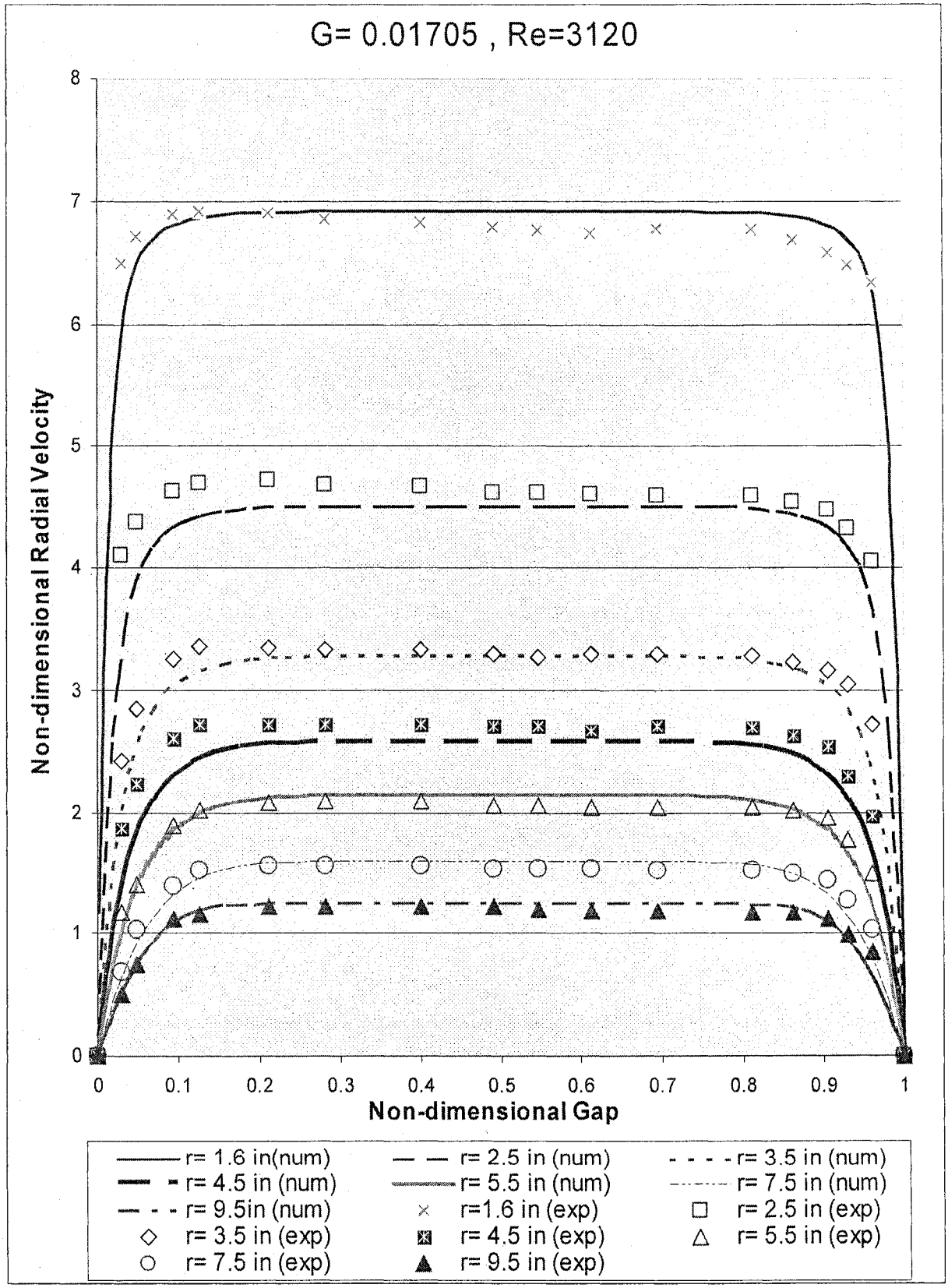

Figure 5.11: Radial velocity Vs. Gap size from numerical results and experimental data of Desantis and Rakwasky, [1971] for 176 CFM flow rate.

The flow seems to behave as an external boundary layer with a large central core flunked on both sides. These characteristics can easily be verified by examining figures 5.5 to 5.11 where they show Singh's [1993] Laser Doppler Anemometer (LDA) data against the present numerical computations.

Reasonable agreement in velocity profiles from radial location 91.44 mm (or 0.6 non-dimensional radius) to 45.72 mm (or 0.3 non-dimensional radius) is evident. However, for the increased Reynolds number with a same gap ratio (see figure 5.6), the numerical results collapse with the experimental data validating the appropriateness of all the assumptions and boundary conditions as well as the Reynolds-stress turbulent model employed to achieve the numerical calculations.

Although the gap size was increased from 12 mm to 15.24 mm [Singh,1993] with the same inlet Reynolds number (see figures 5.5and 5.7), but the radial velocity profiles have similar tendency within the intermediate flow region. Here again the numerical results was found to be more accurate at higher Reynolds number (see Figures 5.7 and 5.8). These characteristics imply that if the flow rate (hence the Reynolds number) is increased, the acceleration is also increased providing the flow lesser time and space (as area is reducing toward to the flow) to be affected by turbulence. This tendency can also be found in the previous numerical study of Murphy et al. [1983] where the flow visualization showed that the flow remained laminar up to local Reynolds number 20700 although it supposed to be turbulent at this extreme Reynolds number.

The numerical simulation based on Desantis and Rakwasky [1971] experimental arrangement has shown sensible agreement between two (figure 5.9, 5.10, 5.11). Here also the velocity profiles become flat as the flow proceeds (starting from 0.8 non-dimensional radius) towards the centre. At lowest flow rate (38 cfm), the results presented in figure 5.8, show a deviation between experimental and numerical data at the radial location of 2.5 inches which is eliminated at higher flow rates (see figures 5.10 and 5.11). Average radial velocity, calculated from the experimental data of Desantis and Rakwasky [1971] for this location (2.5 in), does not satisfy the law of mass conservation. This discrepancy may occur either due to plotting error or an error in the experimental set-up. Velocities at different sections were measured using hot-wire anemometry techniques. In general, the probe disturbs the flow and at the lower flow rate, this interference is more profound than the case of higher flow rate. In Singh's [1993] experiments this is not true as laser was used to measure the velocity. However, for different flow rates with the same gap ratio (G = 0.01705 here) the good agreement with experiments of Desantis and Rakwasky [1971] at the intermediate flow region (figure 5.9, 5.10, 5.11) confirms the adequacy of the numerical method to approximate the radial velocity.

Past this zone, the flow starts to sense the exit. In order to negotiate the turn, the streamlines begin to curve. Numerical modeling is also able to predict the asymmetric behavior of the velocity (see figures 5.5 to 5.8) where it displays maxima towards the disc encompassing the exit port. The latter behavior was also found in the

experiment conducted by Tsifourdaris [2003] at very low inlet Reynolds number and gap ratio (Re = 328.74, G= 0.01389).

Comparing the present results to the experiments of Singh [1993] for exit zone shows a good agreement for lower Reynolds number (figure 5.5 and 5.7) but a discrepancy appears if the flow rate is approximately doubled (see figures 5.6 and 5.8). These differences of numerical result from the actual flow situation could be due to two reasons. Firstly, the computations provide only an approximate solution. Secondly, the effect of compressibility plays an important role in the determination of the flow character which the present approach does not include. A qualm concerning the precise conditions in Desantis and Rakwasky [1971] experimental work may arise noting the asymmetric velocity profile near the exit area (see figures 5.10 and 5.11) where the flow paradoxically tends to go faster in one end than in the symmetric counterpart.

Another important fact of the numerical solution is its ability to predict the flow criteria near wall. All of the figures shown above (figures 5.5 to 5.11) are reporting a good correspondence between the numerical and the experimental results for the near the wall behavior although the present study focused on the mean flow rather than the flow through the boundary layers where no experimental data are available.

5.2 Swirling inflow:

Let us now consider the previously treated inflow with one modification. In addition to the pure radial velocity imposed at the inlet, let us now include also a tangential component. These types of sink flow have been found to be characterized by streamline curving; see the fine work of Savino and Keshock [1965]. A striking characteristic of flows of this kind is the appearance of a toroidal recirculation zone of fluid, which covers a hefty part of main flow area, see figure 5.12.

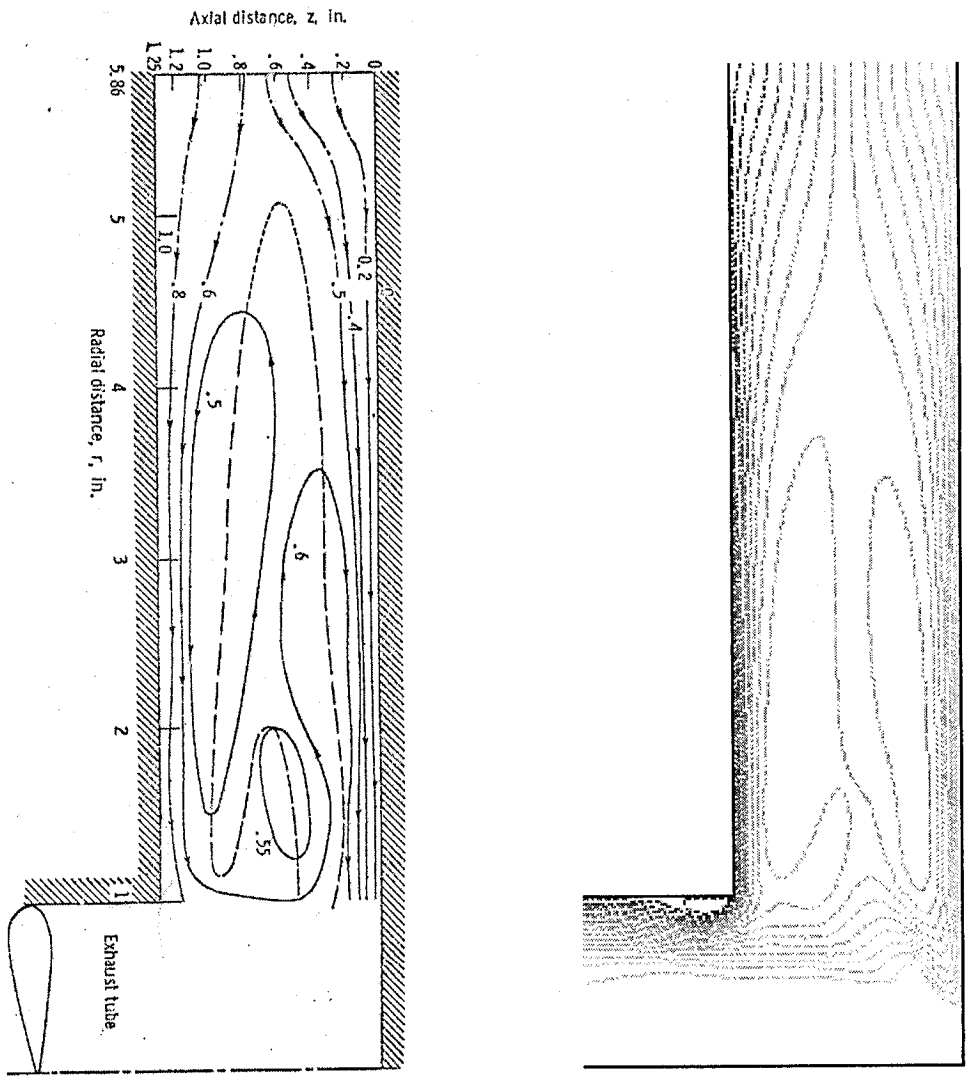

Figure 5.12 (a): streamlines of the experiment [Savino and Keshock, 1965]. Figure 5.12 (b): numerical streamlines.

The simulations with swirl considered the experimental set-up and flow conditions of Savino and Keshock [1965]. Their arrangement can be viewed into two ways; either swirling flow between two disks with a large gap, or the flow in a short cyclone chamber. Figure 5.12 (a) and (b) represents the streamline patterns obtained numerically and the previous experimental streamline patterns [Savino and Keshock, 1965] respectively. A good similarity between the two is clearly evident. As the fluid enters the flow domain it immediately senses the centrifugal force field. In the attempt to find the exit taking a path of least resistance, it splits into two streams. The first stream flows along the upper plate while the second one propagates next to the lower disk. Streamline contraction in the proximity of walls points out that most of the inlet flow finds the exit flowing through the top and bottom Ekman's boundary layers.

In core region where the toroidal vortices reside, are seen to extend up to the inlet and to even to penetrate deep near exit, streamlines indicate that almost no fluid particles fine the exit through a rude crossing the mid channel. Savino and Keshock [1965] performed their experimental investigation under one swirl ratio. However, the effect of different inlet swirling ratios on streamline development will be discussed later. Here, the numerical results in terms of the non-dimensional pressure, radial velocity along with swirling velocity profiles will be compared with the experimental of Savino and Keshock [1965].

i) The Pressure:

The static pressure for swirling inflow shows a similar behavior as for the purely sink flow. Following the acceleration, which has less effect in the inlet region, pressure drop increases slower than in the case of a uni-radial flow but as it penetrates more into the flow domain the strong acceleration makes the pressure to experience a considerable drop near the outlet region.

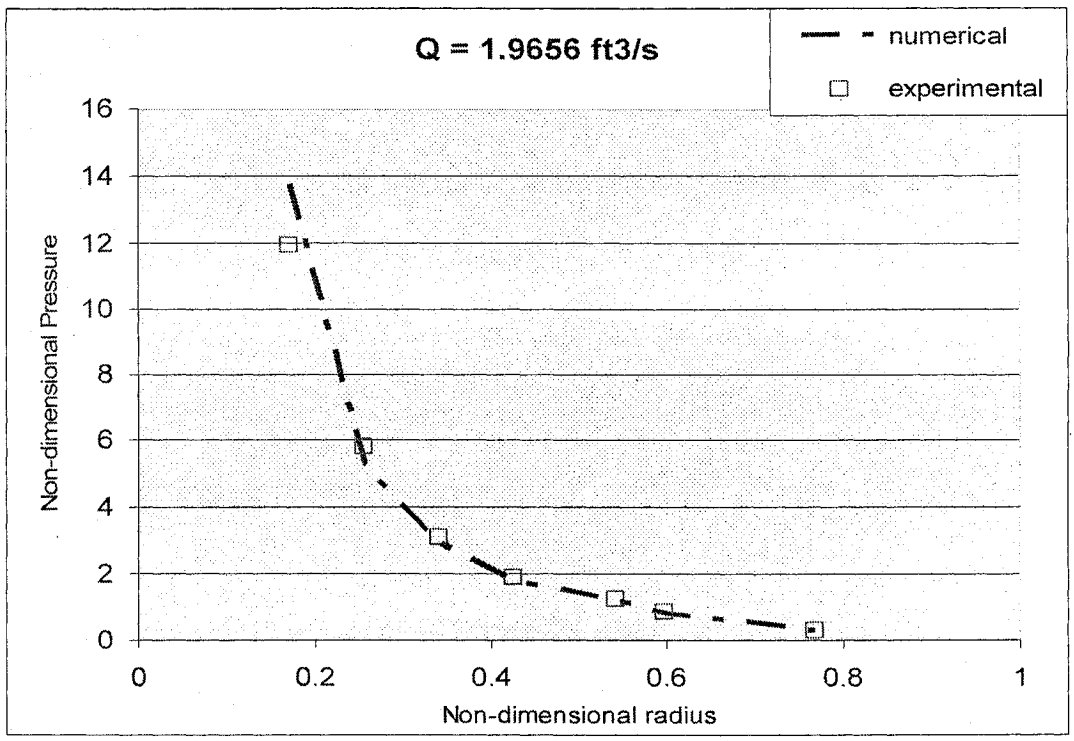

Figure 5.13: comparison of numerical pressure profile with the experiment [Savino and Keshock, 1965]

Figure 5.13 shows the numerical pressure values to be in good accord with the experimental data of Savino and Keshock [1965]. Alike to the purely radial inflow there is a noticeable small deviation between the two in the vicinity of the exit where compressibility may be important. A similar behavior for the pressure field was also

reported by Tsifourdaris [2003] where it was shown that for the highest gap size tested, the pressure drop was more pronouns at Reynolds numbers. Meanwhile, the effect of Reynolds number and gap ratio is minimal on the pressure field for smaller gap sizes. The more severe reduction of pressure for swirling flow in comparison to purely sink flow was reported in Tsifourdaris [2003] which is also in concurrence with present numerical calculations.

ii) The Radial Velocity

The numerically calculated radial velocities at different radial stations and the experimental profiles from reference [Savino and Keshock, 1965] are presented in figures 5.14 (a) to (g).

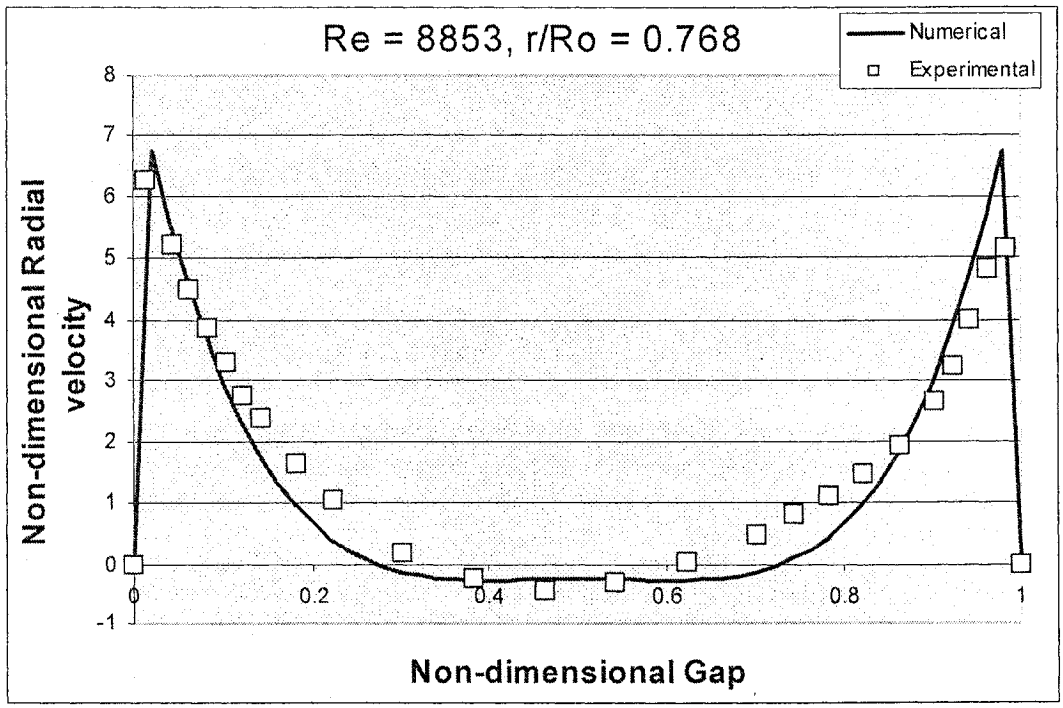

Figure 5.14(a): Radial velocity Vs Gap size from numerical result and experimental data of Savino and Keshock [1965] at 0.768 non-dimensional radial distance.

Its clear form all these figures that almost all radial inflow occurs adjacent to the discs surfaces.

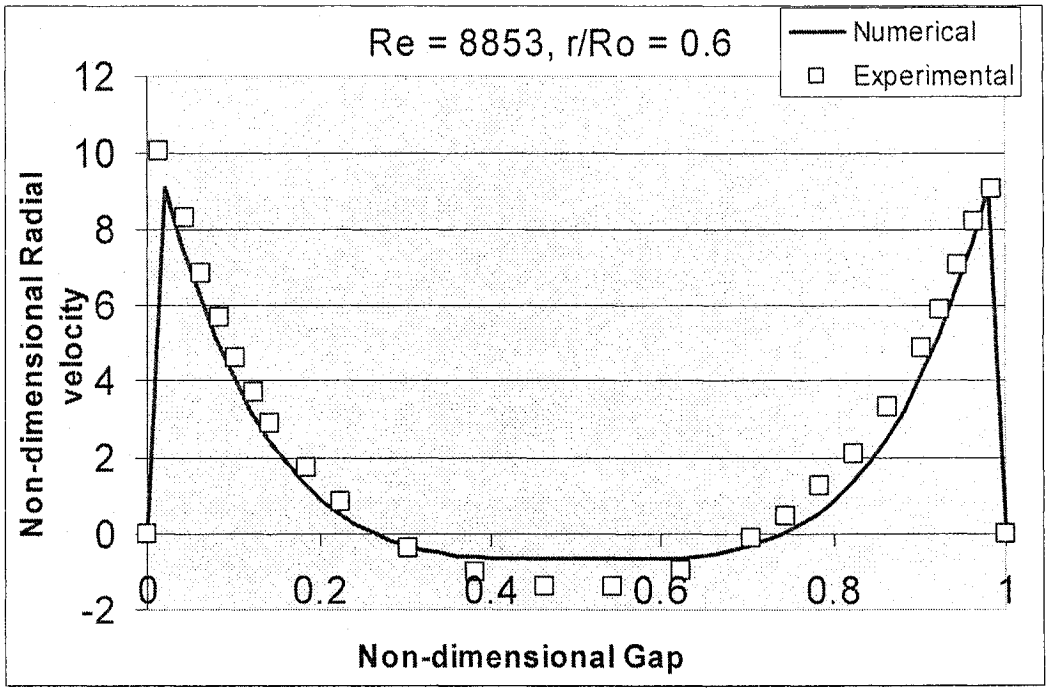

Figure 5.14(b): Radial velocity Vs Gap size from numerical result and experimental data of Savino and Keshock [1965] at 0.6 non-dimensional radial distance.

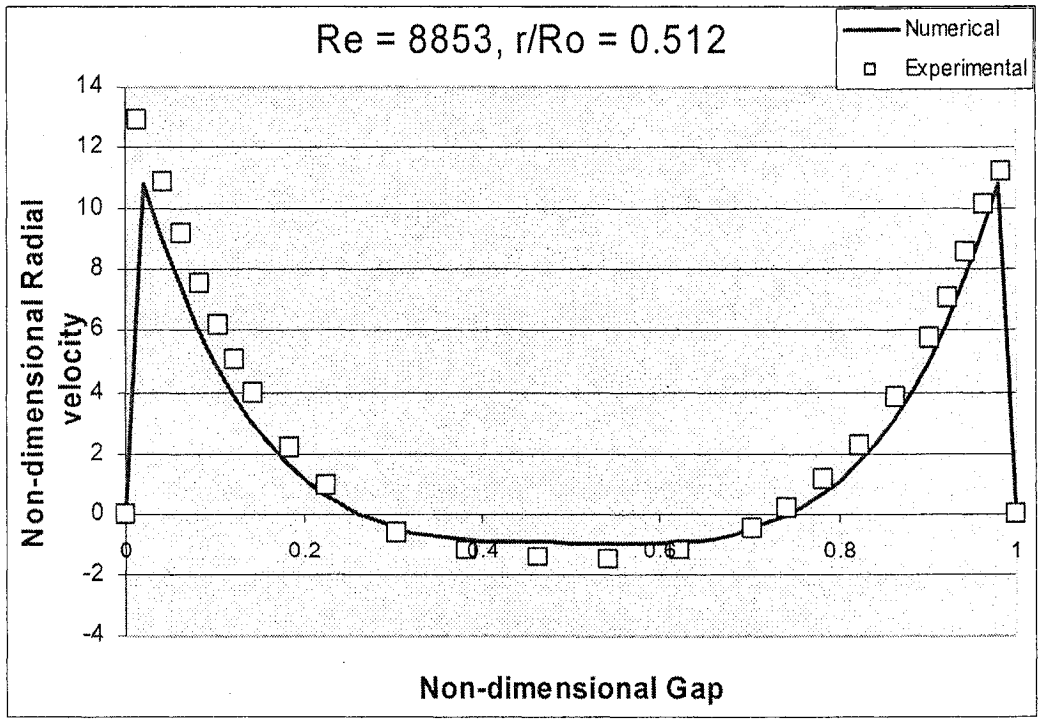

Figure 5.14(c): Radial velocity Vs Gap size from numerical result and experimental data of Savino and Keshock [1965] at 0.512 non-dimensional radial distance.

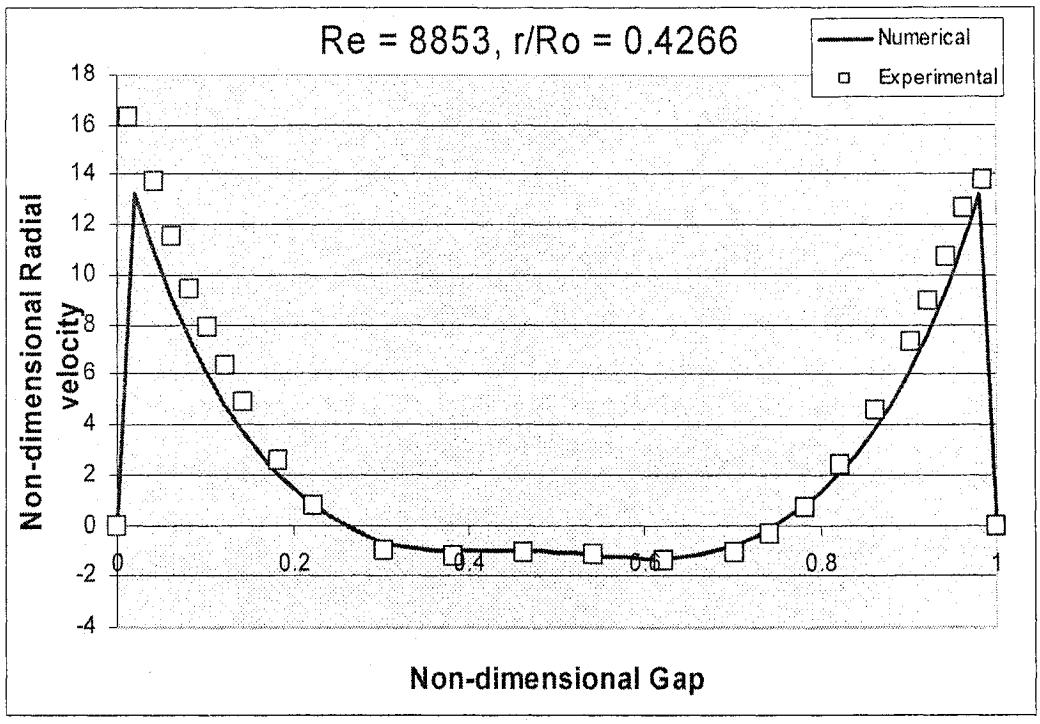

Figure 5.14(d): Radial velocity Vs Gap size from numerical result and experimental data of Savino and Keshock [1965] at 0.4266 non-dimensional radial distance.

The swirling ratio, which dominates this type of fluid motion, will be discussed next. Imposition of swirl at the inlet gives rise to a centrifugal force field. In addition to the acceleration, this type of flow must develop a static pressure component in such a way as to mainly balance the radial centrifugal force. This will give rise to differences in the present calculations as compared to the previous where swirl was absent. Increasing the inlet swirl ratio produces a greater centrifugal field which affects considerably the flow.

In an analytical and experimental study by Wormley [1969] using a short vortex valve, the preference of the radial inflow to find the exit through the boundary layers was looked at by means of flow visualizations. Photographs with injected

milky powder has shown that the higher the swirl number is the smaller the portion of the fluid that finds the exit through a mid-channel path, or the higher the fraction that finds the outlet through the upper and lower boundary layers. The long lasting milky donut (see flow visualization photographs, fig 3, 4, 5, 6 of Wormley, 1969) have shown the lack of radial flow in the mid- chamber at highest swirl ratio. When swirling ratio was decreasing, more radial component was penetrating the mid-gap causing those milky donuts to occupy less portion of the chamber. At the lowest swirl ratio, there was no donut remaining in the domain which demonstrated the minimal effect of a weak centrifugal force on the flow.

The influence of variable swirling ratio was also examined by Donaldson and Snedeker which was reported by Savino and Keshock [1965].

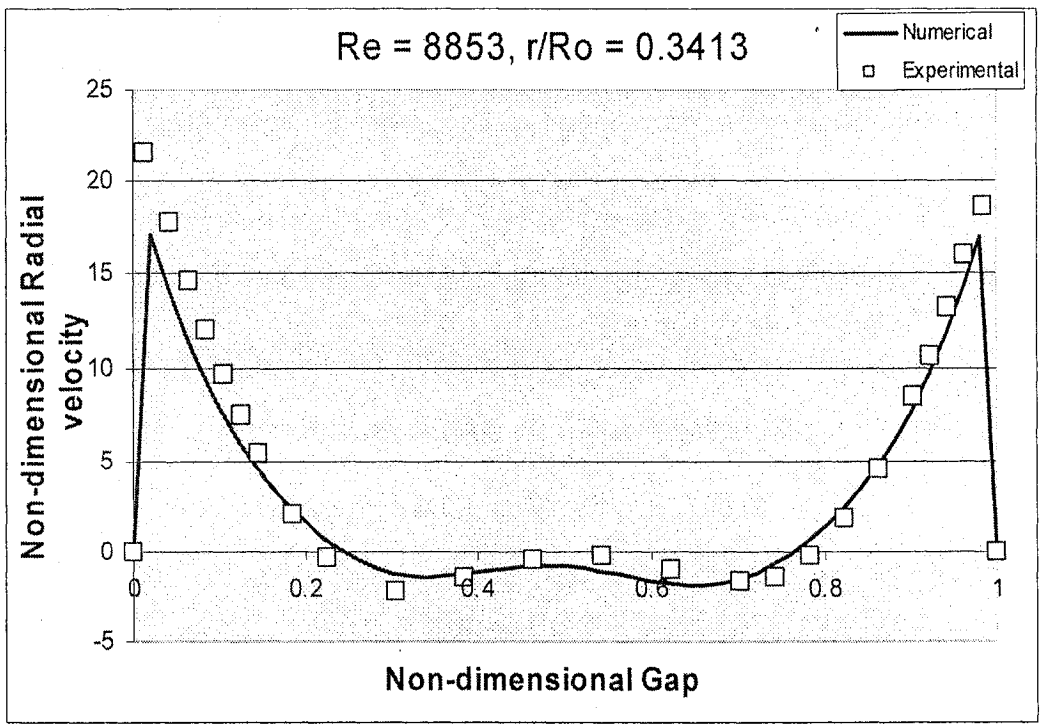

Figure 5.14(e): Radial velocity Vs Gap size from numerical result and experimental data of Savino and Keshock [1965] at 0.3413 non-dimensional radial distance.

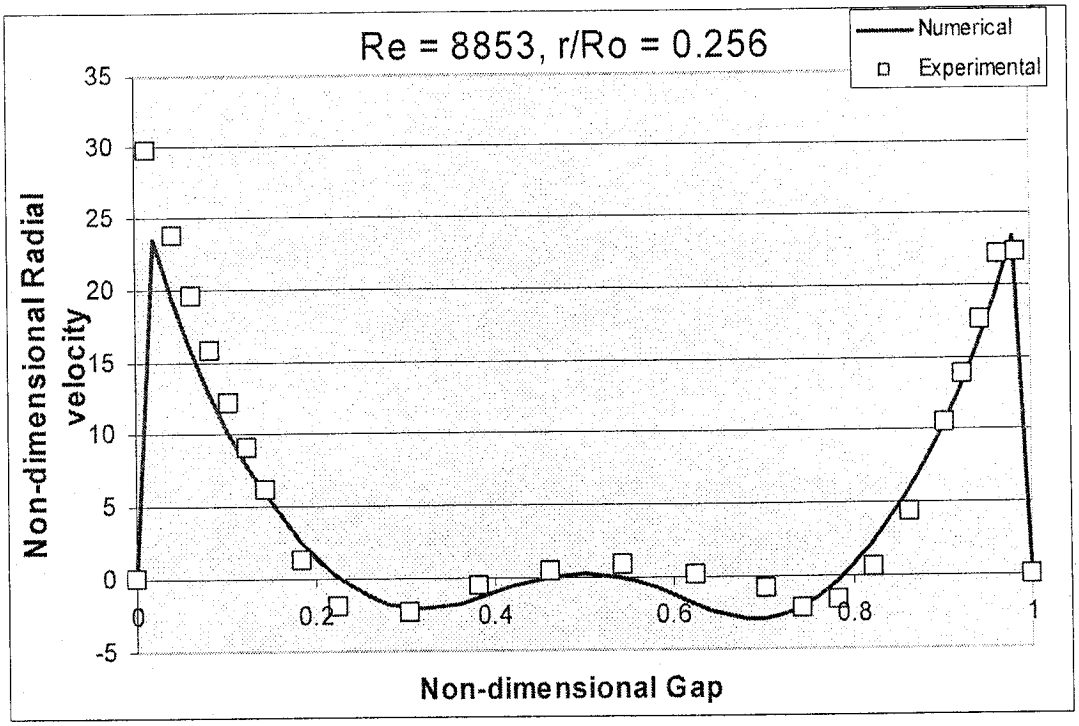

Figure 5.14(f): Radial velocity Vs Gap size from numerical result and experimental data of Savino and Keshock [1965] at 0.256 non-dimensional radial distance.

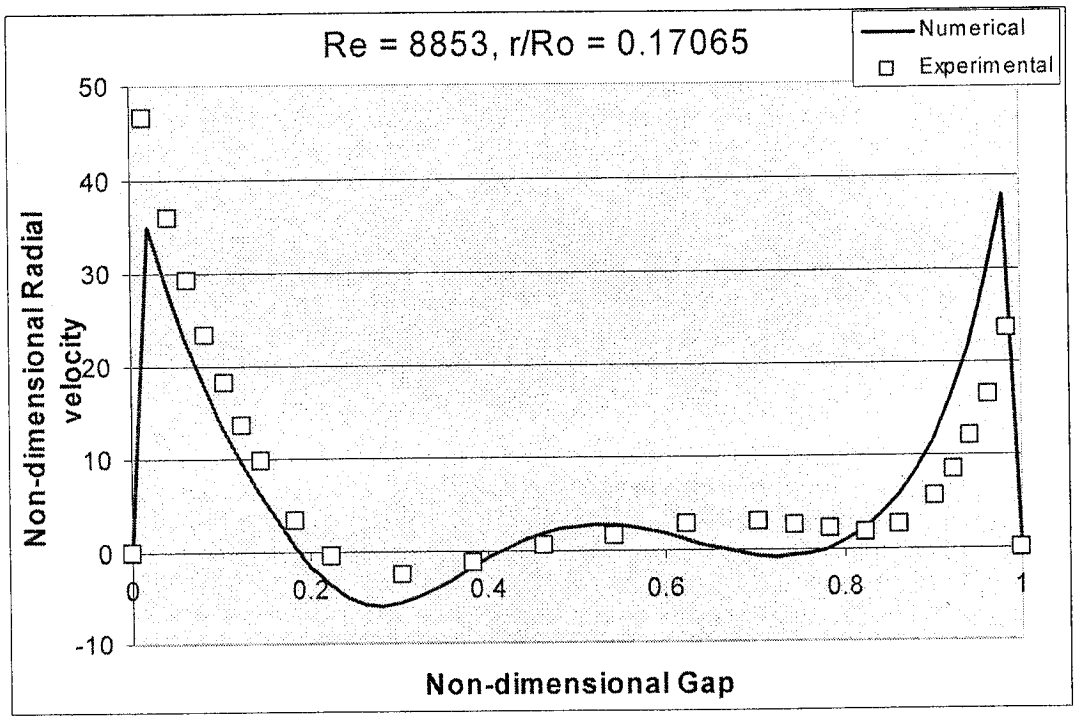

Figure 5.14(g): Radial velocity Vs Gap size from numerical result and experimental data of Savino and Keshock [1965] at 0.17065 non-dimensional radial distance.

They had reported that when tangential to radial velocity ratio is equal or less than 1.5, radial flow was found at gap centre line. If this ratio exceeded by 1.5, radial inflow was unable to penetrate the centrifugal field. Consequently, at the swirling ratio of $\geq$ 12, fluid changed their path from radial to axial direction just after entered into the chamber.

The present study is concerned with the modeling of strongly swirling turbulent inflow. The powerful tangential motion would set up the expected toroidal vortices. As the fluid enters the domain it would be quickly deflected towards the two disks and would continually flow parallel to the disk surfaces. As the fluid approaches the exit, the effective flow area decreases thus it is experiencing an increase of the inward radial momentum. Figure 5.14 confirms that near the wall the radial is greater than centrifugal acceleration.

It is therefore clear that for the case of strong swirl, the centrifugal force dominates the gap center but not the neighborhood of the wall, where it becomes weak and allows the radial flow to dominate.

Vortices cause the radial flow to reverse at the mid-plane and to reach even the near the inlet area. Figure 5.14a, 5.14b, 5.14c, shows the ability of numerical calculation to capture accurately this particular flow behavior. Let us be reminded that the inlet velocity was uniform (discussed in numerical chapter). Although in this way we approximated the flow by including the average effect this may not however be absolutely true when one wishes to capture the flow transformations very near the inlet.

As the fluid approaches the exit the effective flow area decreases thus the flow must be experiencing an increase in the inward radial velocity. This effect gives rise to the growing velocity spikes near the wall (see figures 5.14a to 5. 14g). The saddle-like shape manifestation in the velocity profile, shown in figures 5.14 (d) to (f), is the consequence of the development of a reverse flow near the mid-plane. As the fluid approaches the exit its velocity is expected to become asymmetric. This manifestation is clear in figure 5.14(g) where one of spikes (near the bottom disk) is smaller than the other. The present numerical solution using the Reynolds stress modeling predicts approximately the same trend.

iii) The Swirl Velocity

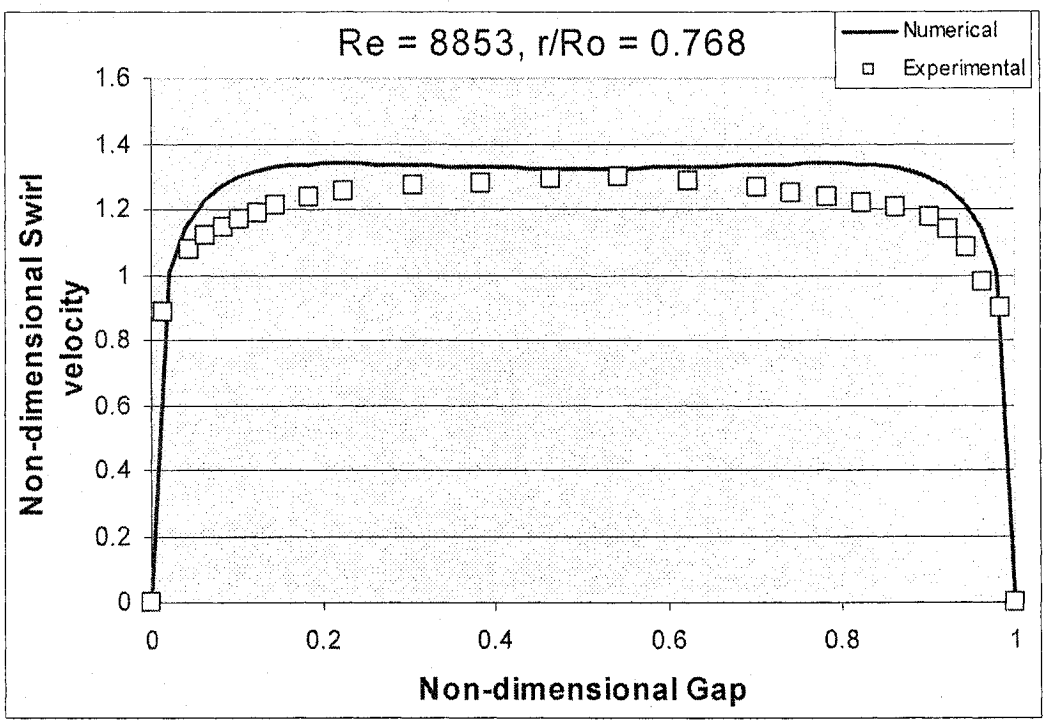

Figure 5.15(a): Swirl velocity Vs Gap size from numerical result and experimental data of Savino and Keshock [1965] at 0.768 non-dimensional radial distance.

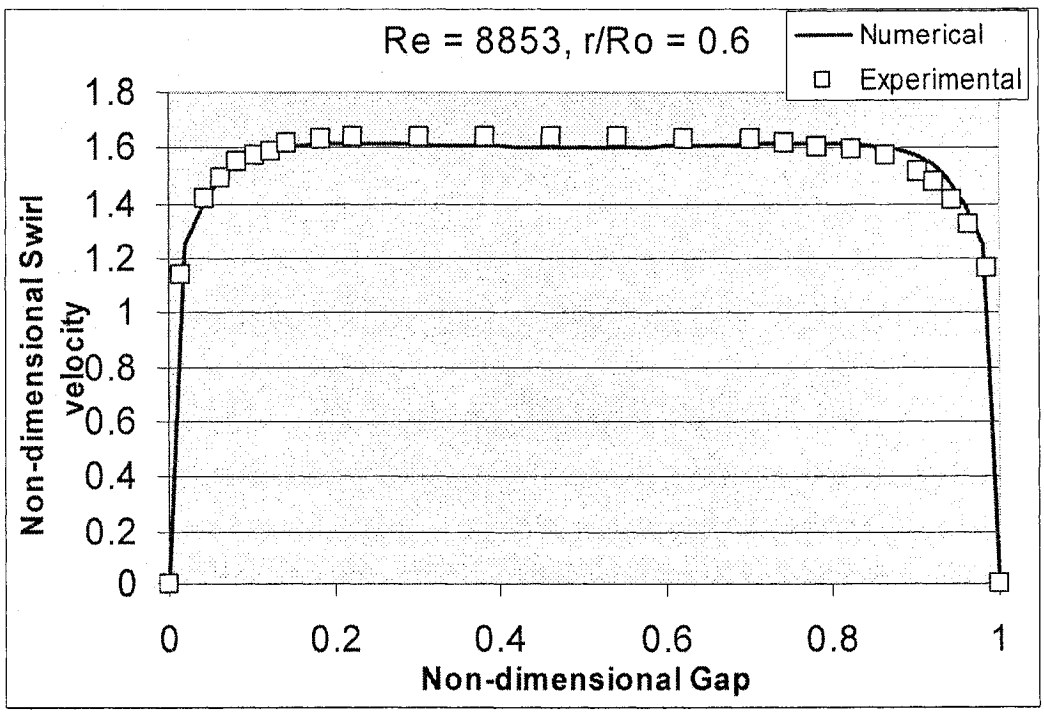

Figure 5.15(b): Swirl velocity Vs Gap size from numerical result and experimental data of Savino and Keshock [1965] at 0.6 non-dimensional radial distance.

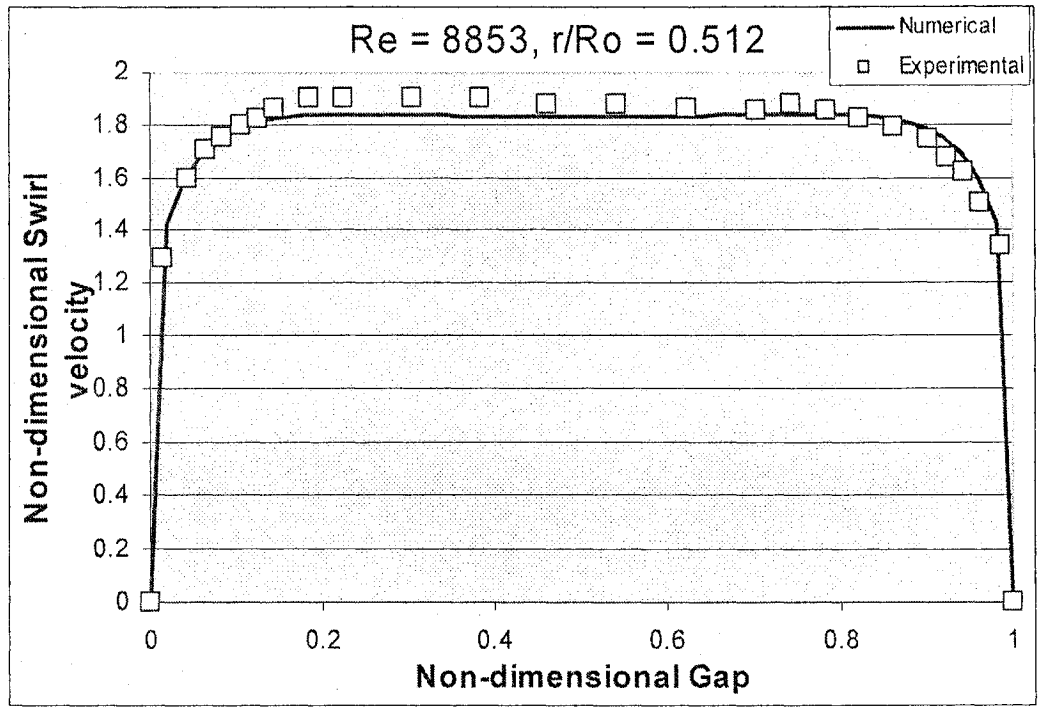

Figure 5.15(c): Swirl velocity Vs Gap size from numerical result and experimental data of Savino and Keshock [1965] at 0.512 non-dimensional radial distance.

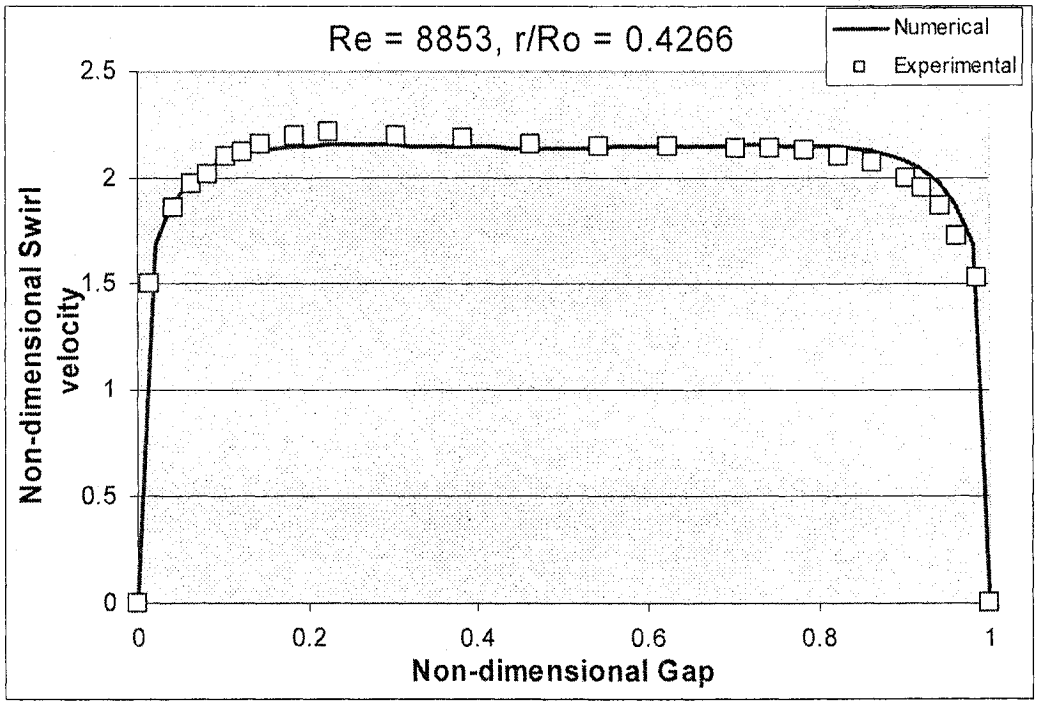

Figure 5.15(d): Swirl velocity Vs Gap size from numerical result and experimental data of Savino and Keshock [1965] at 0.4266 non-dimensional radial distance.

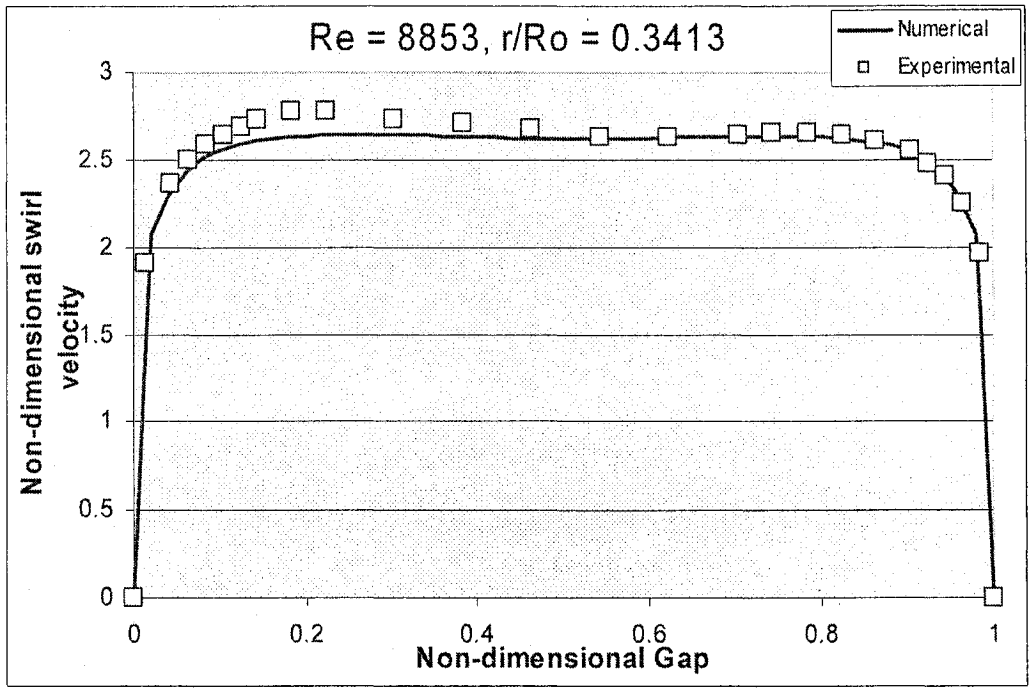

Figure 5.15(e): Swirl velocity Vs Gap size from numerical result and experimental data of Savino and Keshock [1965] at 0.3413 non-dimensional radial distance.

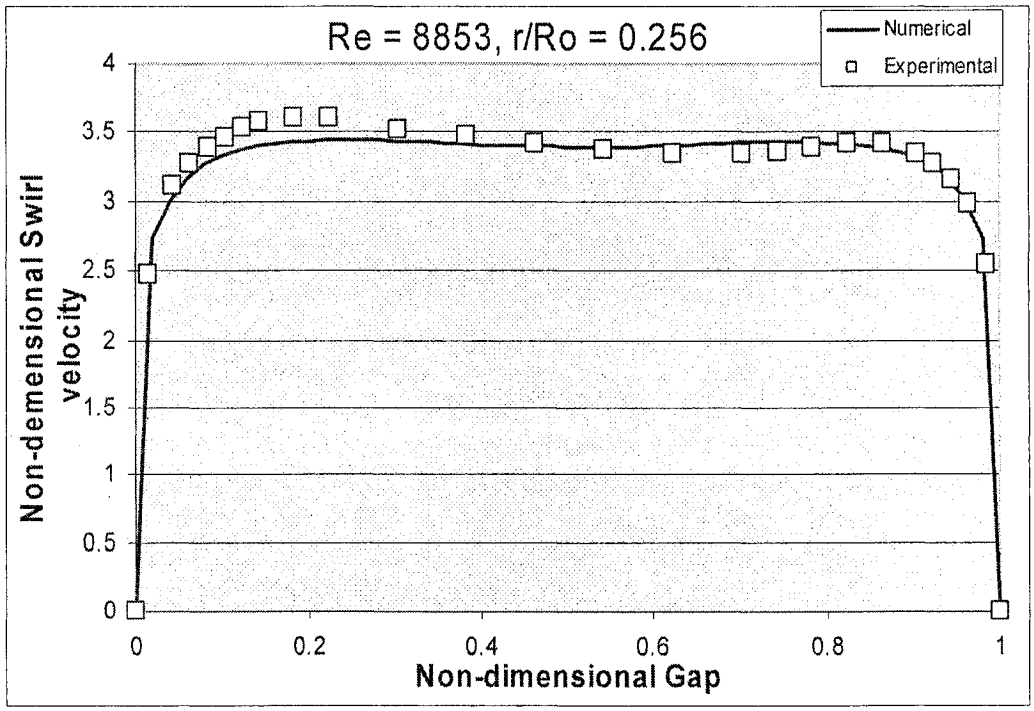

Figure 5.15(f): Swirl velocity Vs Gap size from numerical result and experimental data of Savino and Keshock [1965] at 0.256 non-dimensional radial distance.

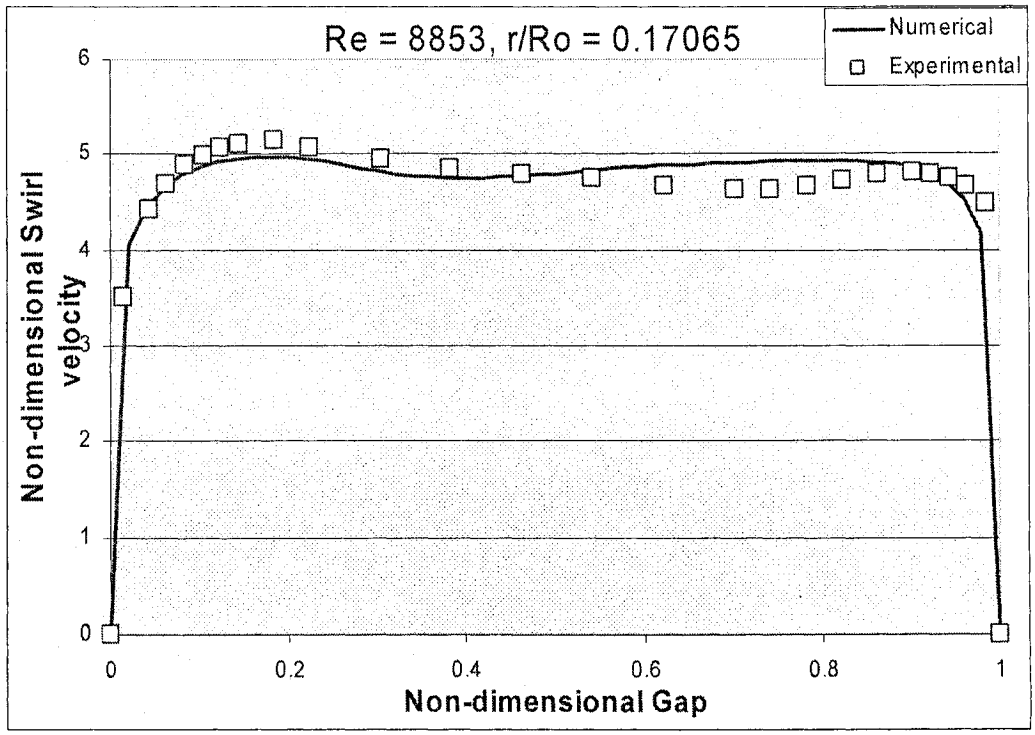

Figure 5.15(g): Swirl velocity Vs Gap size from numerical result and experimental data of Savino and Keshock [1965] at 0.17065 non-dimensional radial distance.

The development of the tangential or swirl velocity inside the chamber is expected to be that of a real vortex rather that the idealized formulation of Rankine. At the outer periphery the tangential velocity should follow closely the potential vortex profile veering away as the vortex center is approached. The last was clearly shown by Tsifourdaris [2003].

Swirl velocity is seen to remain almost flat across a good portion of the gap, see figures 5.15(a) to 5.15 (g). Near the flat surfaces of the disks the velocity reduces to zero through the Ekman's layer developed in the azimuthal direction. Two peaks in the tangential velocity profile, presented in Kendall's experiments [1962] and Vatistas' numerical computations [1984] also appear here. As anticipated the swirl

velocity is increasing towards the center (see figures 5.15a to 5.15g). Accordingly, the centrifugal force experienced by the forward moving fluid is increased. Difference between numerical and experimental profiles near the inlet (figure 5.15a) must be as due to the velocity imposition of the inlet tangential velocity, which was assumed to uniform across the entire height of the gap.

CHAPTER 6

Conclusions

Numerical investigations concerning the turbulent flow developed between two disks were conducted using the commercial CFD software FLUENT 6.1. Steady, incompressible purely radial and swirling inflows were considered.

It was shown that in the case of sink flows, inertia increased either due to inlet velocity augmentation or decrease of the local area. This produced velocity profile plateau thus suggesting that inertia must overpower the viscous forces. In the case of swirling inflow, the dominating centrifugal force pressed almost all of the flow to drain through the end plate boundary layers. It became apparent that the near the disk, radial velocity spikes are due to the synergetic contribution of boundary layer development and the reduction of the local cross sectional flow area. The numerical algorithm was found to be able to effectively simulate the mid channel recirculation zone. The latter is also the causes for the saddle-like behavior of the radial velocity. The known tangential velocity peaks near the disks known from previous studies appeared also in the current solutions.

Therefore, the present study has been validated the tool that can now be used to provide answers to some outstanding questions.

Contribution

1) Different inlet and exit conditions were examined to select appropriate boundary conditions that are able to predict reasonably accurate numerical results.

2) In case of purely radial inflow, present work catches the entrance and exit effects along with the flow of intermediate zone comparing to the previous numerical work by Singh [1993].

3) The effect of centrifugal force and the presence of toroidal vortices are successfully outlined in present investigation. These phenomena obstructed to the previous researches getting proper analytical treatment [Vatstas et al., 2005] or numerical solution [Kowk et al., 1972] for this type of flow.

4) Reasonable agreement between numerical results and those of previous experimental works indicate that the numerical tool, assumptions and boundary specifications used here are capable to predict the similar flow problem with complicated geometries relevant to the industrial applications.

5) Above all, present work is cost effective comparing to experimentations.

Future Works

1) Numerical study with time dependent solution can be done to achieve the effect of compressibility at near exit area.

2) Entrance length and effect of turbulence intensity inside the domain can be checked.

3) Problem related to the instability can be investigated.

4) Numerical and experimental work for radial outflow (with and without swirl) can be done with the similar set-up or with different gap ratios.

5) Heat transfer of the flow between two discs for sink flow and source flow with or without swirl can be examined numerically as well as experimentally.

References

1. Choudhury, D., "Introduction to the renormalization group method and Turbulence Modeling." *Fluent Inc.*, Technical Memorandum TM-107, 1993.
2. Daly, B. J., Harlow, E.H., "Transport Equations in Turbulence." *Phy. Fluid*, 13:2634-2649, 1970.
3. DeSantis, M. J., Rakowsky, E.L., "An experimental investigation of the viscous flow field in a pneumatic vortex sensor." *ASME, 70-FLCS-16*,pp. 1-12 (1971).
4. Fayed, M. "The Heat Transfer within Disk Like Geometry", Ph. D thesis, Mechanical and Industrial Engineering Department, Concordia University, Montreal, Canada (In progress Nov 2006).
5. Ferziger, J.H., Peric, M., "computational methods for fluid dynamics, 2nd edition, *Springer-Verlag Berlin Heidelberg*, 1999.
6. Fluent 6.1 User's Guide, *Fluent Inc.* USA, 2003.
7. Frankel, J. I., and Taira, K.: Integral equation formulation and error estimates for radial flow between two flat disks. *Journal of Computational and Applied Mathematics*, 181, 103-124, 2005.
8. Fu, S., Launder, B.E., Leschziner, M.A., "Modeling Strongly Swirling Recirculating Jet Flow with Reynolds- Stress Transport Closures.", In Sixth Symposium of Turbulent Shear Flows, Toulouse, France,1987.

9. Gibson, M.M., Launder, B.E., "Ground Effects on Pressure Fluxuations in the Atmospheric Boundary Layer." *J. Fluid Mechanics*, 86: 491-511, 1978.

10. Ghaly, W., Vatistas, G.H., "Numerical Solution of the flow between two discs." *ASME, Proceedings of CIE*, Sacramento, California, pp. 1-6, Sep. 1997.

11. Ghaly, W. S., Vatistas, G.H., "A parametric Study of axisymmetric swirling flows in a low aspect ratio vortex chamber." *Proceedings of ICFDP7*: International conference on Fluid dynamics and propulsion, Sharm El-Sheik, Egypt, 2001.

12. Hinze, J.O., "Turbulence", *McGraw-Hill Publishing Company*, New York, 1975.

13. Jawarneh, A., Vatistas, G.H., Hong, H., "On flow development in jet-Driven Vortex Chambers." *Journal of Propulsion and Power* (October, 2004), Vol.21, pp.564-570.

14. Kendall, J. M. "Experimental Study of a Compressible Viscous Vortex", *Jet Propulsion Laboratory Tech. Report No. 32-290*, California Institute of Technology, Pasadena, California, June 1962.

15. Kwok, C.C.K., Thinh, N.D., Lin, S., "An investigation of confined vortex flow phenomena." *Journal of Basic Engineering, Transactions of ASME*, pp.689-696, September, 1972.

16. Kwok, C.C.K., Lee, P.M., "Integral equation method for Compressible flow between two discs." *CSME-14*, vol.5, no.1, 1978-79.

17. Launder, B.E., "Second- Moment Closure and its use in Modeling Turbulent Industrial Flows.", *International Journal for Numerical Methods in Fluid,* 9:963-985; 1989.

18. Lee, P.M., Lin, S., "Pressure distribution for radial inflow between narrowly spaced discs." *Journal of Fluid Engineering*, vol.107, pp.338- 341, September, 1985.

19. Lien, F.S., Leschziner, M.A., "Assessment of turbulent transport models including non-linear RNG eddy-viscosity formulation and second –moment closure." *Computers and Fluids*, 23(8), pp.983- 1004, 1994.

20. Murphy, H.D., Coxon, M., McEligot, D.M., "Symmetric sink flow between parallel plates." *Journal of Fluids Engineering*, vol. 100, pp. 477-484, Dec, 1978.

21. Murphy, H.D., Chambers, F.W., McEligot, D.M., "Laterally converging flow. Part1.Mean flow." *J. Fluid mech.* vol. 127, pp. 379-401, 1983.

22. Savino, J. M., Keshoch, E. G., "Experimental profiles of velocity components and radial pressure distributions in a vortex contained in a short cylindrical chamber." NASA TN D-3072, Library of University of California, San Diego, pp.2-32, October 1965.

23. Shih, T.H., Liou, W.W., Shabbir, A., Yang, Z.,Zhu, J., " A new eddy viscosity model for high Reynolds number turbulent flows-model development and validation." *Computers Fluids*, 24(3), pp.227-238, 1995.

24. Singh, A., "Theoritical and Experimental investigations on inward flow between two discs." Ph. D thesis, IIT. Bombay, India, 1993.

25. Sovran, G., "Fluid mechanics of internal flow" 1967, *Elsevier publishing company*, TA 357S93, pp.39-43.

26. Speziale, C.G., Sarkar, S., Gataski, T.B., "Modeling The Pressure- Strain Correlation of Turbulence." An Invariant Dynamical System Approach, *J. Fluid Mechanics*, 227: 245- 272, 1991.

27. Tsifourdaris, P., "On the flows developed within the gap of two parallel discs." Ph. D thesis, Concordia University, Montreal, Quebec, Canada, April 2003.

28. Vatistas, G. H. "Theoretical and Experimental Studies on Confined Vortex Flows", Ph.D. Thesis, Mechanical Engineering Department, Concordia University, Montreal Canada, 1984.

29. Vatistas, G.H., "Radial flow between two closely placed flat discs." *Journal of AIAA,* vol.26, no.7, pp. 887-889, July, 1988.

30. Vatistas, G.H., "Radial inflow within two flat discs." *Journal of AIAA*, vol.28, no.7, pp. 1308-1310, July, 1990.

31. Vatistas, G.H., Ghila, A., Zitouni, G., "Radial inflow between two flat discs." *Acta Mechanica*, 113,109-118, 1995.

32. Vatistas, G.H, Ghaly, W., Tsifourdaris, P., "Swirling inflow within the narrow gap of two discs." *Journal of propulsion and power*, Vol.21, No.4, pp.743-750 July- August 2005.

33. Wormley, D.N., "An analytical model for the incompressible flow in short vortex chamber." *Transactions ASME*, pp.264-276, June, 1969.

34. Yakhot, V., Orszag, S.A., "Renormalization group analysis of turbulence: I. Basic Theory." *Journal of Scientific Computing* 1 (1), pp. 1- 51, 1986.

35. Zitouni, G., Vatistas, G.H., "Purely accelerating and decelerating flows within two flat discs." *Acta Mechanica*, 123,151-161, 1997.

APPENDIX

Non dimensional parameters are as follows;

$$u = \frac{v_r}{u_0}, \qquad v = \frac{v_\theta}{v_0}, \qquad w = \frac{v_z}{u_0}, \qquad \eta = \frac{r}{R_0}$$

$$\zeta = \frac{z}{h}, \qquad \sigma = \frac{h}{R_0}, \qquad \mathrm{Re} = \frac{u_0 h}{\nu}$$

$$S = \frac{v_0}{u_0}, \qquad \Pi = \frac{P}{\rho u_0^2}, \qquad \mathrm{Re}_r = \frac{\mathrm{Re}}{\sigma} = \frac{u_0 R_0}{\nu}$$

Introducing these non-dimensional parameters in continuity and momentum equations;

Now, continuity equation (4) can be modified as;

$$\frac{u_0}{R_0}\{\frac{\partial u}{\partial \eta} + \frac{u}{\eta}\} + \frac{u_0}{h}\frac{\partial w}{\partial \zeta} = 0$$

or, $$\frac{h}{R_0}\{\frac{1}{\eta}\frac{\partial (u\eta)}{\partial \eta}\} + \frac{\partial w}{\partial \zeta} = 0$$

or, $$\frac{\sigma}{\eta}\frac{\partial (u\eta)}{\partial \eta} + \frac{\partial w}{\partial \zeta} = 0$$

So the non-dimensional continuity equation for present flow domain will be;

$$\frac{1}{\eta}\frac{\partial (u\eta)}{\partial \eta} + \frac{1}{\sigma}\frac{\partial w}{\partial \zeta} = 0 \qquad (8)$$

Putting all non-dimensional values in r momentum equation (5);

$$uu_0\frac{\partial(uu_0)}{\partial(\eta R_0)}+wu_0\frac{\partial(uu_0)}{\partial(h\zeta)}-\frac{(vv_0)^2}{\eta R_0}=-\frac{1}{\rho}\frac{\partial(\Pi\rho u_0^2)}{\partial(\eta R_0)}+\nu[\frac{\partial^2(uu_0)}{\partial(\eta R_0)^2}+\frac{1}{(\eta R_0)}\frac{\partial(uu_0)}{\partial(\eta R_0)}+\frac{\partial^2(uu_0)}{\partial(h\zeta)^2}-\frac{uu_0}{(\eta R_0)^2}]$$

or,

$$uu_0\frac{\partial(uu_0)}{\partial(\eta R_0)}+wu_0\frac{\partial(uu_0)}{\partial(h\zeta)}-\frac{(vu_0S)^2}{\eta R_0}=-\frac{1}{\rho}\frac{\partial(\Pi\rho u_0^2)}{\partial(\eta R_0)}+\nu[\frac{\partial^2(uu_0)}{\partial(\eta R_0)^2}+\frac{1}{(\eta R_0)}\frac{\partial(uu_0)}{\partial(\eta R_0)}+\frac{\partial^2(uu_0)}{\partial(h\zeta)^2}-\frac{uu_0}{(\eta R_0)^2}]$$

or, $$\frac{u_0^2}{R_0}\{u\frac{\partial u}{\partial\eta}+\frac{R_0}{h}w\frac{\partial u}{\partial\zeta}-\frac{v^2S^2}{\eta}\}=-\frac{u_0^2}{R_0}\frac{\partial\Pi}{\partial\eta}+\nu\frac{u_0}{R_0^2}[\frac{\partial^2u}{\partial\eta^2}+\frac{1}{\eta}\frac{\partial u}{\partial\eta}+\frac{R_0^2}{h^2}\frac{\partial^2u}{\partial\zeta^2}-\frac{u}{\eta^2}]$$

or, $$u\frac{\partial u}{\partial\eta}+\frac{1}{\sigma}w\frac{\partial u}{\partial\zeta}-\frac{v^2S^2}{\eta}=-\frac{\partial\Pi}{\partial\eta}+\frac{\frac{h}{R_0}}{\frac{u_0h}{\nu}}[\frac{\partial^2u}{\partial\eta^2}+\frac{1}{\eta}\frac{\partial u}{\partial\eta}+\frac{1}{\sigma^2}\frac{\partial^2u}{\partial\zeta^2}-\frac{u}{\eta^2}]$$

or, $$u\frac{\partial u}{\partial\eta}+\frac{1}{\sigma}w\frac{\partial u}{\partial\zeta}-\frac{v^2}{\eta}S^2=-\frac{\partial\Pi}{\partial\eta}+\frac{1}{\frac{\mathrm{Re}}{\sigma}}[\frac{\partial^2u}{\partial\eta^2}+\frac{1}{\eta}\frac{\partial u}{\partial\eta}+\frac{1}{\sigma^2}\frac{\partial^2u}{\partial\zeta^2}-\frac{u}{\eta^2}]$$

So, Non-dimensional r momentum equation will be;

$$u\frac{\partial u}{\partial\eta}+\frac{1}{\sigma}w\frac{\partial u}{\partial\zeta}-\frac{v^2}{\eta}S^2=-\frac{\partial\Pi}{\partial\eta}+\frac{1}{\mathrm{Re}_r}[\frac{\partial^2u}{\partial\eta^2}+\frac{1}{\eta}\frac{\partial u}{\partial\eta}+\frac{1}{\sigma^2}\frac{\partial^2u}{\partial\zeta^2}-\frac{u}{\eta^2}] \qquad (9)$$

Putting values in dimensional θ momentum equation (6);

$$uu_0\frac{\partial(vv_0)}{\partial(\eta R_0)}+wu_0\frac{\partial(vv_0)}{\partial(h\zeta)}+\frac{(uu_0)(vv_0)}{\eta R_0}=\nu[\frac{\partial^2(vv_0)}{\partial(\eta R_0)^2}+\frac{1}{(\eta R_0)}\frac{\partial(vv_0)}{\partial(\eta R_0)}+\frac{\partial^2(vv_0)}{\partial(h\zeta)^2}-\frac{vv_0}{(\eta R_0)^2}]$$

or,

$$uu_0\frac{\partial(vu_0S)}{\partial(\eta R_0)}+wu_0\frac{\partial(vu_0S)}{\partial(h\zeta)}+\frac{(uu_0)(vu_0S)}{\eta R_0}=\nu[\frac{\partial^2(vu_0S)}{\partial(\eta R_0)^2}+\frac{1}{(\eta R_0)}\frac{\partial(vu_0S)}{\partial(\eta R_0)}+\frac{\partial^2(vu_0S)}{\partial(h\zeta)^2}-\frac{vu_0S}{(\eta R_0)^2}]$$

or, $$\frac{u_0^2}{R_0}S\{u\frac{\partial v}{\partial\eta}+\frac{R_0}{h}w\frac{\partial v}{\partial\zeta}+\frac{uv}{\eta}\}=\nu\frac{u_0}{R_0^2}S[\frac{\partial^2 v}{\partial\eta^2}+\frac{1}{\eta}\frac{\partial v}{\partial\eta}+\frac{R_0^2}{h^2}\frac{\partial^2 v}{\partial\zeta^2}-\frac{v}{\eta^2}]$$

or, $$u\frac{\partial v}{\partial\eta}+\frac{1}{\sigma}w\frac{\partial v}{\partial\zeta}+\frac{uv}{\eta}=\frac{1}{\frac{u_0R_0}{\nu}}[\frac{\partial^2 v}{\partial\eta^2}+\frac{1}{\eta}\frac{\partial v}{\partial\eta}+\frac{1}{\sigma^2}\frac{\partial^2 v}{\partial\zeta^2}-\frac{v}{\eta^2}]$$

Than, the non- dimensional θ momentum equation will be;

$$u\frac{\partial v}{\partial\eta}+\frac{1}{\sigma}w\frac{\partial v}{\partial\zeta}+\frac{uv}{\eta}=\frac{1}{\mathrm{Re}_r}[\frac{\partial^2 v}{\partial\eta^2}+\frac{1}{\eta}\frac{\partial v}{\partial\eta}+\frac{1}{\sigma^2}\frac{\partial^2 v}{\partial\zeta^2}-\frac{v}{\eta^2}] \tag{10}$$

Now substituting the dimensional z momentum equation (7);

$$u_0u\frac{\partial(u_0w)}{\partial(\eta R_0)}+u_0w\frac{\partial(u_0w)}{\partial(h\zeta)}=-\frac{1}{\rho}\frac{\partial(\Pi\rho u_0^2)}{\partial(h\zeta)}+\nu[\frac{\partial^2(u_0w)}{\partial(\eta R_0)^2}+\frac{1}{(\eta R_0)}\frac{\partial(u_0w)}{\partial(\eta R_0)}+\frac{\partial^2(u_0w)}{\partial(h\zeta)^2}]$$

or, $$\frac{u_0^2}{R_0}\{u\frac{\partial w}{\partial\eta}+\frac{R_0}{h}w\frac{\partial w}{\partial\zeta}\}=-\frac{u_0^2}{h}\frac{\partial\Pi}{\partial\zeta}+\nu\frac{u_0}{R_0^2}[\frac{\partial^2 w}{\partial\eta^2}+\frac{1}{\eta}\frac{\partial w}{\partial\eta}+\frac{R_0^2}{h^2}\frac{\partial^2 w}{\partial\zeta^2}]$$

or, $$u\frac{\partial w}{\partial\eta}+\frac{R_0}{h}w\frac{\partial w}{\partial\zeta}=-\frac{R_0}{h}\frac{\partial\Pi}{\partial\zeta}+\frac{\nu}{u_0R_0}[\frac{\partial^2 w}{\partial\eta^2}+\frac{1}{\eta}\frac{\partial w}{\partial\eta}+\frac{R_0^2}{h^2}\frac{\partial^2 w}{\partial\zeta^2}]$$

or, $$u\frac{\partial w}{\partial\eta}+\frac{R_0}{h}w\frac{\partial w}{\partial\zeta}=-\frac{1}{\sigma}\frac{\partial\Pi}{\partial\zeta}+\frac{1}{\frac{u_0R_0}{\nu}}[\frac{\partial^2 w}{\partial\eta^2}+\frac{1}{\eta}\frac{\partial w}{\partial\eta}+\frac{1}{\sigma^2}\frac{\partial^2 w}{\partial\zeta^2}]$$

$$u\frac{\partial w}{\partial\eta}+\frac{R_0}{h}w\frac{\partial w}{\partial\zeta}=-\frac{1}{\sigma}\frac{\partial\Pi}{\partial\zeta}+\frac{1}{\mathrm{Re}_r}[\frac{\partial^2 w}{\partial\eta^2}+\frac{1}{\eta}\frac{\partial w}{\partial\eta}+\frac{1}{\sigma^2}\frac{\partial^2 w}{\partial\zeta^2}] \tag{11}$$